



Virginia Commonwealth University
VCU Scholars Compass

Theses and Dissertations


Graduate School

2023

Using Superatomic Clusters and Charge Transfer Ligands to Control Electronic Characteristics of Phosphorene Nanoribbons and Phosphorene Monolayer

Ryan Lambert
Virginia Commonwealth University

Follow this and additional works at: <https://scholarscompass.vcu.edu/etd>

 Part of the [Atomic, Molecular and Optical Physics Commons](#), [Computational Chemistry Commons](#), [Condensed Matter Physics Commons](#), [Materials Chemistry Commons](#), [Physical Chemistry Commons](#), and the [Quantum Physics Commons](#)

© Ryan Lambert

Downloaded from

<https://scholarscompass.vcu.edu/etd/7411>

This Dissertation is brought to you for free and open access by the Graduate School at VCU Scholars Compass. It has been accepted for inclusion in Theses and Dissertations by an authorized administrator of VCU Scholars Compass. For more information, please contact libcompass@vcu.edu.

© Ryan Lambert 2023
All Rights Reserved

**Using Superatomic Clusters and Charge Transfer Ligands to
Control Electronic Characteristics of Phosphorene Nanoribbons
and Phosphorene Monolayer**

A Dissertation Submitted in Partial Fulfillment of the Requirements for the Degree
of Doctor of Philosophy in Nanoscience & Nanotechnology at Virginia
Commonwealth University

by
Ryan Lambert

Director: Shiv N. Khanna, Ph.D.
Chairman and Commonwealth Professor
Department of Physics

Virginia Commonwealth University
Richmond, Virginia
May 2023

**To My Wonderful Family,
With Special Dedication to My Beloved
Grandmother,
Dr. Audrey Eubanks**

Acknowledgments

First, I would like to thank my advisors, Dr. Shiv Khanna and Dr. Arthur Reber, for their continued support from my acceptance into the Nanoscience and Nanotechnology graduate program to present. Dr. Reber was always willing to sit and answer my questions on research problems and ensure my adequate understanding. I am forever grateful for Dr. Khanna's ability to explain complex subject matter with simplicity and eloquence – something which sparked my own interest in solid state physics. It is a tribute to his passions for teaching and the quest for new knowledge which he so fervently shares with his students. Thank you both for your guidance.

I would also like to extend special thanks to Turbasu Sengupta who helped me on countless occasions, sometimes with the most mundane of tasks, and was always happy to do so. I will always appreciate the extra time spent helping me with research from tweaking input files to our discussions about new work in the field, and, in general, your kind words of encouragement.

I am also grateful to the many professors and fellow students who have been positive influences in my academic journey. Thank you to our group collaborators at Columbia University, and to the additional members of my committee, Dr. Daeha Joung and Dr. Jayasimha Atulasimha.

Finally, I would like to express my greatest thanks and gratitude to my wife, my family, and my friends. Without your unwavering support, this accomplishment would have been infinitely more trying. To my wife: Mackenzie, thank you from the bottom of my heart. The late nights and early mornings spent studying and working have finally paid off. I am eternally grateful for your love, your patience, and your companionship. I hope to return, in kind and value, your support with the same grace you have shown me throughout the years. To my parents: Jim and Nicole, simply put, I could not be where I am today in my life without you both. Thank you for your wisdom, guidance, and love. To my sister: Hanna, I am forever thankful for your lifelong friendship and for the humor you bring when it is most needed. I strive to continue to make you all proud in my professional pursuits and to always be a positive force in this world. At last, to my son and daughter, Cashel, and Faye: thank you for being an endless source of joy and giving me renewed purpose each day. You can accomplish great things when you set your mind to it. I look forward to and cherish the gift of watching you both forge your own paths in life.

Table Of Contents

Chapter 1. An Introduction to Two-Dimensional Materials Featuring Phosphorene and A Novel Approach To Surface Doping.....	13
1.1 Motivation – A History of Innovation and the Modern Demand for Technological Advancement.....	13
1.2 A Brief Background on Two-Dimensional Materials:.....	14
1.3 Graphene as a Starting Point for Modern 2-D Materials:.....	17
1.4 Phosphorene Background and Phosphorene Nanoribbon Synthesis:.....	18
1.5 Research Interests in Phosphorene Nanoribbons:.....	22
1.6 Designer Superatoms as Efficient Donors or Acceptors:.....	23
1.7 Extension of Chemical Doping Concepts to Superatoms and Other Two-Dimensional Systems.....	26
1.8 Research Objectives and Remaining Composition.....	31
Chapter 2. Density Functional Theory and Computational Methods.....	37
2.1 Introduction and Background.....	37
2.2 The Schrodinger Equation:.....	38
2.3 The Electron Density:.....	40
2.4 The Thomas-Fermi Model:.....	42
2.5 The Hohenberg-Kohn Theorems.....	44
2.6 The Kohn Sham Method:.....	50
2.7 Exchange-Correlation Energy and Choice of Functional.....	56
2.7.1 Local Density Approximation (LDA).....	57
2.7.2 Generalized Gradient Approximation (GGA).....	59
2.7.3 Meta-GGA functionals.....	60
2.7.4 Hybrid Exchange Functionals.....	60
2.8 Periodic Boundary Conditions.....	62
2.9 The Reciprocal Space Lattice, Plane Wave Basis, and Monkhorst Pack k-Point Sampling.....	64
2.10 Non-Periodic, Cluster Model DFT Calculations.....	68
2.11 Computational Details.....	70
Chapter 3. Ligand and Width Effects: Fragmentation Pathways, Ribbon Stability, Band Gap, Work Function and Electron Affinity.....	78
3.1 Introduction.....	78
3.2 Discussion of Naming, Geometry, Relative Stability, and Potential Fragmentation Pathways:.....	80
3.3 Band Structure and Band Gap Scaling with Width and Edge Passivation:.....	93
3.4 Work Function and Electron Affinity Observations:.....	97
3.4.1 Hydrogen-Terminated Zigzag Phosphorene Nanoribbons.....	97
3.4.2 Hydrogen-Terminated Armchair Phosphorene Nanoribbons.....	100

3.5	Bader Charge Analysis:.....	101
3.6	Summary and Conclusions	103
Chapter 4. Controlling the Location of Quantum States in Phosphorene Nanoribbons via Edge Passivation with Various Ligands		109
4.1	Introduction	109
4.2	Cluster Model – an Investigation of the Nature of Edge Ligands Leading to a Shift in Molecular Orbitals and Ionization Energy	110
4.3	Effects of Varying Ligation on the Electronic Structure of Periodic Phosphorene Nanoribbons and Chemical Doping via Sodium Adatoms.....	118
4.4	Control of Work Function by Various Edge-Passivation of N = 9 Zigzag Phosphorene Nanoribbon	119
4.5	Controlling Bandgap and Inducing a Metallic Transition via Sodium Atom Deposition on Phosphorene Nanoribbon Surface.....	122
4.6	Bader Charge Analysis of Phosphorene Nanoribbons with Various Edge-Passivation.....	126
4.7	Conclusions	128
Chapter 5. Transforming the Electronic Properties of Phosphorene through Charge Transfer Superatomic Doping.....		135
5.1	Introduction	135
5.2	Controlling the Band Gap in Phosphorene by depositing Superatoms:	137
5.3	Controlling p-/n- Character using $Re_6Se_8Cl_n(PH_3)_{5-n}$ Clusters as Charge Transfer Dopants:.....	144
5.4	Conclusions	150
Chapter 6. Proposed Future Work: Extending Charge Transfer Doping to Various Two-Dimensional Systems and Magnetic Superatoms		155
Appendix-A.....		159

List Of Figures

Figure 1.1 Band gap values as a function of PNR width in direct comparison with ribbon type, termination, and the monolayer sheet.	20
Figure 1.2 One-electron energy levels of optimized ground state ligated clusters through ligand exchange from 6PEt ₃ to 6CO. Reprinted with permission from the authors Khanna and Reber. [45].....	25
Figure 1.3 Plot of the energy shift in HOMO and LUMO levels (left) and the adiabatic ionization energy (AIE) compared to adiabatic electron affinity (AEA) for Co ₆ Te ₈ (PEt ₃) _n (CO) _{6-n} (right). Reprinted with permission from Khanna and Reber.[45]	26
Figure 1.4 Geometry and placement of Co ₆ Se ₈ (PEt ₃) _{5,6} superatomic clusters on WSe ₂ surface to initiate charge transfer doping effects. Reprinted with permission from Khanna and Reber [43].....	29
Figure 1.5 Visualization of the shift in fermi level as the inserted HOMO and LUMO levels change with respect to ligand exchange on the cluster.	29
Figure 1.6 “(a) Schematic of a back-gated TMDC FET doped with electron-rich molecular clusters, Co ₆ Se ₈ (PEt ₃) ₆ . Transfer characteristics of the fewlayer (b) MoS ₂ and (c) WSe ₂ FETs. The black and red curves are before and after doping with superatoms, respectively.”[55,56]	30
Figure 2.1. Kohn-Sham DFT flow chart depicting the self-consistency method for energy minimization.....	54
Figure 2.2. Representation of the transformation from real space (a) to reciprocal space (b) and the construction of the first Brillouin Zone for a face-centered cubic (fcc) real space lattice, from VASP lecture, Martijn Marsman, University of Vienna, open source.[7,24]	65

Figure 2.3. Visualization of the truncation of the plane wave basis in reciprocal space via the cutoff energy such that the cutoff energy is less than or equal to kinetic energy of the67

Figure 3.1. (a) Structure of non-terminated armchair phosphorene nanoribbon. (b) Hydrogen terminated armchair phosphorene nanoribbons. (c) Non-terminated and (d) hydrogen-terminated zig-zag ribbons. Note, also, highlighted atoms, labeled $N = 1-5$, identify the naming convention for the ribbon widths in both armchair (a)–(b) and zig-zag ribbons (c)–(d). (e) Comparison of optimized structures of non-terminated zigzag phosphorene nanoribbons (left) and hydrogen-terminated zigzag phosphorene nanoribbons (right). (f) Comparison of optimized structures of non-terminated armchair phosphorene nanoribbons (left) and hydrogen-terminated armchair phosphorene nanoribbons (right). Note the differences in edge reconstruction between non-terminated and hydrogen-terminated structures in both (e) and (f).82

Figure 3.2. Visual comparison of geometry optimization for non-terminated (a.) and terminated (b.) APNRs of width $N = 5$84

Figure 3.3. Visual comparison of geometry optimization for non-terminated (a.) and terminated (b.) ZPNRs of width $N = 5$85

Figure 3.4. Lowest energy fragmentation pathway for non-terminated APNR, width $N = 5$, showing cleavage point as well as the subsequent geometry optimized fragments for top-down (a.) and face-on (b.) views. Note the significant reconstruction of the $N = 2$ fragment and persistent edge reconfiguration of the $N = 3$ (New) fragment.86

Figure 3.5. Lowest energy fragmentation pathway for terminated APNR, width $N = 5$, showing cleavage point as well as the subsequent geometry optimized fragments for top-down (a.) and face-on (b.) views.....86

Figure 3.6. Lowest energy fragmentation pathway for non-terminated ZPNR, $N = 5$, showing cleavage point of the ribbon for top down (a.) and face on (b.) views as well as the geometry optimized fragments.....87

Figure 3.7. Lowest energy fragmentation pathway for terminated ZPNR, $N = 5$, showing cleavage point of the ribbon for top down (a.) and face on (b.) views as well as the geometry optimized fragments.87

Figure 3.8. Graph of minimum fragmentation energies for respective ribbon types. Note, the significant shift in fragmentation energy for non-terminated APNRs could be a result of the rearrangement occurring in the small fragment ($N = 2$).....	90
Figure 3.9. Comparison of geometric reconstruction in the small, non-terminated armchair ribbons ($N = 2$ (a), left and $N = 3$ (a), right). (b) Structure for tetrahedral phosphorous used to compare energies with the reconstructed non-terminated APNRs (c) The reconstruction demonstrated by the hydrogen terminated PNRs, showing minimal reconstruction. (d) Energy comparison of APNRs, $N = 2 - 9$, with tetrahedral phosphorous. Note, the horizontal axis, 'N,' is indicative of ribbon width.	91
Figure 3.10. Band gap values as a function of PNR width in direct comparison with ribbon type, termination and the monolayer sheet.....	95
Figure 3.11. Work function and electron affinity as functions of increasing ribbon widths for hydrogen-terminated zigzag PNRs.	98
Figure 3.12. Comparison of Fermi level, vacuum level, and conduction band for zigzag PNRs. Note, Conduction band remains relatively constant with changes in width while the vacuum level and fermi level are pushed up overall.	100
Figure 3.13. Work function and electron affinity as functions of increasing ribbon widths for hydrogen-terminated armchair PNRs.	100
Figure 3.14. Comparison of Fermi level, vacuum level, and conduction band for hydrogen-terminated armchair PNRs. Note, Conduction band remains relatively constant with changes in width while the vacuum level and fermi level are pushed up overall. ..	101
Figure 4.1 The structure of the Phosphorene cluster model, $P_{141}H_{35}$, top view, front view, and side view.	112
Figure 4.2 The structure of the Phosphorene cluster models with the following termination, A) H B) Cl, C) NH_2 , D) SCH_3 , E) OH, F) OCN, and G) OCH_3	113
Figure 4.3 The HOMO and LUMO energy of the Phosphorene cluster models as a function of the ligand.....	113
Figure 4.4 The ionization energy, dipole moment, a comparison of the ionization energy and dipole moment, and the net charge on the phosphorene as compared to the ligand. The dipole moment is calculated by binding one side of the sheet with the ligand and	

the other side is hydrogen terminated. The dipole moment is positive if it is pointing from the ligand to the phosphorene, and negative if it is pointing from the phosphorene to the ligand.....	114
Figure 4.5 The structure of the cluster model of phosphorene with one side ligated with OCN, Cl, OH, OCH ₃ , SCH ₃ , and NH ₂ . The dipole vector is shown in red, and the vector points from the ligand either towards or away from the phosphorene sheet depending on the sign of the dipole moment.....	117
Figure 4.6 Visualization of geometry for various termination/ligations of N=9 zigzag PNR. a) SCH ₃ – Terminated, b) NH ₂ – Terminated, c) OH – Terminated, d) SH – Terminated, e) H – Terminated, f) Cl – terminated, g) OCN – terminated.....	119
Figure 4.7 Work Function various termination and Na – adsorption with varying concentration	120
Figure 4.8 Bandgap vs edge termination with adsorbed Na concentration for 0, 2, 4, 6, and 8 Na	121
Figure 4.9 Work function and Bandgap vs. Termination for comparison of bandgap change with termination to work function change with termination. B.G. remains constant pointing to level change as a result of dipole effects of edge terminal groups/ ligands.....	122
Figure 4.10 Visualization of converged geometry with sodium adsorption. (a) various concentrations of sodium adsorbed on hydrogen edge-passivated N = 9 zigzag PNR. (b) Example of standard unit cell dimensions for all nanoribbons using hydrogen edge-passivation.	123
Figure 4.11 Comparison of projected density of states for OCN-Terminated 0, 2, and 8 Na cases, top, middle, and bottom respectively.	124
Figure 4.12 Visualization of charge density distribution for conduction band (a, b) and valence band (c, d) in different orientations of the unit cell.....	126
Figure 5.1. Complete picture of all CONTCAR geometry for Co ₆ S ₈ (PH ₃) _{5-n} (CO) _n doped phosphorene monolayer as a function of n from 0 – 5 (a-f).....	138

Figure 5.2. Binding energies of phosphine ligands to cluster and cluster to surface as ligands are exchanged as a function of n for both (a) $\text{Re}_6\text{Se}_8(\text{Cl})_n(\text{PH}_3)_{5-n}$ and (b) $\text{Co}_6\text{S}_8(\text{CO})_n(\text{PH}_3)_{5-n}$ respectively.	140
Figure 5.3. (a) The structure of $\text{Co}_6\text{S}_8(\text{PH}_3)_5$, $\text{Co}_6\text{S}_8(\text{CO})_3(\text{PH}_3)_2$, and $\text{Co}_6\text{S}_8(\text{CO})_5$, supported on Phosphorene. (b) The position of the valence and conduction band of phosphorene, and the HOMO and LUMO of the $\text{Co}_6\text{S}_8(\text{CO})_n(\text{PH}_3)_{5-n}$ cluster as a function of n. Note, the valence band maximum is set to zero in the presentation of the band energy levels.	141
Figure 5.4. Projected density of states for $\text{Co}_6\text{S}_8(\text{PH}_3)_{5-n}(\text{CO})_n$ as a function of n, plotted from results obtained using the HSE06 hybrid functional. Note, for sumo software, the legend cutoff for PDOS is 3% thus, C and O are not included in the legend due to their low contribution to overall number of states in the plotted energy range.	143
Figure 5.5. Charge density associated with LUMO (a-c) and HOMO (d-f) states of the cluster for $\text{Co}_6\text{S}_8(\text{CO})_{1,3,5}(\text{PH}_3)_{4,2,0}$	144
Figure 5.6. Complete picture of all CONTCAR geometry for $\text{Re}_6\text{Se}_8(\text{PH}_3)_{5-n}(\text{Cl})_n$ doped phosphorene monolayer as a function of n from 0 – 3 (a-d).	145
Figure 5.7. (a) The structure of $\text{Re}_6\text{Se}_8(\text{PH}_3)_5$, $\text{Re}_6\text{Se}_8\text{Cl}_2(\text{PH}_3)_4$, and $\text{Re}_6\text{Se}_8\text{Cl}_3(\text{PH}_3)_2$, supported on Phosphorene. (b) The position of the valence and conduction band of phosphorene, and the HOMO and LUMO of the $\text{Re}_6\text{Se}_8\text{Cl}_n(\text{PH}_3)_{5-n}$ cluster as a function of n.	147
Figure 5.8. Charge density associated with HOMO and LUMO states of the cluster for $\text{Re}_6\text{Se}_8\text{Cl}_{1,2,3}(\text{PH}_3)_{4,3,2}$	148
Figure 5.9. The projected density of states of $\text{Re}_6\text{Se}_8(\text{PH}_3)_5$, $\text{Re}_6\text{Se}_8\text{Cl}(\text{PH}_3)_4$, $\text{Re}_6\text{Se}_8\text{Cl}_2(\text{PH}_3)_3$, and $\text{Re}_6\text{Se}_8\text{Cl}_3(\text{PH}_3)_4$. In this case, the VBM energy is set to zero.	149
Figure 6.1. Example structures of phosphorene nanoribbons doped with $\text{Co}_6\text{S}_8(\text{CO})_5$ superatoms with zigzag (a) and armchair (b) geometries respectively.	156
Figure 6.2. Visualization of various ligated magnetic metal chalcogenide clusters, $\text{Fe}_6\text{E}_8\text{CO}_5$, deposited on monolayer MoS_2 , where E = S, Se, and Mn, from top to bottom.	157

List Of Tables

Table 3.1. Comparison of average Bader Charge for edge phosphorus and hydrogen atoms of various ribbon widths.....	103
Table 4.1 Bader charge of bare zigzag phosphorene nanoribbon of width $N = 9$	127
Table 4.2 Bader charge of sodium adsorbed zigzag phosphorene nanoribbon of width $N = 9$	127
Table 5.1. Comparison of binding energies for ligand-to-cluster and cluster-to-surface showing that all cases, for both (a) $\text{Co}_6\text{S}_8(\text{PH}_3)_{5-n}(\text{CO})_n$ and (b) $\text{Re}_6\text{Se}_8(\text{PH}_3)_{5-n}(\text{Cl})_n$ superatomic clusters, the cluster binds preferentially to the surface of the phosphorene monolayer.	139

Abstract

Using Superatomic Clusters and Charge Transfer Ligands to Control Electronic Characteristics of Phosphorene Nanoribbons and Phosphorene Monolayer

By Ryan Lambert, Ph.D.

A dissertation submitted in partial fulfilment of the requirements for the degree of Doctor of Philosophy in Nanoscience & Nanotechnology at Virginia Commonwealth University.

Virginia Commonwealth University, 2023

Major Director: Shiv N. Khanna, Ph.D.

Commonwealth Professor and Chairman, Department of Physics

Phosphorene is a two-dimensional electron poor p-type semiconductor with high carrier mobility and great promise for applications in electronics and optoelectronics. As the main theme in this dissertation, the following work represents different investigations of various electronic properties associated with phosphorene. Most notable are the findings on charge transfer doping with metal-chalcogenide superatoms which displays novel control of the two most important properties of a semiconductor – the band gap energy and the nature of carriers. By tuning the width of the gap and p-/n-type character of conduction, we gain control over a material's capacity to play a certain role upon incorporation into a device setting. For example, control of bandgap characteristics on the nanometer and sub-nanometer scale is an integral next step for scientists and engineers to move beyond the current size limit of logic transistors. Additionally, improving the function of optoelectronics leading to a variety of positive enhancements in sensing devices spanning a wide array of fields from specialized medical devices to ubiquitous consumer electronics. Another possibility is fine-tuning photovoltaic devices to increase efficiency or expand the energy range which a solar panel may harvest light, subsequently increasing overall output

– a vital component to our transition and continued improvement of renewable energy technologies.

Summary of Contents

Chapter 1: A brief survey of two-dimensional materials and an introduction of the various compositions which lead to novel physical and chemical properties like ambipolar and anisotropic electronic behavior, strain- and layer-dependent bandgap, and relatively high carrier mobility. A more thorough introduction of phosphorene and phosphorene nanoribbons and associated research interests such as the ribbon stability and fragmentation pathways, tunability of bandgap and work function are discussed as well.

Chapter 2: The short history and significance of the Density Functional Theory (DFT) can be found in Chapter 2. Additionally, the relevant theory and density functional formalisms associated with calculations completed in investigations of phosphorene are discussed in more depth. One can also find explanations for key takeaways and the reason DFT has been so successful to this day at producing reliable calculations for the energy minimization problem and other important electronic properties in solid state physics and physical chemistry such as band gap and work function. Computational details for various structures calculated with periodic and non-periodic boundary conditions are included in this chapter as well.

Chapter 3: Results presented in this chapter first discuss the effects of edge passivation with hydrogen on the stability of nanoribbons before moving into the work on potential fragmentation pathways. In the final portions, the effect of ribbon width and edge passivation on electronic properties like bandgap, work function and electron affinity as well as Bader charge analysis can be found. This chapter provides the groundwork for the remaining composition of the dissertation by combining verification of previous trends in literature with studies in stability. These results lead to questions about the control of phosphorene nanoribbon quantum states as well as novel doping techniques which may add to the tunability of electronic properties while maintaining crystallinity of phosphorene.

Chapter 4: Here one can find a discussion on the effects of varying edge-passivating ligands on the bandgap, work function, electron affinity, and ionization energy of small

phosphorene flakes as well as nanoribbons. Additionally, an exploration of chemical doping via sodium atom adsorption shows the potential in tuning the bandgap of phosphorene nanoribbons.

Chapter 5: Combining the principles of chemical doping and control of quantum states via ligand exchange in metal chalcogenide superatoms leads to a success story in charge transfer doping. This chapter covers the specific results associated with adsorbing ligated metal chalcogenide superatoms to a phosphorene support. Ultimately, it was shown that this technique can be utilized in altering the carrier nature of the material from p-type to n-type.

Chapter 6: This chapter covers several promising potential directions for future work including the extension of charge transfer doping via superatoms to magnetic ligated metal chalcogenide superatoms on a variety of two-dimensional supports.

Chapter 1. An Introduction to Two-Dimensional Materials Featuring Phosphorene and A Novel Approach To Surface Doping

1.1 Motivation – A History of Innovation and the Modern Demand for Technological Advancement

“We were wanderers from the beginning...then, as now, technology was the key to our survival.”[1] Carl Sagan’s sage observations eloquently highlight the survival advantage of our species’ wandering and plundering tactics. All the while, technological advances yielded one tribe’s gain and held the power to exert more and more dominance over their domain. Beyond improved survival, climbing the hierarchy of needs through human history also allowed for interests in convenience to enter our daily lives. By the twentieth century, technologies made possible a quality of life which our distant ancestors could have scarcely imagined. However, advent of ease would not quell our species’ wandering spirit. In 1990, one feat of science and engineering also gave us the gift of humility – the view of home from roughly six billion kilometers. Voyager 1 successfully completed its mission tour of our solar system but it also served as a poignant reminder of our unified existence. Thus, technology not only improves our survival and global quality of life but the has the power to unify and inspire fellow humans.

Presently, we are faced with another unifying realization – in the light of our species’ successes, our collective actions now carry the significance to affect all souls on our planet. Our collective wellbeing far into the future depends on solutions which meet

human demand but, not at the expense of nature. Developments in energy technologies, which make access and storage equitable and efficient, improvements in shelter which do not degrade our health, and even equitable access to clean water, depend upon the combined efforts of scientists, engineers, lawmakers, and consumers.

At the heart of the technological term in the equation of progress, stands materials research. The ability to push past current limitations depends upon the discovery, fundamental understanding, and production of novel materials. One such area of growth includes two-dimensional materials. This class of materials shows great promise due to novel mechanical, electronic, and magnetic properties which would enable sizable leaps forward in chip manufacturing, energy storage, optoelectronics, spintronics, and additive manufacturing. This dissertation focuses on the advancement of two-dimensional materials with particular attention to a material called phosphorene with an exploration of novel surface doping techniques. Let us begin with an overview of the field.

1.2 A Brief Background on Two-Dimensional Materials:

Palpable interest in two-dimensional materials dramatically increased in 2004 with the first mechanical exfoliation of graphene by A. Geim and K. Novoselov.[2,3] The realization of two-dimensional materials with unique properties which were dramatically different from bulk counterparts spelled exciting new opportunities for technological advancements. Thus, a hunt ensued for materials characterized by novel properties resulting from quantum confinement and size effects.[2] Presently, the existence of hundreds of stable single-layer materials has been proposed.[4] Among the most commonly known are other single element materials e.g. silicene, stanene, plumbene, phosphorene, etc. transition metal dichalcogenides (TMDCs or TMDs) such as MoS₂ and

WSe₂, and others like Boron Nitride, Carbon Nitride, Boron Carbo-Nitride, Clays, etc. While enthusiasm surrounding potential practical uses for these materials is in abundance, the materials have yet to be incorporated into devices at scale and are still mainly subjects of research. Thus, research remains vital to garner an understanding of fundamental material properties which enable the development of new technologies and devices. It is the aim of this proposal to briefly outline the properties of two-dimensional materials, provide an in-depth discussion of the current state of phosphorene, outline the necessary background information to understand superatoms and their potential role in providing another control for tunability of two-dimensional materials, and, finally, to discuss the completed research and proposed future work.

In general, two-dimensional materials are defined to be crystalline solids consisting of a single layer of atoms or a single polyhedron layer.[3,5] This simple definition may be expanded considerably as we further characterize unique behaviors exhibited by the large variety of possible single-layer materials. Several different classes have been proposed to better categorize two-dimensional materials.[3] Though there are sources which quote five different categories of 2D materials, the three which comprise the majority of research and prove most promising in terms of potential for application will be the ones covered in this brief review of 2D materials.[12]

First, there are layered van der Waals solids such as graphene, h-BN, phosphorene, SiC, Si₂BN, transition metal dichalcogenides (TMDs) (MX₂ (X-M-X layer) where M=Ti, Zr, Hf, V, Nb, Ta, Mo, W, and X = S, Se, Te), and layered metal oxides such as vanadium oxide and Sb₂Te₃, etc.[3,8] Characteristics within the first category run the gamut of electrical behavior from zero bandgap graphene to insulating h-BN. They are grouped,

generally, as a result of the van der Waals forces which “bond” the layers together. Note, as the main subject of research covered in this proposal is phosphorene, this particular class of materials will be the one with which we are most concerned. However, it is prudent to provide an outline of other well-researched 2D materials so that the reader may have a more complete picture of the wide range of possibilities in this area of research.

Layered ionic solids comprise the second category. As the name suggests, these materials possess stronger, ionic interlayer bonding. This interlayer bonding may “consist of a charged polyhedral layer sandwiched between hydroxide or halide layers by electrostatic forces”[3] as in the superconducting material La_2CuO_4 ; however, it is also possible to have layers bound by electropositive ions such as Na or Ca as seen in CaZn_2Sb_2 , a well-known thermoelectric material.[32,33] Other examples include, $\text{La}_{0.90}\text{Eu}_{0.05}\text{Nb}_3\text{O}_{10}$, KLnNb_2O_7 , $\text{Eu}(\text{OH})_{2.5}(\text{DS})_{0.5}$. [3] Behaviors of these solids are quite unique and have only recently been explored. Notable properties range from the superconducting behavior of La_2CuO_4 and thermoelectric properties of CaZn_2Sb_2 , both of which are derived, in part, by the anisotropy within the solids.[33] These exciting findings can be considered significant developments in materials science and in the evolution of goals for energy-harvesting thermoelectric materials as well as high temperature superconducting materials and even oxidation catalysts.[33,34]

Finally, the third category “includes surface-assisted nanolayered solids such as silicene, germanene, stanene, etc”.[3] This class of materials generally requires growth on a substrate under high vacuum and high temperature via molecular beam epitaxy (MBE). They too have unique physical and chemical properties compared to their bulk counterparts but the challenges lie within control of the epitaxial growth as well as controlled

exfoliation in order to utilize the material in application settings. Developments such as those shown in a 2016 study published by Gibaja et al. which “isolated few-layered antimonene by both liquid phase exfoliation and mechanical cleavage methods” are required to progress this class of materials.[10,11]

1.3 Graphene as a Starting Point for Modern 2-D Materials:

Graphene, since its first mechanical exfoliation in 2004, represents the beginning of the boom in modern day research of two-dimensional materials.[2] It falls in the first category of van der Waals layered materials and is the most well-known and researched two-dimensional crystal. It forms an atomically thin, honeycomb lattice structure with sp^2 hybridization of the carbon atoms.[3,12] As a result, graphene boasts an “all-surface” structure compared to its bulk counterpart meaning an extremely high surface to volume ratio.[12] Properties like high carrier mobility ($\mu > 10^3 \text{ cm}^2/\text{Vs}^{12}$) at room temperature, excellent thermal conductivity, and quantum confinement effects have been well documented and rightfully lead to significant buzz in the scientific community surrounding the potential for graphene.[14] For all its elicited excitement, graphene does have its limitations; most notably, the lack of bandgap restricting the application of graphene in electronic devices. Engineering a bandgap in graphene is certainly possible but requires the introduction of impurities which significantly affect carrier mobility.[12,13] Thus, the existence of such unique properties does not automatically equate to an ability to harness them in device construction. However, recent works by Geim, Novoselov, Liu, and others[26-31] have shown that, although graphene alone is limited in its applications within electronic devices, it is a member of a host of 2D materials which have the potential to be combined in the creation of van der Waals heterostructures proving to have unique

properties of their own.[11,26-30] These combinations of materials in the creation of heterostructures echo the spirit of the questions raised by Richard Feynman in his 1959 lecture, “There’s Plenty of Room At The Bottom”. Thus, supporting the notion that, if we can control the individual components of devices at the nanoscale, we may observe new physics and ultimately reach technological capabilities which were previously unimaginable.

1.4 Phosphorene Background and Phosphorene Nanoribbon Synthesis:

One member of the suite of 2D materials known today has garnered significant attention recently. Phosphorene, or two-dimensional black phosphorus, is the subject of a growing number of studies examining electronic properties from a few to single layers.[15,25,35,36] Subsequent excitement surrounding this particular member of the van der Waals category is due to its extraordinary, directional and layer-dependent properties. High carrier mobility (up to $1000 \text{ cm}^2/\text{Vs}$) similar to that of conventional semiconductor materials ($1500 \text{ cm}^2/\text{Vs}$) coupled with a relatively low current on/off switching ratio compared to transition metal dichalcogenides (TMDs) has been referred to as a good trade-off.[15,18,36] These characteristics, as well as a bulk, direct bandgap of 0.3eV and monolayer, direct bandgap of 1.51eV situate phosphorene on the spectrum between zero bandgap graphene (very high mobility and low on/off ratio) and the transition metal dichalcogenides (low mobility and very high on/off ratio).[15-23]

Pristine phosphorene possesses a puckered honeycomb structure due to its sp^3 hybridized bonding, creating two different P – P bond lengths. This atomic structure ultimately leads to the observed anisotropic characteristics "including its electronic, thermal and ionic transport properties".[15] For example, Yongqing Cai et al. performed a

first principles study revealing the layer-dependent workfunction of few layer phosphorene with significant tunability up to 5L before reaching the bulk value of about 4.5eV (DFT, PBE level).[25] Other works have shown that the layer-dependent bandgap is highly tunable and can also be altered via edge termination/ functionalization, doping, and strain.[21,24] Furthermore, separating phosphorene from the metal dichalcogenides and graphene, is its ambipolar character allowing for n-type or p-type semiconducting behavior.[21] The aforementioned properties make phosphorene an attractive potential material for “interfaces which are themselves the devices” as described by Herbert Kroemer.[12,21] There are, however, limitations to this novel material which have thus far proved to be a hindrance in application settings. Most significant are concerns about stability. Phosphorene is known to be rather unstable and begins to degrade in as little as a few hours in ambient conditions through the adsorption of water molecules and conversion of the surface to phosphoric acid, subsequently dissolving the sheet and rendering the material useless.[21] Excitingly, recent findings by Watts and Picco et al. show that it is possible to synthesize phosphorene nanoribbons (PNRs) in a variety of widths and with extraordinary aspect ratios. Best of all, these findings note a stability of ribbons far greater than that of their few layer and monolayer counterparts, lasting up to six days in ambient lab conditions before degrading. Nanoribbons were synthesized via lithium intercalation of black phosphorus and immersion in solvents. The proposed chemical scissors action by the Li ions weakens and breaks the longer P-P bonds resulting in fragments. Layers become negatively charged as a result of the Li ion intercalation and, after immersion in polar solvent, zig-zag phosphorene nanoribbons (ZPNRs) are formed.[15]

The synthesis and stabilization of PNRs represent a promising advancement for this material as these ribbons display even more tunability than few to monolayer phosphorene.[15,21,36,37] First-principles electronic properties of PNRs have been well documented and display band gap tunability with varying ribbon width, edge termination, and strain.[21,36,37] In general, band gap value increases with decreasing number of layers or decreasing width of the PNR. Thus, it has been said that the increase in bandgap follows an increase in confinement effects from decreasing number of layers or increase in the contributions of edge states in the ribbons of decreasing width.[36] Additionally, it is critical to note the electronic anisotropy of phosphorene between armchair (APNR) and zig-zag nanoribbons (ZPNR) leading to significant differences in band properties which can be seen in Figure 1.1. In the case of the respective ribbons, non-passivated or non-terminated ZPNRs have been shown to have a metallic nature while hydrogen edge-termination leads to an indirect bandgap.[36,38]

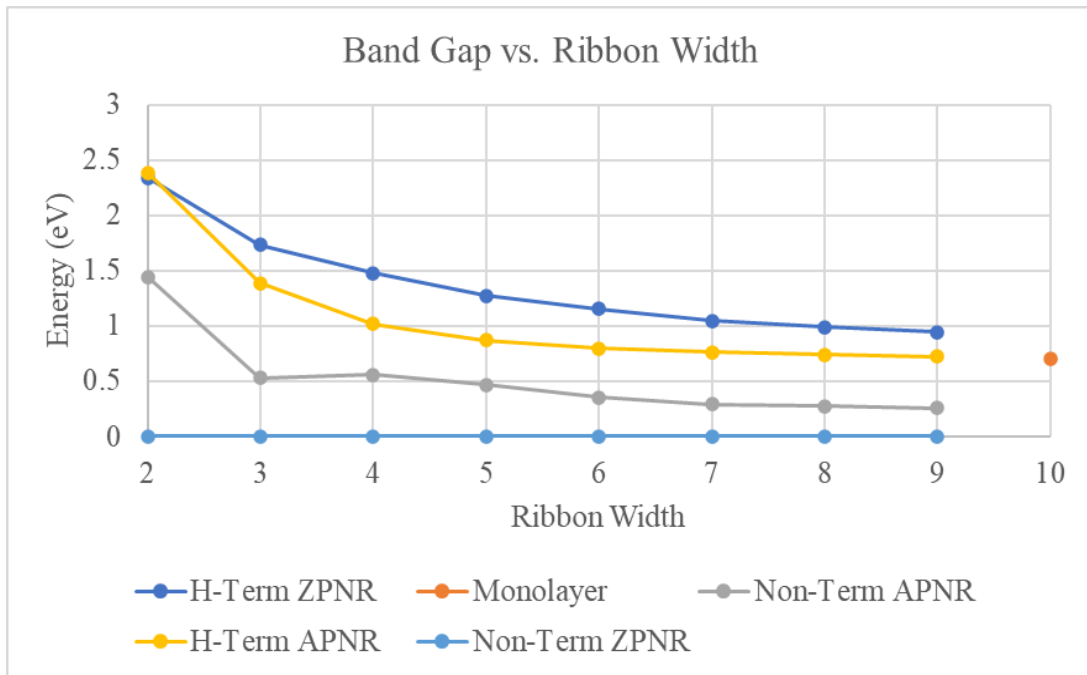


Figure 1.1 Band gap values as a function of PNR width in direct comparison with ribbon type, termination, and the monolayer sheet.

Non-terminated APNRs exhibit an indirect bandgap while hydrogen edge-termination of the APNRs leads to a direct bandgap.[36] Multiple studies have reported both direct and indirect bandgaps as well as nearly direct bandgaps.[36,38,39] Thus, the nuances here should be subsequently addressed.

Tran et al. published a study in 2014 discussing the scaling behavior of hydrogen edge-terminated PNR bandgaps in armchair PNRs (APNRs) vs zig-zag PNRs (ZPNRs).[39] In this discussion of bandgap tunability, the scaling properties as a function of ribbon width were the focus. It was shown that, based on the kind of ribbon (i.e. type of ribbon created by direction of propagation, armchair or zig-zag) different bandgap scaling was observed. In other words, the electronic anisotropy leads not only to a difference in value of bandgap along different directions of the material, but also a difference in how the bandgap scales with width in armchair vs zig-zag ribbons. Importantly, in the discussion of the character of these bandgaps, Tran et al. discussed observations that both kinds of ribbons exhibited “nearly direct bandgaps.” More specifically, it was observed that in each ribbon type, the true bandgap of the material was shifted slightly away from the gamma point, or, origin of the first Brillouin zone in the reciprocal space lattice. However, the difference in energies between the true bandgap and the bandgap taken at the gamma point were all less than 20meV for each ribbon type and ribbon width.[39] Therefore, given the small difference in energy between the “true valence band maximum and local valence band maximum at the gamma point”, the materials are considered direct bandgap materials.[38,39] Since there are multiple other studies which have presented findings highlighting the strain-dependence of bandgaps, the observations made by Tran et al. seem

acceptable in that, at room temperature conditions, these small variances in bandgaps would be difficult to detect experimentally.[36,37] Ultimately, Tran et al. and similar studies show that PNRs exhibit exceptional tunability with control of nanoribbon width and edge termination as well as strain and layer-dependent variability.

1.5 Research Interests in Phosphorene Nanoribbons:

This work has been of significant interest within our research group and as a result has been the subject of my research with several questions in mind. First, the question of stability. If phosphorene is to be used in the construction of widely applicable devices, the material must be stable enough in ambient conditions not to degrade and be rendered useless. As shown in the work presented by Watts and Picco et al., phosphorene nanoribbons are significantly more stable at room temperature in ambient conditions than their mono-to-several-layer counterparts.[15] At this point, however, we do not know of any other studies that have investigated the stability characteristics and potential fragmentation pathways. As such, we have performed an examination of the possible fragmentation pathways as well as the relative stability of the fragments. Additionally, edge-passivation or ligation plays a significant role in the observed stability of PNRs of varying width. Detailed results and discussion are provided in subsequent sections in this dissertation.

Also of interest are the tuning of the electronic and even magnetic properties. There is a wide variety of applicable areas of interest such as room temperature magnetism, spin density waves, and applications in photovoltaic water splitting, batteries, etc. However, for the purposes of this dissertation, a specific focus on tuning electronic properties including the band gap by varying width of the ribbon as well as varying

terminal groups at the edges of nanoribbons. Since demonstrated possible, the ability to synthesize individual ribbons offers the unique potential of tuning the electronic properties by selectively functionalizing edge termination.[15]

1.6 Designer Superatoms as Efficient Donors or Acceptors:

In addition to varying the band gap width and shifting the electronic spectrum up or down, the possibility to utilize and advance the principles of chemical doping in order to change p-/n-character of phosphorene is of great interest. Specifically, we investigate the capacity of ligated metal chalcogenide superatoms to act as charge transfer dopants, and effectively influence carrier concentration and type compared to a traditional chemical doping approach. To adequately address the nuances of the aforementioned approach, we begin by outlining the relevant concepts of superatoms in more depth. The origins of the superatom concept lie in the ideas of magic numbers associated with electronic and geometric shell closings. Almost forty years ago Knight and coworkers reported significant variations in the abundance of size-selected clusters generated by molecular beam of alkali metals.[40,42] Clusters which appeared most frequently were a result of higher binding energy and subsequently labeled “magic numbers”.[42] High ionization energy and low polarizability were key attributes of these magic number clusters – patterns synonymous with closed electronic shells (as opposed to closed nuclear shells in nuclear physics).[42] It was then posited that these periodic trends of magic numbers were likely due to quantum confinement effects. Subsequently, the shell model under the jellium approximation was developed for metallic clusters in which a nearly free electron gas was confined to a spherical square well in a uniform positive background which led to spherical shells in which the electron gas was grouped. These shells, or allowed quantum states, were ordered

1S, 1P, 1D, 2S, 1F, 2P, . . . and are a result of the orthogonality requirements of the core and delocalized electrons within the nearly free electron gas.[41] Ultimately, the shell closings predicted by this model accounted for the observation of accepted magic number metal clusters at sizes 2, 8, 18, 20, 34, 40, . . .[40,41,42] The ideas developed by Knight et al. led to the formalism that a cluster with an effective zero valent superatomic state was both electronically and chemically stable.[42]

This concept has been explored on various fronts by Khanna and coworkers and has led to the development of a concise definition for superatoms as: “clusters whose chemical and electronic properties are dominated by their proximity to a zero valent state, just like the valence of atoms in the Periodic Table”. [42] The superatom concept has been expanded to metal chalcogenide clusters leading to highly stable clusters with closed electronic shells and large HOMO-LUMO gaps. , to multiple valence superatoms which have been shown useful in chemical doping via the formation of charge transfer complexes.[43] First and foremost, unlike noble and transition metal clusters, metal chalcogen clusters do not abide by the nearly free electron gas approximation. Instead, covalent bonding between metal d-electrons and chalcogen p-electrons prohibits this behavior. However, the cluster symmetry introduced by the octahedral geometry and filling of the cluster valence shell leads to enhanced stability among the transition metal chalcogenide clusters. Khanna and coworkers have shown that a variety of different ligated transition metal chalcogenide combinations with octahedral geometry (TM = transition metal, E = chalcogen), exhibit closed electronic shells and high stability are maintained even under ligand exchange thereby exhibiting unique control of quantum states through ligand exchange.[42,45,46] At such small sizes, confinement effects dominate the clusters’ electronic behavior, grouping

states into shells much akin to atomic orbitals which led to the view that some such clusters

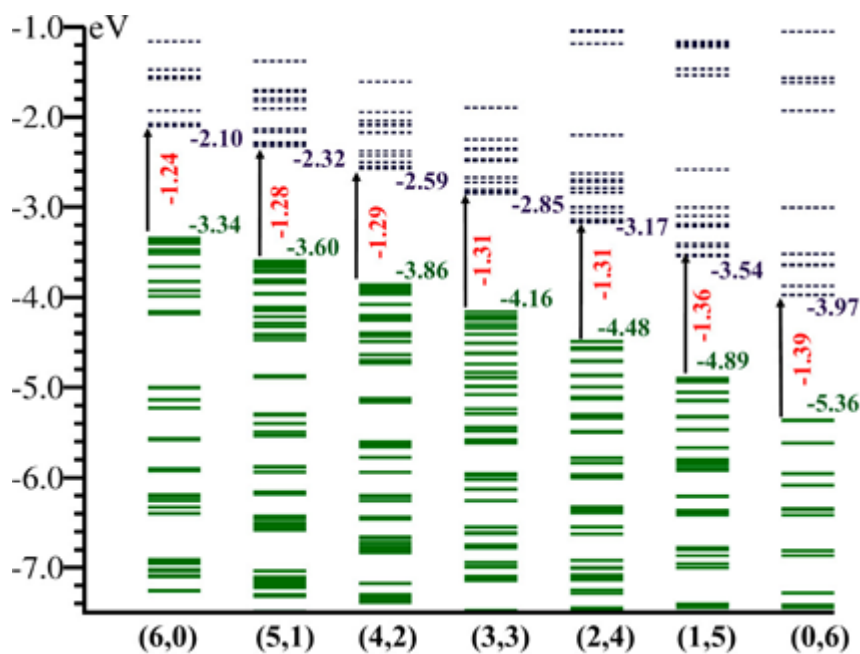


Figure 1.2 One-electron energy levels of optimized ground state ligated clusters through ligand exchange from 6PEt₃ to 6CO. Reprinted with permission from the authors Khanna and Reber. [45]

could be considered superatoms.[43,45,46] With the electronic contributions from the binding of ligands either through charge transfer or traditional covalent bonding, it has been shown that the entire electronic spectrum shifts up or down based on a specific ratio of donating vs accepting ligands while maintaining the large HOMO-LUMO gap and therefore overall stability. The cluster's electron affinity and ionization energies subsequently are affected as well demonstrating control over the cluster's electronic spectrum. These effects can be visualized with the help of Figure 1.2 which shows the shift in one-electron levels during the course of ligand exchange.

Figure 1.3 displays the subsequent shifts in adiabatic ionization energy and electron affinity as well as the cluster highest occupied molecular orbital (HOMO) and lowest unoccupied molecular orbital (LUMO) levels. This work is directly related to our intrigue in the ability to form nano p-n junctions as published in a study by Khanna and Reber with $\text{Co}_6\text{S}_8(\text{Pet}_3)_6$ superatoms on WSe_2 surface and has been extended to our interest in the unique properties of phosphorene nanoribbons.[43] Chapter 5 discusses the results of charge transfer doping of phosphorene with ligated metal chalcogen superatoms.

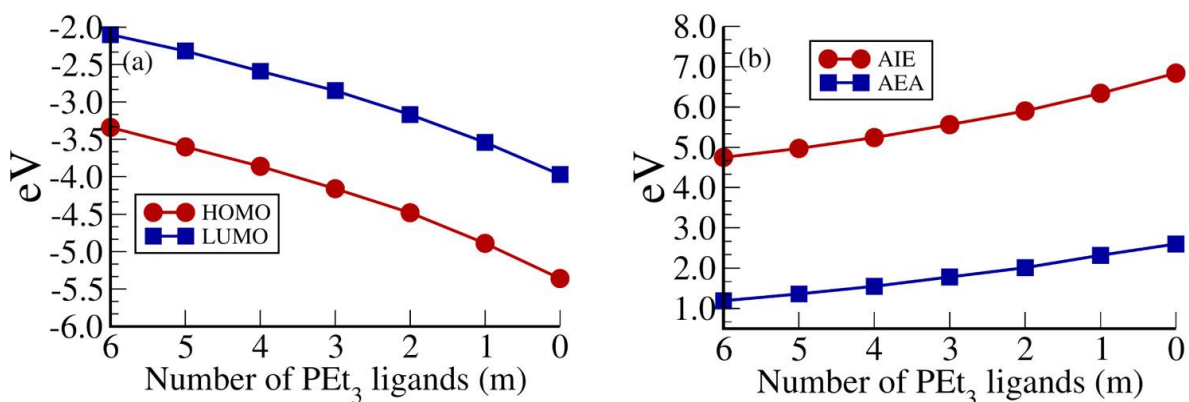


Figure 1.3 Plot of the energy shift in HOMO and LUMO levels (left) and the adiabatic ionization energy (AIE) compared to adiabatic electron affinity (AEA) for $\text{Co}_6\text{Te}_8(\text{PET}_3)_n(\text{CO})_{6-n}$ (right). Reprinted with permission from Khanna and Reber.[45]

1.7 Extension of Chemical Doping Concepts to Superatoms and Other Two-Dimensional Systems

Our interest in chemical doping stems from the inherent limitations of current standards for doping semiconductor materials. Most semiconducting materials are doped with impurities which are incorporated into the crystal lattice of the system. The “kind, concentration, and location of impurity levels” govern observed characteristics.[54-55] As

such, they are restricted by the ability of and degree to which the semiconductor material can incorporate the aforementioned impurities; a task known to be difficult or, at the very least expensive and technologically limiting (e.g. photolithography, proprietary doping and assembly techniques). If one has any doubt, one need not look further than the sheer number of patents awarded to device companies such as IBM or TSMC.

Kiriya, D. and others have explored one potential solution, in the realm of two-dimensional or thin film solids, for overcoming limitations of bulk semiconductors.[58,59] The approach consists of surface-deposition of dopants which bind directly to surface sites. This deposition, whether through field effect or charge transfer donation, has a significant effect on charge carrier density within the material. There are limitations here too, however. Atoms are typically only able to donate a single electron and are limited by their second ionization energy.[43] Additionally, atomic control of coverage can be difficult to direct potentially leading to unintended effects in semiconductor applications like the collapsing of bandgap entirely, inducing metallic behavior. Thus, it would certainly be an improvement if surface dopants could donate multiple carriers with relative energetic ease and still exert the ability to control p-/n-type character. Khanna and Reber provide a preliminary investigation of this very concept utilizing $\text{Co}_6\text{S}_8(\text{Pet}_3)_6$ superatoms on WSe_2 surface in which, the effects of ligand exchange on the nature of charge donation behavior and subsequent effects on semiconducting character of the material as a whole are outlined.[43] It was shown that the ligated cluster, $\text{Co}_6\text{S}_8(\text{Pet}_3)_5$ binds preferentially with the WSe_2 surface over the fully ligated $\text{Co}_6\text{S}_8(\text{Pet}_3)_6$ counterpart and charge donation behavior is tunable via ligand exchange at the cluster (superatom) level. This is a key attribute as the tunability of HOMO and LUMO levels in the cluster give the ability to

tailor the superatom in order to either inject electrons into the bandgap of the surface material, or situate the LUMO below the valence band of the surface material thereby affecting carrier concentration and kind. Excitingly, the ionization potentials were also calculated yielding a first ionization energy of 4.76eV (lower than that of the sodium atom), followed by 7.48eV 10.38 eV, and 12.88 eV for the removal of second, third, and fourth electron.[43] Thus, there is a realistic possibility for donation of more than a single electron to the system. Visualization of geometries and superatom placement can be seen in Figure 1.4.

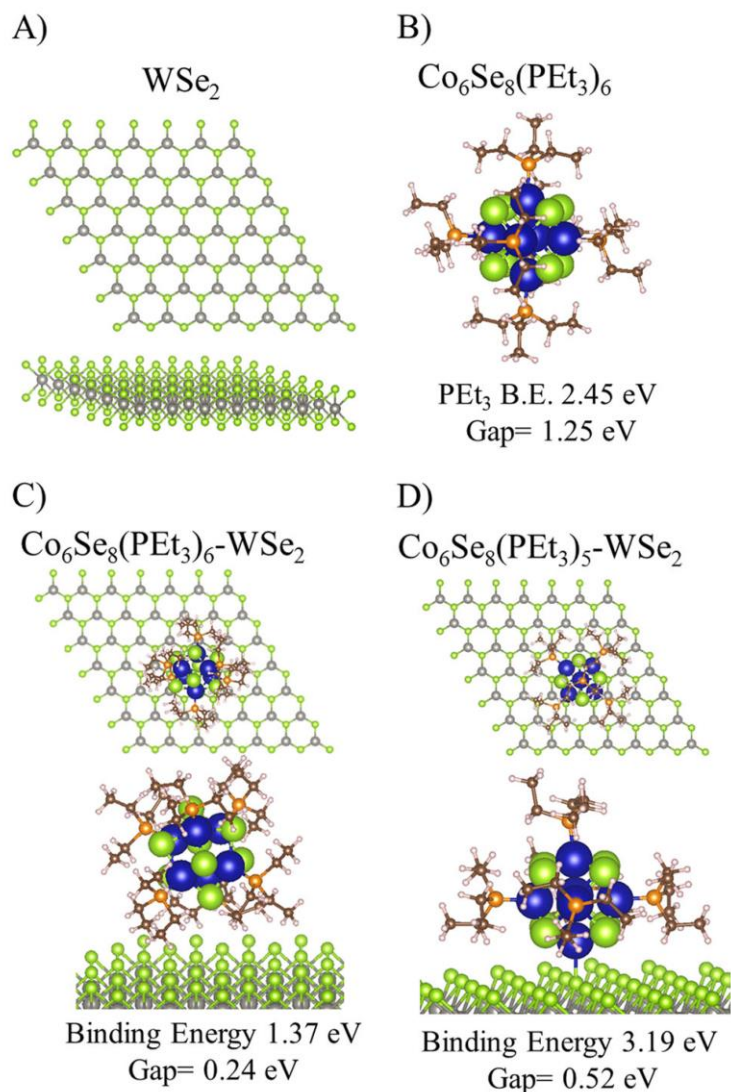


Figure 1.4 Geometry and placement of $\text{Co}_6\text{Se}_8(\text{PEt}_3)_{5,6}$ superatomic clusters on WSe_2 surface to initiate charge transfer doping effects. Reprinted with permission from Khanna and Reber [43]

Figure 1.5 displays the control of fermi energy of the material through subsequent ligand exchange at the cluster level.

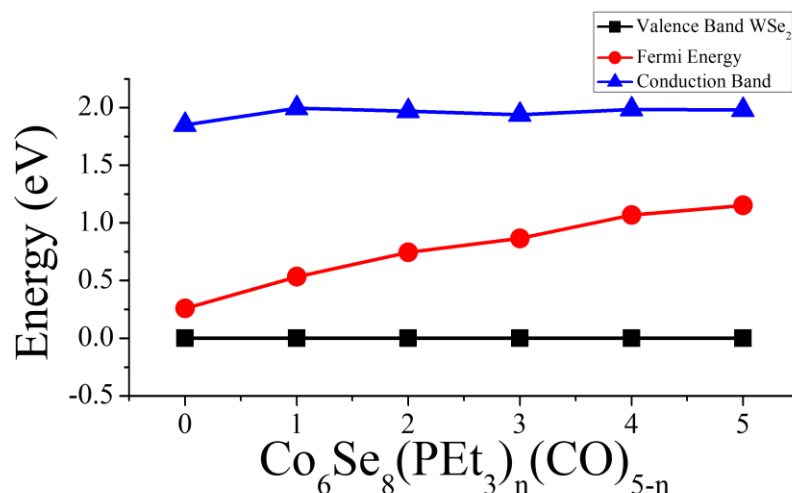


Figure 1.5 Visualization of the shift in fermi level as the inserted HOMO and LUMO levels change with respect to ligand exchange on the cluster.

Ultimately, this combination of effects leads to an ability for twofold control over tuning of the fermi level of the material; both at the level of the cluster through ligand exchange and the ability of the superatom to donate more than one electron in a charge-transfer complex with the WSe_2 surface. Experimental work from the group of Nuckolls et al. at Columbia University have utilized these novel ideas and doped two-dimensional transition metal chalcogenides using $\text{Co}_6\text{Se}_8(\text{PEt}_3)_6$ superatoms as electron donors.[55,56] Their experiments indicate that electron-rich superatom could be used as a tunable and controllable surface dopant for the semiconductors. For example, their experiments show that they could transform MoS_2 from moderately to heavily electron-doped-states by controlling the concentration of superatoms in the solution. Fig. 1.6 shows the transfer characteristics of the n-type MoS_2 upon doping from the experiments by Nuckolls et

al.[55,56] Even more interesting was that for WSe₂, the characteristics of the film changed from hole transporting to electron transporting upon doping (Fig. 1.6). They further used a lithographic mask (h-BN) to selectively dope areas of WSe₂ film thereby creating p-n junctions effectively creating a diode. These are remarkable findings that could open the pathway to novel class of doped semiconductors.

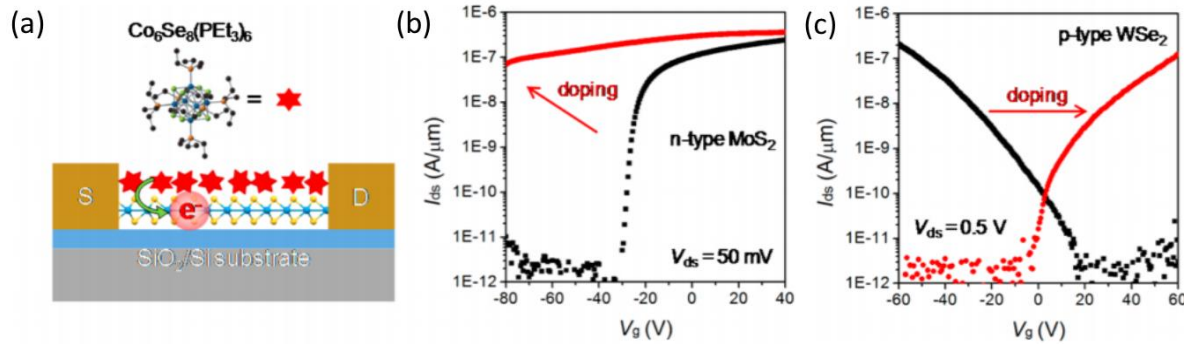


Figure 1.6 “(a) Schematic of a back-gated TMDC FET doped with electron-rich molecular clusters, Co₆Se₈(PEt₃)₆. Transfer characteristics of the fewlayer (b) MoS₂ and (c) WSe₂ FETs. The black and red curves are before and after doping with superatoms, respectively.”[55,56]

We are particularly interested in exploring the possibility of controlling the semiconducting properties of nanoribbons by charge transfer doping methods, and, in general, whether it is even possible to apply these methods to a material such as phosphorene with such a high valence band relative to proposed dopant superatoms. Results of these investigations are covered in Chapter 5 in more detail.

1.8 Research Objectives and Remaining Composition

The work presented in the subsequent chapters follows the motivation of the next three research objectives:

1. A study of the relative stability and fragmentation patterns of phosphorene nanoribbons and the effects of ligation or edge-passivation on the potential fragmentation pathways available during synthesis.
2. Investigating the effects of edge-passivation with various ligands on the work function and associated quantum states of the system.
3. The comparison between traditional chemical doping via atoms or small molecules and charge transfer doping of phosphorene by ligated metal chalcogenide superatoms with a specific aim to control p-/n-character of the system.

Chapter 2 discusses the development of density functional theory and relevant methods utilized in the theoretical research presented in Chapters 3 – 6. The study of ribbon stability between bare and passivated ribbons, fragmentation pathways, and bandgap variation or dependence upon width is contained in Chapter 3. The effects of ligands on work function, bandgap, and associated quantum states of the system are presented in Chapter 4. A comparison between chemical doping of phosphorene nanoribbons by varying concentration of Na surface atoms and charge transfer doping by ligated metal chalcogenide clusters is covered in Chapter 5. Finally, a discussion dedicated to related future works can be seen in Chapter 6.

References

1. Sagan, Carl. *Pale Blue Dot: A Vision of the Human Future in Space*. First Ballantine Books edition, Ballantine Books, 1997.
2. Novoselov, K. S. et al. Electric field effect in atomically thin carbon films. *Science* **306**, 666–669 (2004).
3. Akhtar, M., Anderson, G. et al. “Recent advances in synthesis, properties, and applications of phosphorene”. *npj 2D Materials and Applications* volume 1, Article number: 5 (2017)
4. Ashton, M.; Paul, J.; Sinnott, S. B.; Hennig, R. G. (2017). "Topology-Scaling Identification of Layered Solids and Stable Exfoliated 2D Materials". *Phys. Rev*
5. Prasad S.V.S., Mishra R.K., Gupta S., Prasad S.B., Singh S. (2021) Introduction, History, and Origin of Two Dimensional (2D) Materials. In: Singh S., Verma K., Prakash C. (eds) *Advanced Applications of 2D Nanostructures*. Materials Horizons: From Nature to Nanomaterials. Springer, Singapore.
6. Butler, S. Z. et al. Progress, challenges, and opportunities in two-dimensional materials beyond graphene. *ACS Nano* **7**, 2898–2926 (2013).
7. Bhimanapati, G. R. et al. Recent advances in two-dimensional materials beyond graphene. *ACS Nano* **9**, 11509–11539 (2015).
8. Thompson, Brianna C., et al. “Graphite Oxide to Graphene. Biomaterials to Bionics.” *Advanced Materials*, vol. 27, no. 46, Dec. 2015, pp. 7563–82. *DOI.org (Crossref)*, <https://doi.org/10.1002/adma.201500411>.
9. Duan, X., Wang, C., Pan, A., Yu, R. & Duan, X. Two-dimensional transition metal dichalcogenides as atomically thin semiconductors: opportunities and challenges. *Chem. Soc. Rev.* **44**, 8859–8876 (2015)
10. Gibaja, C. et al. Few-layer antimonene by liquid-phase exfoliation. *Angew. Chem. Int. Ed.* doi:10.1002/anie.201605298 (2016).
11. Ares, P. et al. Mechanical isolation of highly stable antimonene under ambient conditions. *Adv. Mater.* **28**, 6332–6336 (2016)
12. Li, Xinming et al. “Graphene and related two-dimensional materials: Structure-property relationships for electronics and optoelectronics.” *Applied physics reviews* 4 (2017): 021306.
13. Gosling, J.H., Makarovskiy, O., Wang, F. et al. Universal mobility characteristics of graphene originating from charge scattering by ionised impurities. *Commun Phys* **4**, 30 (2021). <https://doi.org/10.1038/s42005-021-00518-2>
14. Ferrari, A. C. et al. Science and technology roadmap for graphene, related two-dimensional crystals, and hybrid systems. *Nanoscale* **7**, 4598–4810 (2015).
15. Watts, Mitchell C., et al. “Production of Phosphorene Nanoribbons.” *Nature*, vol. 568, no. 7751, Apr. 2019, pp. 216–20. *DOI.org (Crossref)*, <https://doi.org/10.1038/s41586-019-1074-x>.
16. Li, L. K. et al. Black phosphorus field-effect transistors. *Nat. Nanotechnol.* **9**, 372–377 (2014).

17. Qiao, J. S., Kong, X. H., Hu, Z. X., Yang, F. & Ji, W. High-mobility transport anisotropy and linear dichroism in few-layer black phosphorus. *Nat. Commun.* **5**, 4475 (2014).
18. Liu, H. et al. Phosphorene: an unexplored 2D semiconductor with a high hole mobility. *ACS Nano* **8**, 4033–4041 (2014).
19. Xia, F. N., Wang, H. & Jia, Y. C. Rediscovering black phosphorus as an anisotropic layered material for optoelectronics and electronics. *Nat. Commun.* **5**, 4458 (2014).
20. Lee, S. et al. Anisotropic in-plane thermal conductivity of black phosphorus nanoribbons at temperatures higher than 100 K. *Nat. Commun.* **6**, 8573 (2015).
21. Sorkin, V., Cai, Y., Ong, Z., Zhang, G. & Zhang, Y. W. Recent advances in the study of phosphorene and its nanostructures. *Crit. Rev. Solid State Mater. Sci.* **42**, 1–82 (2017).
22. Lewis, E. A., Brent, J. R., Derby, B., Haigh, S. J. & Lewis, D. J. Solution processing of two-dimensional black phosphorus. *Chem. Commun. (Camb.)* **53**, 1445–1458 (2017).
23. Li, W. F., Yang, Y. M., Zhang, G. & Zhang, Y. W. Ultrafast and directional diffusion of lithium in phosphorene for high-performance lithium-ion battery. *Nano Lett.* **15**, 1691–1697 (2015).
24. Hongyan Guo, Ning Lu, Jun Dai, Xiaojun Wu, and Xiao Cheng Zeng. Phosphorene Nanoribbons, Phosphorus Nanotubes, and van der Waals Multilayers. *J. Phys. Chem. C* **118** (25), 14051-14059 (2014).
25. Cai, Y., Zhang, G. & Zhang, YW. Layer-dependent Band Alignment and Work Function of Few-Layer Phosphorene. *Sci Rep* **4**, 6677 (2014). <https://doi.org/10.1038/srep06677>
26. A. K. Geim and I. V. Grigorieva, *Nature* **499**, 419 (2013).
27. Liu, N. O. Weiss, X. Duan, H. Cheng, Y. Huang, and X. Duan, *Nat. Rev. Mater.* **1**, 16042 (2016).
28. Jariwala, T. J. Marks, and M. C. Hersam, *Nat. Mater.* **16**, 170 (2017).
29. S. Novoselov, A. Mishchenko, A. Carvalho, and A. H. Castro Neto, *Science* **353**, aac9439 (2016).
30. Ajayan, P. Kim, and K. Banerjee, *Phys. Today* **69**(9), 38 (2016).
31. Li and H. Zhu, *Phys. Today* **69**(9), 46 (2016).
32. McKinney, R. W., et al. Ionic vs. van der Waals layered materials: identification and comparison of elastic anisotropy, *J. Mater. Chem. A*, **2018**,**6**, 15828-15838
33. Toberer, Eric S., et al. “Electronic Structure and Transport in Thermoelectric Compounds AZn₂Sb₂ (A = Sr, Ca, Yb, Eu).” *Dalton Trans.*, vol. 39, no. 4, 2010, pp. 1046–54. DOI.org (Crossref), <https://doi.org/10.1039/B914172C>.
34. Preparation, Characterization and Electrochemical Properties of La₂CuO₄@Au as a Novel Bifunctional Oxygen Electrode.” *International Journal of Electrochemical Science*, Oct. 2020, pp. 9933–39. DOI.org (Crossref), <https://doi.org/10.20964/2020.10.74>
35. Na, Junhong, et al. “Few-Layer Black Phosphorus Field-Effect Transistors with Reduced Current Fluctuation.” *ACS Nano*, vol. 8, no. 11, Nov. 2014, pp. 11753–62. DOI.org (Crossref), <https://doi.org/10.1021/nn5052376>.

36. Zhang, J., et al. "Phosphorene Nanoribbon as a Promising Candidate for Thermoelectric Applications." *Scientific Reports*, vol. 4, no. 1, Dec. 2014, p. 6452. DOI.org (Crossref), <https://doi.org/10.1038/srep06452>.
37. Guo, Hongyan, et al. "Phosphorene Nanoribbons, Phosphorus Nanotubes, and van Der Waals Multilayers." *The Journal of Physical Chemistry C*, vol. 118, no. 25, June 2014, pp. 14051–59. DOI.org (Crossref), <https://doi.org/10.1021/jp505257g>
38. Ploog, Klaus, and Gottfried H. Döhler. "Compositional and Doping Superlattices in III-V Semiconductors." *Advances in Physics*, vol. 32, no. 3, Jan. 1983, pp. 285–359. DOI.org (Crossref), <https://doi.org/10.1080/00018738300101561>.
39. Tran, Vy, and Li Yang. "Scaling Laws for the Band Gap and Optical Response of Phosphorene Nanoribbons." *Physical Review B*, vol. 89, no. 24, June 2014, p. 245407. DOI.org (Crossref), <https://doi.org/10.1103/PhysRevB.89.245407>.
40. W. D. Knight, K. Clemenger, W. A. de Heer, W. A. Saunders, M. Y. Chou, and M. L. Cohen, *Phys. Rev. Lett.* **52**, 2141 (1984).
41. Knight, W. D., et al. "Alkali Metal Clusters and the Jellium Model." *Chemical Physics Letters*, vol. 134, no. 1, Feb. 1987, pp. 1–5. DOI.org (Crossref), [https://doi.org/10.1016/0009-2614\(87\)80002-7](https://doi.org/10.1016/0009-2614(87)80002-7).
42. Khanna, Shiv N., et al. "The Superatomic State beyond Conventional Magic Numbers: Ligated Metal Chalcogenide Superatoms." *The Journal of Chemical Physics*, vol. 155, no. 12, Sept. 2021, p. 120901. DOI.org (Crossref), <https://doi.org/10.1063/5.0062582>.
43. Reber, Arthur C., and Shiv N. Khanna. "Co6Se8(PET3)6 Superatoms as Tunable Chemical Dopants for Two-Dimensional Semiconductors." *Npj Computational Materials*, vol. 4, no. 1, Dec. 2018, p. 33. DOI.org (Crossref), <https://doi.org/10.1038/s41524-018-0092-9>.
44. Martin, T. P., et al. "Shell Structure of Clusters." *The Journal of Physical Chemistry*, vol. 95, no. 17, Aug. 1991, pp. 6421–29. DOI.org (Crossref), <https://doi.org/10.1021/j100170a009>.
45. Khanna, S. N., and P. Jena. "Atomic Clusters: Building Blocks for a Class of Solids." *Physical Review B*, vol. 51, no. 19, May 1995, pp. 13705–16. DOI.org (Crossref), <https://doi.org/10.1103/PhysRevB.51.13705>.
46. Chauhan, Vikas, et al. "Metal Chalcogenide Clusters with Closed Electronic Shells and the Electronic Properties of Alkalis and Halogens." *Journal of the American Chemical Society*, vol. 139, no. 5, Feb. 2017, pp. 1871–77. DOI.org (Crossref), <https://doi.org/10.1021/jacs.6b09416>.
47. Reber, Arthur C., et al. "Transforming Redox Properties of Clusters Using Phosphine Ligands." *The Journal of Physical Chemistry C*, vol. 123, no. 14, Apr. 2019, pp. 8983–89. DOI.org (Crossref), <https://doi.org/10.1021/acs.jpcc.9b00039>.
48. Harbola, M. K. "Magic Numbers for Metallic Clusters and the Principle of Maximum Hardness." *Proceedings of the National Academy of Sciences*, vol. 89, no. 3, Feb. 1992, pp. 1036–39. DOI.org (Crossref), <https://doi.org/10.1073/pnas.89.3.1036>.
49. D. E. Bergeron, P. J. Roach, A. W. Castleman, N. O. Jones, and S. N. Khanna, *Science* **307**, 231 (2005).
50. D. E. Bergeron, A. W. Castleman, T. Morisato, and S. N. Khanna, *Science* **304**, 84 (2004).

51. J. U. Reveles, S. N. Khanna, P. J. Roach, and A. W. Castleman, Proc. Natl. Acad. Sci. U. S. A. 103, 18405 (2006).
52. A. C. Reber, S. N. Khanna, and A. W. Castleman, J. Am. Chem. Soc. 129, 10189 (2007).
53. Spear, W. E. & Le Comber, P. G. Substitutional doping of amorphous silicon. Solid State Commun. 17, 1193–1196 (1975).
54. Erwin, S. C. et al. Doping semiconductor nanocrystals. Nature 436, 91–94 (2005).
55. Yu, J. et al. Patterning superatom dopants on transition metal dichalcogenides. Nano Lett. 16, 3385–3389 (2016).
56. J. Yu, C.-H. Lee, D. Bouilly, M. Han, P. Kim, M.L. Steigerwald, X. Roy, and C. Nuckolls. Nano Lett., 16, 3385 (2016), X. Roy, C.-H. Lee, A.C. Crowther, C.L. Schenck, T. Besara, et al., Science 341, 157 (2013)
57. Wang, Q. H., Kalantar-Zadeh, K., Kis, A., Coleman, J. N. & Strano, M. S. Electronics and optoelectronics of two-dimensional transition metal dichalcogenides. Nat. Nanotechnol. 7, 699–712 (2012).
58. Kiriya, D., Tosun, M., Zhao, P., Kang, J. S. & Javey, A. Air-stable surface charge transfer doping of MoS₂ by benzyl viologen. J. Am. Chem. Soc. 136, 7853–7856 (2014).
59. Schellenberger, A., Schlaf, R., Pettenkofer, C. & Jaegermann, W. Synchrotroninduced surface-photovoltage saturation at intercalated NaWSe₂ interfaces. Phys. Rev. B 45, 3538–3545 (1992).
60. Perdew, J. P., Burke, K. & Ernzerhof, M. Generalized gradient approximation made simple. Phys. Rev. Lett. 77, 3865–3868 (1996).
61. Krukau, A. V., Vydrov, O. A., Izmaylov, A. F. & Scuseria, G. E. Influence of the exchange screening parameter on the performance of screened hybrid functionals. J. Chem. Phys. 125, 224106 (2006).
62. Ling, Xi, et al. “The Renaissance of Black Phosphorus.” *Proceedings of the National Academy of Sciences*, vol. 112, no. 15, Apr. 2015, pp. 4523–30. DOI.org (Crossref), <https://doi.org/10.1073/pnas.1416581112>.
63. Welch, Eric J., and Jeffrey R. Long. “Atom-Like Building Units of Adjustable Character: Solid-State and Solution Routes to Manipulating Hexanuclear Transition Metal Chalcogenide Clusters.” *ChemInform*, vol. 37, no. 2, Jan. 2006. DOI.org (Crossref), <https://doi.org/10.1002/chin.200602221>.
64. Hafner, Juergen. “ChemInform Abstract: Ab-Initio Simulations of Materials Using VASP: Density-Functional Theory and Beyond.” *ChemInform*, vol. 39, no. 47, Nov. 2008. DOI.org (Crossref), <https://doi.org/10.1002/chin.200847275>.
65. Yang, Y., Castano, C. E., Gupton, B. F., Reber, A. C. & Khanna, S. N. A fundamental analysis of enhanced cross-coupling catalytic activity for palladium clusters on graphene supports. Nanoscale 8, 19564–19572 (2016).
66. Yang, Y. et al. More than just a support: graphene as a solid-state ligand for palladium-catalyzed cross-coupling reactions. J. Catal. 360, 20–26 (2018).
67. Grimme, S. Semiempirical GGA-type density functional constructed with a longrange dispersion correction. J. Comput. Chem. 27, 1787–1799 (2006).
68. Kresse, G. & Furthmüller, J. Efficient iterative schemes for ab initio total-energy calculations using a plane-wave basis set. Phys. Rev. B 54, 11169–11186 (1996).

69. Neugebauer, J. & Scheffler, M. Adsorbate-substrate and adsorbate-adsorbate interactions of Na and K adlayers on Al(111). *Phys. Rev. B* 46, 16067–16080 (1992).
70. Roberts, F. S., Anderson, S. L., Reber, A. C. & Khanna, S. N. Initial and final state effects in the ultraviolet and X-ray photoelectron spectroscopy (UPS and XPS) of size-selected Pd_n clusters supported on TiO₂(110). *J. Phys. Chem. C* 119, 6033–6046 (2015).

Chapter 2. Density Functional Theory and Computational Methods

2.1 Introduction and Background

Density functional theory (DFT) is the basis for modern computational quantum mechanical methods and has led to the ability to perform complex calculations to determine, principally, the ground state electronic structures of many-body systems. However, it has not always held this position with unwavering support from the scientific community. In fact, there had been outright dismissal of the methods proposed in DFT by quantum chemists until the 1990s when the exchange-correlation functionals underwent significant refinement by Perdew and coworkers.[12,14,40] However, after their enhancement, these methods have led to the development of numerous software packages which make possible diverse theoretical exploration of physics, chemistry, and materials science. Theoretical modelling has proven predictive power as well as the capacity for aiding experimentalists in determining the inner workings of observed, novel physical or chemical properties. Thus, through collaborative and explorative efforts, the advent and application of DFT has led to a better understanding of the physical world in which we reside. As such, contributions of theoretical scientists have played a significant role in the development of better technologies utilized by the modern world today.[1-3] Consequently, we may not understate the utility of DFT and the value of continued contributions from the world of computational physics and chemistry.

2.2 The Schrodinger Equation:

Much of modern quantum mechanics rests on the shoulders of Erwin Schrodinger. His adaptation of Newton's second law led to the development of a wave equation whose evolution over time gives the quantum mechanical details about the path some isolated physical system takes with time. Specifically, that the behavior of electrons within atoms could be treated mathematically as matter waves was theorized in 1925 and published in 1926. His seminal work proved a vital interpretation of the wave-nature of the electron and successfully reproduced the spectral energies of hydrogen. Soon after, Max Born effectively interpreted the wave function as the probability amplitude while noting its modulus squared equates to the probability density. [6] Pertinent to the development of DFT, is the time-independent Schrodinger equation which, for a system with N electrons and M nuclei, is expressed in equation (2.1).

$$\hat{H}\Psi\left(\vec{x}_1, \vec{x}_2, \dots, \vec{x}_N, \vec{R}_1, \vec{R}_2, \dots, \vec{R}_M\right) = E\Psi\left(\vec{x}_1, \vec{x}_2, \dots, \vec{x}_N, \vec{R}_1, \vec{R}_2, \dots, \vec{R}_M\right) \quad 2.1$$

Where, \hat{H} , the Hamiltonian operator, is an observable which gives the total energy of the system as a sum of the operators associated with the kinetic and potential energies of the system, E is the corresponding energy eigenvalue, and ψ represents the wavefunction of the total system. Expanding the Hamiltonian Operator, \hat{H} , into its constituent parts in atomic units is given by equation (2.2).

$$\hat{H} = -\frac{1}{2} \sum_{i=1}^N \nabla_i^2 - \frac{1}{2} \sum_{A=1}^M \frac{\nabla_A^2}{M_A} - \sum_{i=1}^N \sum_{A=1}^M \frac{Z_A}{r_{iA}} + \sum_{i=1}^N \sum_{j>i}^N \frac{1}{r_{ij}} + \sum_{A=1}^M \sum_{B>A}^M \frac{Z_A Z_B}{R_{AB}} \quad 2.2$$

Note, the first two terms in Eq. 2.2 describe the kinetic energy of the electrons and nuclei respectively while the latter three terms represent the attractive electrostatic potential

between nuclei and electrons, repulsive electrostatic potential associated with electron-electron interactions, and the repulsive potential between nuclei. A first approximation to simplify the Hamiltonian considers the significant difference in mass between electrons and nuclei in the system. Known as the Born-Oppenheimer approximation, electrons are treated as a sea of electrons moving among a background of positive, spatially fixed nuclei. Since the nuclei are approximately stationary relative to the electrons, we may assume the kinetic energy of the nuclei approaches zero and the nuclear potential term to be a constant. Thus, the second term of the Hamiltonian vanishes and the expression can be reduced as follows in Equation 2.3,

$$\hat{H}_e = -\frac{1}{2} \sum_{i=1}^N \nabla_i^2 - \sum_{i=1}^N \sum_{A=1}^M \frac{Z_A}{r_{iA}} + \sum_{i=1}^N \sum_{j>i}^N \frac{1}{r_{ij}} = \hat{T} + \hat{V}_{Ne} + \hat{V}_{ee} \quad 2.3$$

where N and e denote nucleus and electron respectively. The exact solution to many-body Schrödinger equation given by Eq. 2.1. is considered the pinnacle of ab initio computational materials science. This would give us a wealth of information about every electron interaction within the system, including the exact details of the ground state energy of the system. The simplicity of this many-body Schrodinger equation is deceptive as, even with this first approximation, it remains entirely unsolvable. For example, if we take a 5-electron sample system on a 10x10x10 grid, data storage alone required to store the many-body wave function dependent upon all of the electronic spatial coordinates is on the order of 10 petabytes. (7) A proposed method for working around this problematic search for exact solutions is to map the wave function which depends on all spatial coordinates of all electrons in a system to a single electron.[7] This is called the one-

electron theory, and can be attributed to the work of Hohenberg and Kohn.[7-10] The Hohenberg-Kohn theorem declares that all ground state properties of a system may be attributed to the density of that system. As such, the ground state energy exists as a functional of the electronic density. Thus, if we can determine the electron density then we may also solve the total energy of the system. This greatly simplifies the many-body Schrodinger equation because the electron density only depends upon one spatial coordinate. Anything that is unknown about the system is grouped together into the exchange-correlation functional which is also a functional of the electron density. In this way, all of quantum mechanics is packed into these two terms which we know exist but have not yet defined. Thus, utilizing the system's electron density as the fundamental parameter to determine the quantum mechanical properties of the system remains quite an attractive approach from a practical standpoint. Not only is the electron density an observable parameter, thus experimentally obtainable, but the density functional approach leads to a computationally tractable minimization of energy for small systems. Let us dive deeper and observe the individual pillars of modern density functional theory in the subsequent sections, beginning with the definition of the electron density.

2.3 The Electron Density:

Recall from introductory quantum mechanics the wavefunction, ψ , mentioned in section 2.1, is not an observable quantity as it represents the probability amplitude of a particular electron in the system. However, the modulus squared of the wavefunction represents the probability density of electrons and is therefore directly related to the systems electron density which can be obtained experimentally via X-ray diffraction (XRD). Since electrons are indistinguishable from one another, for any N electron system

the total electron density may be defined as N times the integral of the wavefunction modulus squared (probability density) with respect to all possible spin coordinates ($\mathbf{d}s_1$) and all but one spatial coordinate, ($\vec{x} \equiv \vec{r} \cdot \mathbf{s}$) shown below:

$$\rho(\vec{r}) = N \int \int \cdots \int |\Psi(\vec{x}_1, \vec{x}_2, \cdots, \vec{x}_N,)|^2 ds_1 d\vec{x}_2 d\vec{x}_3 \cdots d\vec{x}_N \quad 2.4$$

Where, $\rho(\vec{r})$ now defines the probability of finding any electron (N) within a volume element of $d\vec{r}$ with arbitrary spin. All other electrons within the system (N-1) also have arbitrary positions and spin where the state is defined by wavefunction ψ . Though the quantity, $\rho(\vec{r})$, obtained by solving Eq. 2.4 represents the probability density, it is commonly referred to as the electronic density and the function obeys the following criteria [5]:

- a) The function $\rho(\vec{r})$ integrates to an integer N , total number of electrons in the system and vanishes at infinity

$$\begin{aligned} \rho(\vec{r} \rightarrow \infty) &= 0 \\ \int \rho(\vec{r}) d\vec{r} &= N \end{aligned} \quad 2.5$$

- b) At the nucleus of any atom or molecule within a material the electron density reaches a finite value resulting in a discontinuity. To avoid any blowups of Hamiltonian terms as a result of this cusp; the specific cusp condition is given below,

$$\lim_{r_{iA} \rightarrow 0} \left[\frac{\partial}{\partial r} + 2Z_A \right] \bar{\rho}(\vec{r}) = 0 \quad 2.6$$

where $\bar{\rho}(\vec{r})$ is the spherical average of $\rho(\vec{r})$.

- c) The final important result is the long-range law for electron density which states the asymptotic exponential decay of the electronic density for large distances, or, as $\vec{r} \rightarrow \infty$. [5]

2.7

$$\rho(\vec{r}) \propto \exp\left[-2\sqrt{2I}|\vec{r}|\right]$$

Importantly, the probability of finding two electrons simultaneously whose spin states are σ_1 and σ_2 within two different volume elements dr_1 and dr_2 respectively is given by Eq. 2.8,

$$\rho_2(\vec{x}_1, \vec{x}_2) = N(N-1) \int \int \cdots \int |\psi(\vec{x}_1, \vec{x}_2, \cdots \vec{x}_N)|^2 d\vec{x}_3 \cdots d\vec{x}_N \quad 2.8$$

The remainder of the electrons in the system are treated with arbitrary position and spin. Note, the pair density is positive and normalized to the total number of non-distinct electron pairs. [5, 11] Now that we have a better idea for what parameterizes the electron density, let us inspect the first of several founding ideas which comprise modern DFT – The Thomas-Fermi Model.

2.4 The Thomas-Fermi Model:

A first approach utilizing the density functional was proposed by Llewellyn Thomas and Enrico Fermi in 1927. [5,6] As mentioned in previous sections, utilization of the density functional approach greatly reduces the computational cost required to solve the energy minimization problem. It can be measured experimentally and depends only on

the spatial variables of the wavefunction mapped to a single electron, thus, decreasing the number of variables from $4N$ for an N -electron system ($3N$ related to spatial and N related to spin), to N . Thus, for small systems like molecules the calculations become possible. Thomas and Fermi were the first to propose a density functional-based model which utilized the uniform electron gas approximation in order to derive the quantum mechanical kinetic energy of the system. The accuracy of the model is flawed, however, as all other energetic contributions within the system (attractive nuclear potential, and electron repulsion) are considered classically. The power and significance of this model lies in the proof that a density functional-based approach could be used to obtain a result.

Eq 2.9 represents the T-F kinetic energy:

$$T_{TF}[\rho(\vec{r})] = \frac{3}{10}(3\pi^2)^{\frac{2}{3}} \int \rho(\vec{r})^{\frac{5}{3}} d\vec{r} \quad 2.9$$

Where, adding the classical contributions, we have the following expression for total energy E_{TF} ,

$$E_{TF}[\rho(\vec{r})] = \frac{3}{10}(3\pi^2)^{\frac{2}{3}} \int \rho(\vec{r})^{\frac{5}{3}} d\vec{r} - Z \int \frac{\rho(\vec{r})}{r} d\vec{r} + \frac{1}{2} \int \int \frac{\rho(\vec{r}_1)\rho(\vec{r}_2)}{r_{12}} d\vec{r}_1 d\vec{r}_2 \quad 2.10$$

Considering the extent of these estimations as well as the exclusion of the exchange and correlation effects it does not require much effort to discern the lack of accuracy in solutions obtained with this approach. Again, the significance is in the first representation of the total energy of the system using only the electron density. Given the evidence against the presented method and the lack of justification for the proposed method at the time, the importance of the preliminary work by Thomas and Fermi cannot be understated in its importance and influence in modern computational solid-state physics and materials

science. It wasn't until the work of Hohenberg and Kohn and later Kohn and Sham in the 1960s that the density functional approach took another leap forward.

2.5 The Hohenberg-Kohn Theorems

Hohenberg and Kohn's postulates published in their seminal paper in 1964 mark the birth of modern density functional theory. These two theorems provide justification of Thomas and Fermi's earlier model as well as lay the fundamental theoretical groundwork necessary to utilize a density functional approach for rigorous quantum mechanical investigation of solid-state materials. The two theorems apply to any system of electrons moving under the influence of some external potential.[5,6,8-11]

1. The ground state energy of the system is a unique functional of the electron density of the system.[5,6,8-11]

Corollary 1: The ground state density uniquely determines the potential and therefore all knowable properties of the system including the many body wavefunction.

Corollary 2: Since the energy of the system is a functional of the ground state electron density, the spectrum of the Hamiltonian is also a unique functional of the ground state charge density.[5,6,8-11]

2. The electron density that minimizes the energy of the overall functional is the true electron density corresponding to the full solution of the Schrodinger equation. [5,6,8-11] These theorems were first applied to the stationary, time independent ground state but later adapted for time dependent consideration as well.[5,6,8-11]

While the proposed theorems by Hohenberg and Kohn seem a viable path one might take to arrive at the ground state energy of some system, the validity must be proven.

The proof of the first theorem lies in showing that the energy can indeed be written as a functional of the electron density, while proof of the second theorem must say something about what form the density functional takes. First, recall the Born-Oppenheimer approximation as discussed in section 2.1 which utilizes the relatively heavy mass of nuclei to adjust the electronic Hamiltonian to what is given by Equation 2.3. Now, the ground state energy of the system is directly related to the potential associated with the nuclei within the system – called the external potential. It states that the ground-state electron density $\rho(\vec{r})$ of an electronic system distinctively determines an external potential ($V_{ext}(\vec{r})$) acting on the electrons up to an additive constant. This theorem creates a one-to-one correspondence between the ground-state electron density and the external potential. Quite significantly, this reduces the dimensionality of the problem for a 100 Pt atom system with 78 valence e^- , each with three spatial dimensions, from a total of 23,400 dimensions in the wave function regime to a reliance on just three spatial dimensions.[11] Recall, from Equation 2.5, integrating the electron density $\rho(\vec{r})$ within some volume $d\vec{r}$ yields the integer number of electrons within the system defined by the specified volume,

$$\begin{aligned} \rho(\vec{r} \rightarrow \infty) &= 0 \\ \int \rho(\vec{r}) d\vec{r} &= N \end{aligned}$$

Now, assume $\rho(\vec{r})$ represents the exact ground state density for some non-degenerate system, while ψ is the ground state wavefunction. Furthermore, assume there exist two potentials, $V_{ext}(\vec{r})$ and $V'_{ext}(\vec{r})$, varying by more than just a constant, which give rise to the same ground state density. These two potentials correspond to distinct Hamiltonians, $H(\vec{r})$ and $H'(\vec{r})$, and distinct wavefunctions, $\psi_{ext}(\vec{r})$ and $\psi'_{ext}(\vec{r})$. The variational

principle states that no wavefunction may give an energy that is less than that of $\psi_{ext}(\vec{r})$ for $\mathbf{H}(\vec{r})$. In other words,

$$E_0 = \langle \psi | H | \psi \rangle < \langle \psi' | H | \psi' \rangle \quad 2.11$$

Now, utilizing the variational principle, computing the expectation value of $\psi'_{ext}(\vec{r})$ with $\mathbf{H}(\vec{r})$ yields the following,

$$\begin{aligned} E_0 < \langle \psi' | H | \psi' \rangle &= \overbrace{\langle \psi' | H' | \psi' \rangle}^{E'_0} + \langle \psi' | H - H' | \psi' \rangle \quad 2.12 \\ &= E'_0 + \int \rho(\vec{r}) [\hat{V}_{ext} - \hat{V}'_{ext}] d\vec{r} \end{aligned}$$

Similarly, exchanging labels in Eq. 2.12 to find the expectation value of $\psi_{ext}(\vec{r})$ with $\mathbf{H}'(\vec{r})$, we have,

$$\begin{aligned} E'_0 < \langle \psi | H' | \psi \rangle &= \underbrace{\langle \psi | H | \psi \rangle}_{E_0} + \langle \psi | H' - H | \psi \rangle \quad 2.13 \\ &= E_0 - \int \rho(\vec{r}) [\hat{V}_{ext} - \hat{V}'_{ext}] d\vec{r} \end{aligned}$$

By adding Equations 2.12 and 2.13 we obtain,

$$E_0 + E'_0 < E'_0 + E_0 \quad 2.14$$

The solution given by Equation 2.14 is clearly contradictory. As such, theorem 1 has been proven via *reductio ad absurdum*, and there must be a unique $\rho(\vec{r})$ which corresponds to the ground state energy of the system and therefore a single $V_{ext}(\vec{r})$.

Now, since we have shown that the external potential is uniquely determined by the density of the system and, since this external potential subsequently determines the ground

state wavefunction, $\rho(\vec{r})$ also uniquely determines all other energetic properties of the ground state such as the electron kinetic energy, $T(\rho)$, and electron interaction energy, E_{ee} .

As such, we may write the total energy of the ground state as a functional of the density like so,

$$E[\rho] = \underbrace{E_{Ne}[\rho]}_{\text{system dependent}} + \underbrace{T[\rho] + E_{ee}[\rho]}_{\text{universal}} \quad 2.15$$

Note, we have grouped the terms according to their relation to a particular system, or, as universal terms independent of system. The first term represents the system-dependent attractive potential energy between nuclei and electrons while the universal energy terms include the kinetic energy of electrons and repulsive potential associated with electron interactions. Equation 2.15 may be transformed further by grouping the system-independent terms into a single universal functional, F_{HK} , as follows:

$$\begin{aligned} E[\rho] &= E_{Ne}[\rho] + F_{HK}[\rho] \\ &= \int \rho(\vec{r}) \hat{V}_{Ne}(\vec{r}) d\vec{r} + F_{HK}[\rho] \end{aligned} \quad 2.16$$

This universal, F_{HK} , depends only on the density and, mathematically, remains independent from any system under observation. Though simple, the universal functional proves fundamentally vital to DFT calculations; If its explicit form is known, exact solutions to the Schrodinger equation may be found. Alas, the exact form is yet unknown and presently proves one of the great challenges in DFT research. The electric potential can, however, be expanded in the interest of progressing toward a more exact form and

subsequently more accurate solutions to the ground state properties. Separating the electronic potential into a classical Coulombic interaction term, $J(\rho)$, and a non-classical self-interaction correction and exchange, E_{ncl} due to the error from the sum of Coulomb and exchange self-interactions of the electron, we have the following,

$$\begin{aligned}
 E_{ee}[\rho] &= \frac{1}{2} \int \int \frac{\rho(\vec{r}_1)\rho(\vec{r}_2)}{r_{12}} d\vec{r}_1 d\vec{r}_2 + E_{ncl}[\rho] \\
 &= J[\rho] + E_{ncl}[\rho]
 \end{aligned}
 \tag{2.17}$$

While the first Hohenberg-Kohn theorem proves that the energy of the system may indeed be written as a functional of the electron density, and as such, there exists a particular density which is associated with the ground state of a system, we do not have any notion about how to determine this particular density. We do know that the ground state energy can be defined by a unique ground state density. Thus, in theory, it is possible to utilize the variational principle to vary the density until arriving at a global energy minimum. The second theorem tells us that $E(\rho)$ acts as an upper bound to the ground state energy, E_0 , meaning that any other density than the ground state density will produce an associated energy higher than that of the global minimum. In other words, a trial density, $\tilde{\rho}(\vec{r})$, which satisfies the necessary boundary conditions,

$$\begin{aligned}
 \tilde{\rho}(\vec{r}) &\geq 0, \\
 \int \tilde{\rho}(\vec{r}) d\vec{r} &= N,
 \end{aligned}$$

corresponds to some \tilde{V}_{ext} and yields an energy value $E(\tilde{\rho})$ greater than or equal to that of the ground state energy $E_0(\rho_0)$:

$$E_0[\rho_0] \leq E[\tilde{\rho}] = E_{Ne}[\tilde{\rho}] + T[\tilde{\rho}] + E_{ee}[\tilde{\rho}] \quad 2.18$$

Given the correspondence between the density and Hamiltonian to some wavefunction, we may utilize the related wavefunction as a trial wavefunction. As well we may use the Hamiltonian associated with the true external potential, to obtain the resulting expectation value of the energy:

$$\begin{aligned} \langle \tilde{\psi} | \hat{H} | \tilde{\psi} \rangle &= T[\tilde{\rho}] + E_{ee}[\tilde{\rho}] + \int \tilde{\rho}(\vec{r}) d\vec{r} \\ &= E[\tilde{\rho}] \geq E_0[\rho_0] = \langle \psi_0 | \hat{H} | \psi_0 \rangle. \end{aligned} \quad 2.19$$

It is important to note that the density discussed in the previous sections is defined by distinct criteria:

1. The summation to integer, N , total electrons or N -representability.[5,6,11]
2. The association of the density with some external potential, V_{ext} .[5,6,11]

The first condition is met simply by ensuring the density originates from an antisymmetrized wavefunction. The second condition is not so trivial, however, as not all possible densities map directly to some antisymmetrized wavefunction. Thus, they cannot have the necessary direct correlation to V_{ext} . In other words, though the first condition is easily met, not all densities inherently abide by this condition and must be discerned accordingly. This has been shown by the work of Levy and Lieb and remains an area of study presently in the interest of finding trial densities which meet the second condition to provide more accurate results.[13,14]

2.6 The Kohn Sham Method:

While Hohenberg Kohn methods were integral in building the framework for adapting the density functional theory from its initial formulation laid out by Thomas and Fermi, they lacked a formalism for computing the energy minimization as well as a process for calculating appropriate densities abiding by the criteria defined in the previous section. Kohn and Sham developed an approach which avoided one of the main limitations of the Hohenberg-Kohn theorems, namely, the inaccuracy of the kinetic energy term contained within the critical universal function $F(\rho)$ defined in section 2.4,

$$F[\rho] = T[\rho] + J[\rho] + E_{ncl}[\rho]. \quad 2.20$$

In 1965 Kohn and Sham proposed calculating the kinetic energy from a known wave function for a reference, non-interacting system yet, whose density would be the same as a real interacting system. This kinetic energy expression is given as,

$$T_S = -\frac{1}{2} \sum_i^N \langle \psi_i | \nabla^2 | \psi_i \rangle, \quad 2.21$$

which yields the following expression for the electron density,

$$\rho_S(\vec{r}) = \sum_i^N \sum_s |\psi_i(\vec{r}, s)|^2 = \rho(\vec{r}) \quad 2.22$$

where ψ_i represents the wavefunction from the reference system. We note $T_S \neq T(\rho)$ even for the same electron density. However, the majority of $T(\rho)$ is expected to be preserved in T_S . Kohn and Sham's proposed correction for this inequality is grouping that which is unknown into a new term within the universal function $F(\rho)$, called the **Exchange-Correlation Energy**.

$$F[\rho] = T_S[\rho] + J[\rho] + E_{XC}[\rho], \quad 2.23$$

which is expressed as the sum of differences between terms in respective models yielding,

$$E_{XC}[\rho] = (T[\rho] - T_S[\rho]) + (E_{ee}[\rho] - J[\rho]). \quad 2.24$$

In this way, Kohn and Sham have packaged all that is unknown about a particular system into a single term, $E_{XC}(\rho)$, which approximates the difference between the reference and real systems as well as decreases the computational load. These unknowns, like the electron exchange energy, electron correlation, residual kinetic energy, and a self-interaction correction, are ignored in the energy minimization calculations and left for approximating as a whole. Presently, a great number of accurate approximations exist for the exchange-correlation functional e.g. the Local Density Approximation (LDA), Generalized Gradient Approximation (GGA), a variety of Hybrids, and meta-GGA.

Returning to the business of finding the associated potential, V_S , of the aforementioned non-interacting reference system, we are still tasked with obtaining an antisymmetrized wavefunction (Slater determinant) associated with the exact density from our particular real system of interest. To begin, Kohn and Sham list the new energy expression as follows:

$$E[\rho] = T_S[\rho] + J[\rho] + E_{XC}[\rho] + E_{Ne}[\rho] \quad 2.25$$

Expanding each term yields,

$$E[\rho] = T_S[\rho] + J[\rho] + E_{XC}[\rho] + E_{Ne}[\rho]$$

$$\begin{aligned}
&= -\frac{1}{2} \sum_i^N \langle \psi_i | \nabla^2 | \psi_i \rangle + \frac{1}{2} \sum_i^N \sum_j^N \int \int |\psi_i(\vec{r}_1)|^2 \frac{1}{r_{12}} |\psi_j(\vec{r}_2)|^2 d\vec{r}_1 d\vec{r}_2 \\
&\quad + E_{XC}[\rho] - \sum_i^N \int \sum_A^M \frac{Z_A}{r_{1A}} |\psi_i(\vec{r}_1)|^2 d\vec{r}_1
\end{aligned} \tag{2.26}$$

where the only unknown remains the exchange-correlation term $E_{XC}(\rho)$. Applying the variational principle on Equation 2.26 finally gives the famed Kohn-Sham equations under the constraint, $\langle \psi_i | \psi_j \rangle = \delta_{ij}$,

$$\left(-\frac{1}{2} \nabla^2 + \underbrace{\left[\int \frac{\rho(\vec{r}_2)}{r_{12}} d\vec{r}_2 + \hat{V}_{XC}(\vec{r}_1) - \sum_A^M \frac{Z_A}{r_{1A}} \right]}_{V_{eff}(\vec{r}_1)} \right) \psi_i = \epsilon_i \psi_i \tag{2.27}$$

where \hat{V}_{XC} can be defined as the functional derivative of the exchange-correlation energy with respect to the density,

$$\hat{V}_{XC}(\vec{r}) = \frac{\partial E_{XC}[\rho(\vec{r})]}{\partial \rho(\vec{r})} \tag{2.28}$$

Note, in the Kohn-Sham operator, the effective potential, V_{eff} , depends only on \vec{r} instead of the index over all electrons within the system thus, greatly simplifying matters. Orbitals obtained from Equation 2.22 are used to compute the following total density shown in Equation 2.29:

$$\rho(\vec{r}) = \sum_{i=1}^N |\psi_i(\vec{r})|^2 \quad 2.29$$

This density can, in turn, be used to begin the cycle again to obtain a new effective potential and continued until the calculation reaches self-consistency – the condition in which the beginning density leads to a final density of the exact same form. It would be remiss not to mention that the Kohn-Sham orbitals, $\psi_i(\vec{r})$, do not translate to any physical meaning and are not equivalent to the actual electronic orbitals within a system. They do, however, effectively lead to an accurate approximation of the ground state energy and other physical properties of a system through the previously mentioned self-consistency cycle. This process can be visualized by referring to the pictograph in Figure 2.1.

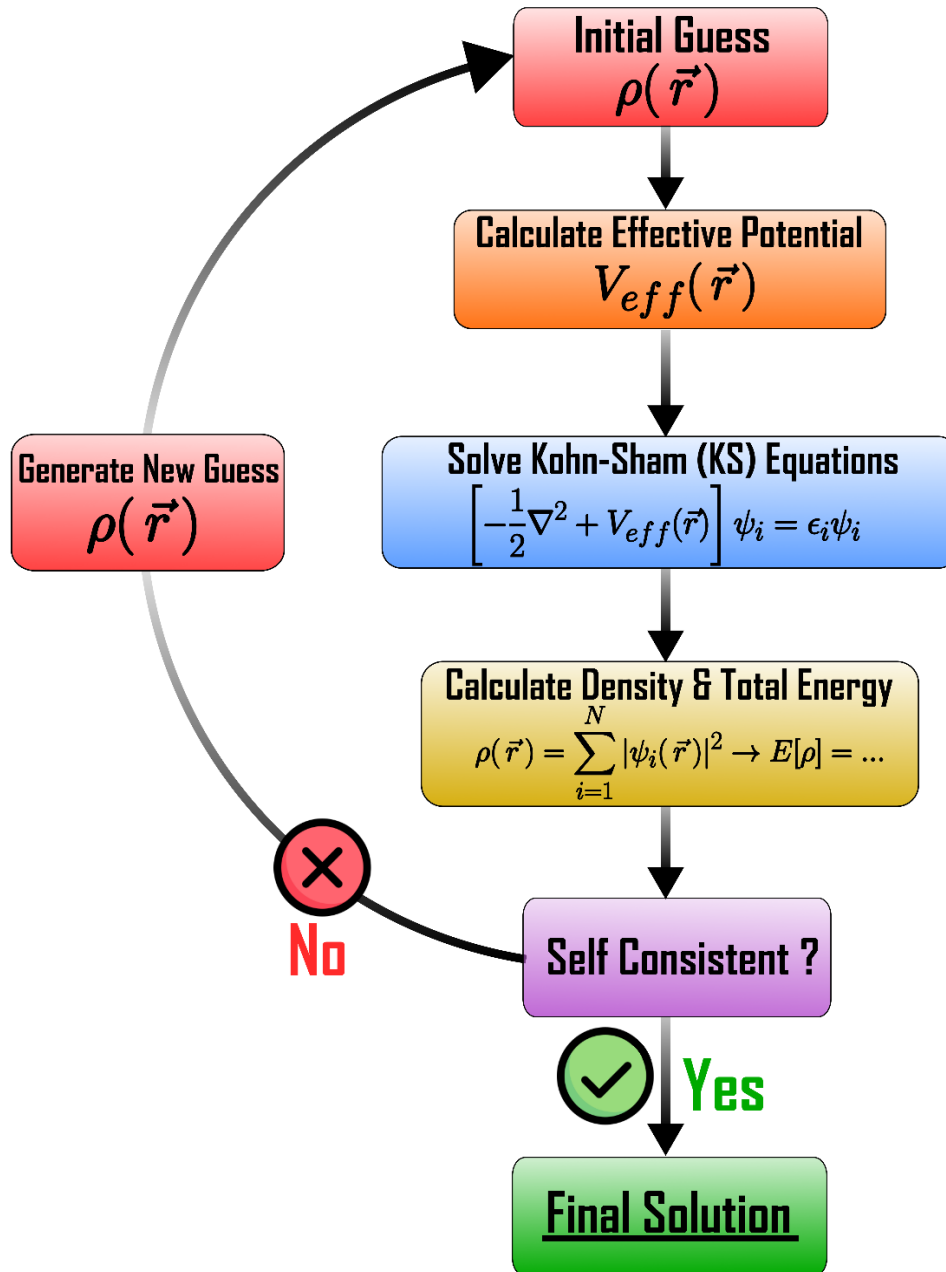


Figure 2.1. Kohn-Sham DFT flow chart depicting the self-consistency method for energy minimization.

There remains one final artifact which arises from the treatment of the exchange-correlation functionals, whose general form is expressed in Equation 2.23 – The idea of **Self-interaction correction** to the exchange-correlation energy. Recall, the density functional formalism relies on mapping to a one-electron system. In a physically real

equivalent, the hydrogen atom, the energy of the system clearly depends solely on the kinetic energy of the electron and the external potential of the nucleus. In this system, there obviously can be no electron-electron interactions. This seems a painfully trivial observation until one considers the energy expression for a one-electron system governed by the Kohn-Sham approach which is indeed the exact same expression as the general form given by Equation 2.25:

$$E[\rho] = T_S[\rho] + J[\rho] + E_{XC}[\rho] + E_{Ne}[\rho]$$

Recall, the classical electrostatic repulsion term, $J[\rho]$, can be expressed as follows,

$$\frac{1}{2} \sum_i^N \sum_j^N \int \int |\psi_i(\vec{r}_1)|^2 \frac{1}{r_{12}} |\psi_j(\vec{r}_2)|^2 d\vec{r}_1 d\vec{r}_2$$

Now, since in this integral there is no restriction prohibiting $i = j$, this term does not completely vanish and results in Coulomb interaction of the density with itself.[27] For the one-electron system this results in a non-zero contribution from electron interaction which is a physically nonsensical result. [27] This error extends to other systems as well and in order to correct for this spurious inclusion we must mathematically constrain the repulsion term to be equivalent to the negative exchange-correlation energy, $E_{XC}[\rho]$, such that the false self-interaction cancels,

$$\frac{1}{2} \iint \frac{\rho(\vec{r}_1)\rho(\vec{r}_2)}{r_{12}} d\vec{r}_1 d\vec{r}_2 = -E_{XC}[\rho]$$

Herein lies a major obstacle in the density functional approach. In the Hartree-Fock scheme, the previous expression is satisfied. Yet, in any application of the Kohn-Sham approach, accounting for this self-interaction does not guarantee complete rectifying of energy mis-match.[27] In fact, the error is amplified in some cases, especially for many-

body systems since the approximations to the exchange-correlation energy are independent of repulsion term, $J[\rho]$. [27]

2.7 Exchange-Correlation Energy and Choice of Functional

We saw from the beautiful work of Hohenberg-Kohn-Sham DFT that the ground state energy of a reference system could be obtained by utilizing a self-consistent minimization of the energy functional which yields a self-consistent solution to a set of single particle equations.[11] Also, the work conveniently grouped all unknowns which separated our reference system from the real one into a single term called the exchange-correlation functional shown in Equation 2.27. However, there exists one major complication in an otherwise elegant formulation: in order to solve the Kohn-Sham equations we must explicitly define the exchange-correlation function. Herein lies the unique difficulty of density functional theory as the exact form of the elusive exchange-correlation functional is unknown. Fortunately, there is a model by which this functional can indeed be derived exactly. This toy system called the **uniform electron gas** treats the electron density as a constant at all points in space. Realistically, this approximation is a far cry from the delicate variations in electron density which give materials inherently interesting qualities. However, it does provide utility to theorists allowing for the use of the Kohn-Sham equations to build somewhat accurate models of real systems. Certainly, the most accurate way to estimate the exchange-correlation energy is the constraint search approach using mathematical conditions that precisely represent physical constraints of real systems yielding exact exchange and correlation energies. However, as described in the Jacob's ladder analogy by J. Perdew, the higher up one climbs, the greater the increase

in accuracy and complexity of the approximation and, subsequently, the greater the computational cost.[12] Modern DFT has produced a growing variety of viable exchange-correlation functionals which have been computed using Monte Carlo methods.[7,12] The discussion below outlines the major classes of exchange-correlation functionals with increasing complexity and accuracy.

2.7.1 Local Density Approximation (LDA)

The Local-density approximations (LDA) remain the simplest class of approximations as they depend solely on the electron density at specific points in space as opposed to derivatives of the density as seen in the Kohn-Sham orbitals in Section 2.5. The success of LDA lies in the approximation of the system's true inhomogeneous electronic density as a locally well-behaved homogeneous or uniform electron gas. As one might imagine this leads to accurately portrayed electron densities near nuclei within a real system, however, the more nuanced electron densities associated with chemical bonding are not well represented by the LDA. Nevertheless, the local-density approximation exists as a first step towards chemical accuracy.

For a spin-unpolarized system, in general, the local-density approximation (LDA) for the exchange-correlation energy is written as follows,

$$E_{xc}^{\text{LDA}}[\rho] = \int \rho(\mathbf{r}) \epsilon_{xc}(\rho(\mathbf{r})) d\mathbf{r} \quad 2.30$$

where ρ is the electronic density and ϵ_{xc} is the exchange-correlation energy per particle of a homogeneous electron gas of the same density. The exchange and correlation terms are then separated linearly as follows

$$E_{xc} = E_x + E_c \quad 2.31$$

The exchange term E_x correlates to the exchange energy of an electron interacting with a uniform electron gas, of particular density, which takes a simple analytic form and is therefore known precisely. The correlation energy has multiple different approximations but can be obtained numerically up to three significant figures for select electron densities and later adapted for all densities.[13,14] As mentioned before, given the nature of the LDA and uniform electron gas, the method has success defining slowly varying electronic densities, like bulk metals. Additionally, LDA has played an integral role in predicting various materials properties such as vibrational frequencies, elastic moduli, etc., as well as lay the groundwork for the construction of more sophisticated approximations to the exchange-correlation energy. Still, significant issues arise when modelling other properties such as the binding energy, band energies, work function, and lacks predictive power for defining energy barriers in chemical reactions. As such, the approximation does not boast much popularity in quantum chemistry or materials science applications. More specifically, there is a tendency to lose accuracy predicting properties of systems in which electron-electron interactions dominate. Aside from its shortcomings, the local-density approximation produces decent estimates for E_{xc} in certain systems because of its inherent error cancellation between the exchange and correlation energies by underestimating E_c but overestimating E_x . Thankfully, far brighter minds than my own worked tirelessly to produce more accurate representations of the exchange-correlation functionals. The next natural progression of the LDA class led to the development of the generalized gradient approximations (GGA).

2.7.2 Generalized Gradient Approximation (GGA)

The aforementioned structure of the LDA formalism depends on the well behaved uniform electron density. In practice, however, the electron density in real systems tends to be spatially inhomogeneous. Therefore, concentrating efforts in the development of formulae that consider the inhomogeneity of the electron density, or more specifically, the gradient of the electron density at varying points in space within model systems. GGA made significant strides in rectifying binding energy and other systematic errors like the overestimation of molecular atomization energies and bond lengths. With its improvements over its predecessor, the generalized gradients approximations of the exchange-correlation functional were quickly adapted by the field of theoretical quantum chemistry beginning in the early 1990s. Some of the most successful within the suite of GGA functionals are Perdew-Burke-Ernzerhof (PBE) and Perdew-Wang (PW91) in physics and Becke-Lee-Yang-Parr (BLYP).[14,15,16] Currently available GGA functionals produce far more accurate results for defining and differentiating chemical bonding – covalent, ionic, metallic, etc. However, there is a general failure to accurately define and account for Van der Waals interactions.[17] Therefore, in the interest of constantly improving theoretical models, suited to build a complete picture of materials properties under the influence of the drive for a comprehensive understanding, as well as societal pressures to create enhanced technologies, more sophisticated formulations have been developed to better model weaker electrostatic interactions.

2.7.3 Meta-GGA functionals

Next in the emergence of a more sensitive class of exchange functionals which account for a variety of electrostatic interactions come the meta-GGAs. The development of meta-GGA relies on the utilization of the Laplacian (second derivative) of the density as well as the magnitude and gradient of the electron density. Importantly, the local kinetic energy of electrons is also considered which aids in the more accurate treatment of weaker electrostatic interactions; usually this is defined as the Kohn-Sham kinetic-energy density. Meta-GGA functionals are improved in several cases over GGA counterparts as they typically report higher accuracies in atomization energies, metal surface energies, and transition pressure.[18] Moreover, they also support accurate van der Waals interactions required for consideration of material aspects such as adsorption on surfaces.[19]

2.7.4 Hybrid Exchange Functionals

Beyond the local or semi-local methods discussed previously (LDA, GGA, meta-GGA), there is a group of functionals which utilizes a mixture of Hartree-Fock and Kohn-Sham theories. The hybrid functionals tend to be far more accurate for non-metallic systems, particularly in their treatment and calculations of band structures. To address this known disparity between known and calculated band structures (band gaps), recent developments in exchange-correlation functional introduce a non-locality in DFT by incorporating a fraction of Fock exchange with exchange-correlation energy within the GGA. In other words, the exchange-correlation functional becomes a linear combination of HF and semi-local exchange terms. Hybrid functionals exist on a range of screening depending on specific application. For example, in periodic solids, HSE (Heyd-Scuseria-

Ernzehof), based on the PBE exchange-correlation (Exc), is usually preferred as the short-range screening leads to faster convergence respective of number of k-points and size of the unit cell.[21] Afterall, the main limitation of this high-level functional is indeed the computational cost. Two other notable hybrid functionals include PBE0, and in quantum chemistry, B3LYP which introduces updated mixing and other empirical parameters into its predecessor BLYP.[20,21,22] Generally speaking, hybrid functionals result in a substantial improvement in obtaining a variety of more complex or nuanced material properties, such as bond lengths, van der Waals interactions, atomization energies, and band structure in nonmetallic solids. However, in the quest for exact chemical accuracy and the growing desire for accurate computational models of forefront materials, we soon may rely on help from additional computational methods. For example, applying data-driven machine learning systems to current DFT methods may prove vital in progressing the field of theoretical materials science and quantum chemistry. In fact, one such approach has predicted a variety of material properties such as bond lengths, electronic structures, crystal structures, etc.[23] Another possibility for the employment of hybrid DFT-machine learning methods could lie with the predictive power of materials not yet envisaged. Imagine the benefits to humankind and the planet of one such method with the ability to forecast particular novel assemblies of materials with desirable properties, e.g. improved photovoltaic efficiency.

The success of DFT as well as improvements in computational resources, has led to a vast and rapidly growing database of hundreds of thousands of materials. With such large, open-source datasets, machine-learning approaches are gaining traction, especially in the application to predictive models which can both propose novel materials as well as

focus research efforts on *viable* materials with desired properties like band gap, formation energy, melting point, magnetic anisotropy, catalytic activity, adsorption energy, etc. Having the ability to parameterize material predictions would prove greatly beneficial to our species as we march forward on our evolutionary path colored by a unique set of modern challenges – energy consumption, food production, water production and allocation, etc.

2.8 Periodic Boundary Conditions

As we have seen from Hohenberg-Kohn-Sham density functional theory, we have reduced the dependence of the system by mapping the many-body wavefunction onto a single electron (one-electron theory) by taking a product of one-electron states like so:

$$\psi(\vec{r}_1, \dots, \vec{r}_N) \rightarrow [\psi_1(\vec{r}), \psi_2(\vec{r}), \dots, \psi_N(\vec{r})]. \quad 2.32$$

This is a clear improvement over the dependence on every aspect of all electronic wavefunctions in the complex many-body Schrodinger equation, or a function to the power of N . However, this improvement to a dependence on the number of one electron states, N , only works well for small systems of a few atoms or small molecules. As we approach bulk systems the number of electrons quickly approaches N^{23} again making solutions quite expensive computationally. So, we must again make clever approximations or set favorable boundary conditions in order to achieve accurate solutions to the Kohn-Sham equations. The Vienna ab initio Simulation Package (VASP) makes use of periodic boundary conditions in order to simplify and reduce computational expense while retaining accuracy in the calculation of bulk or periodic system properties once again.

Bloch's theorem states that solutions to the Schrodinger equation in a periodic potential take the form of a plane wave modulated by a periodic function" [24]. By treating our system like a perfect crystal and applying periodic boundary conditions, the system's nuclei resemble this periodic potential. As such, electrons within our solid abide by a set of symmetry rules which means that the wavefunction is an eigenstate of all translation operators simultaneously. Therefore each of these electronic wavefunctions is a Bloch state, shown by the Bloch function below,

$$\begin{aligned}\psi_{n\mathbf{k}}(\mathbf{r}) &= u_{n\mathbf{k}}(\mathbf{r})e^{i\mathbf{k}\mathbf{r}}, \\ u_{n\mathbf{k}}(\mathbf{r} + \mathbf{R}) &= u_{n\mathbf{k}}(\mathbf{r}).\end{aligned}\tag{2.33}$$

where $u_{n\mathbf{k}}(\mathbf{r})$ is a periodic function with the same periodicity as the crystal, n is the band index, on the order of the number of electrons per unit cell, \mathbf{k} is the Bloch wave vector usually constrained to lie within the first Brillouin zone of the reciprocal space, and \mathbf{r} is a lattice vector of the Brillouin space lattice. Due to the periodicity of the system, the wavefunction remains invariant under spatial translations, $\mathbf{r} + \mathbf{R}$ like so:

$$\psi_{n\mathbf{k}}(\mathbf{r} + \mathbf{R}) = \psi_{n\mathbf{k}}(\mathbf{r})e^{i\mathbf{k}\mathbf{R}},\tag{2.34}$$

Thus, solutions to the Kohn-Sham equations are labeled by the previous methods where one index runs over the number of electrons contained within the unit cell, while the second index, runs over all possible Bloch vectors contained within the first unit cell. We then, transform the electron density expression to abide by the same periodic boundary conditions to obtain the following,

$$\rho(\mathbf{r}) = \frac{1}{\Omega_{\text{BZ}}} \sum_n \int_{\text{BZ}} f_{n\mathbf{k}} |\psi_{n\mathbf{k}}(\mathbf{r})|^2 d\mathbf{k} \quad 2.35$$

$$\rho(\mathbf{r}) = \sum_{n\mathbf{k}} w_{\mathbf{k}} f_{n\mathbf{k}} |\psi_{n\mathbf{k}}(\mathbf{r})|^2 d\mathbf{k}$$

We can see from Equation 2.35 that the density involves an integration over the first Brillouin zone. This is potentially problematic since the number of Bloch vectors, \mathbf{k} , is quite large. We can, however, take advantage of the fact that Bloch vectors which are close together are nearly identical and approximate the integral by a weighted sum over a discrete set of \mathbf{k} -points within the first Brillouin zone.[7,24]

$$\rho(\mathbf{r}) = \sum_{n\mathbf{k}} w_{\mathbf{k}} f_{n\mathbf{k}} |\psi_{n\mathbf{k}}(\mathbf{r})|^2 d\mathbf{k} \quad 2.36$$

This produces a density with dependence upon discrete quantities and greatly reduces the computational load leading to accurate and timely results, depending on the computing system.

2.9 The Reciprocal Space Lattice, Plane Wave Basis, and Monkhorst Pack \mathbf{k} -Point Sampling

Recall, from Bloch's theorem mentioned in Section 2.7, the index, \mathbf{k} , is a vector and considered a quantum number which characterizes wave functions in a periodic crystal.[24] An additional point of distinction for wave vector \mathbf{k} is in its definition as the crystal momentum. This distinction has led to \mathbf{k} -space also referred to as reciprocal space or momentum space. Now, for each given set of real space lattice points, $\mathbf{R} = n_1 \mathbf{a}_1 + n_2 \mathbf{a}_2 + n_3 \mathbf{a}_3$, there exist corresponding reciprocal lattice space vectors to define the reciprocal space lattice given in general by Equation 2.37,

$$\mathbf{a}_i \cdot \mathbf{b}_j = 2\pi \delta_{ij} \quad 2.37$$

For the practical three-dimensional space, these reciprocal lattice vectors take the following form,

$$\mathbf{b}_1 = \frac{2\pi}{\Omega} \mathbf{a}_2 \times \mathbf{a}_3 \quad \mathbf{b}_2 = \frac{2\pi}{\Omega} \mathbf{a}_3 \times \mathbf{a}_1 \quad \mathbf{b}_3 = \frac{2\pi}{\Omega} \mathbf{a}_1 \times \mathbf{a}_2, \quad 2.38$$

$$\Omega = \mathbf{a}_1 \cdot \mathbf{a}_2 \times \mathbf{a}_3$$

Where, the denominator is equivalent to the volume of the real space unit cell or, the Wigner-Seitz cell.[24] In the same fashion the real space Bravais lattice is divided up into the Wigner-Seitz cell by a set of perpendicular bisectors of nearest neighbors, the reciprocal space lattice can be divided into Brillouin zones. Refer to Figure 2.2 for a general visual representation of the real space lattice, the conversion of real to reciprocal space, and the generation of the first Brillouin zone for a face-centered cubic (fcc) real space lattice.

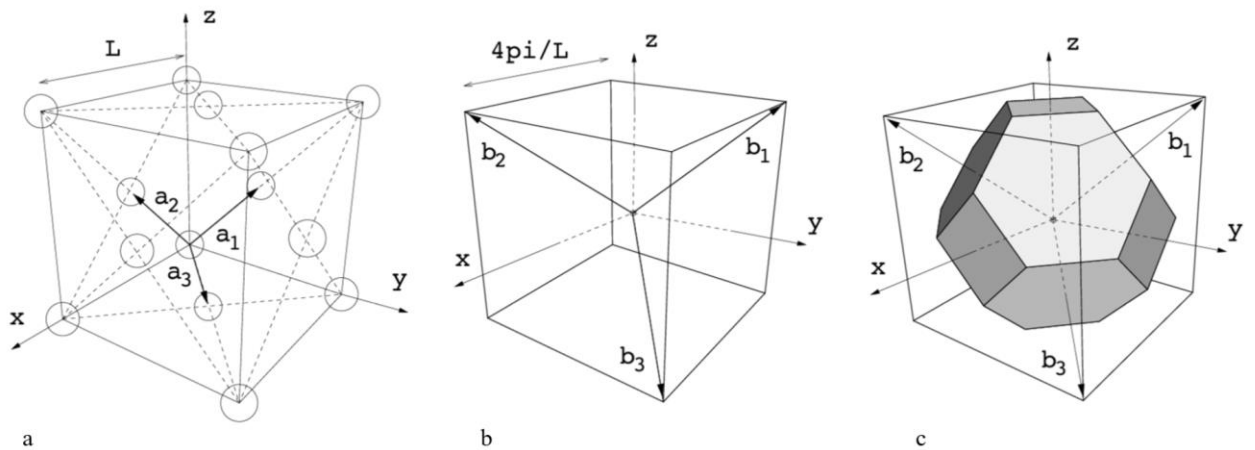


Figure 2.2. Representation of the transformation from real space (a) to reciprocal space (b) and the construction of the first Brillouin Zone for a face-centered cubic (fcc) real space lattice, from VASP lecture, Martijn Marsman, University of Vienna, open source.[7,24]

According to Bloch's theorem, electronic wavefunctions at each \mathbf{k} -point can be expanded in terms of a discrete plane-wave basis set. Recall the periodic condition of translational invariance imposed upon the periodic wavefunction given in Equation 2.33,

$$\begin{aligned}\psi_{n\mathbf{k}}(\mathbf{r}) &= u_{n\mathbf{k}}(\mathbf{r})e^{i\mathbf{k}\mathbf{r}}, \\ u_{n\mathbf{k}}(\mathbf{r} + \mathbf{R}) &= u_{n\mathbf{k}}(\mathbf{r}).\end{aligned}$$

All the periodic functions may be written as a sum of plane waves as follows:

$$\begin{aligned}\psi_{n\mathbf{k}}(\mathbf{r}) &= \frac{1}{\Omega^{1/2}} \sum_{\mathbf{G}} C_{\mathbf{G}n\mathbf{k}} e^{i(\mathbf{G}+\mathbf{k})\mathbf{r}}, \\ u_{n\mathbf{k}}(\mathbf{r}) &= \frac{1}{\Omega^{1/2}} \sum_{\mathbf{G}} C_{\mathbf{G}n\mathbf{k}} e^{i\mathbf{G}\mathbf{r}}.\end{aligned}\tag{2.39}$$

These periodic functions written in terms of plane waves can be written in terms of a grid in the \mathbf{k} -space shown in Figure 2.2 a). Though there are technically still an infinite number of plane waves, the higher order Fourier components (large $|\mathbf{k} + \mathbf{G}|$) are generally considered negligible and we can truncate the expansion at a value which is larger than the kinetic energy value of all plane waves within a certain volume, known as the cutoff energy (ENCUT) shown in Figure 2.3 b).

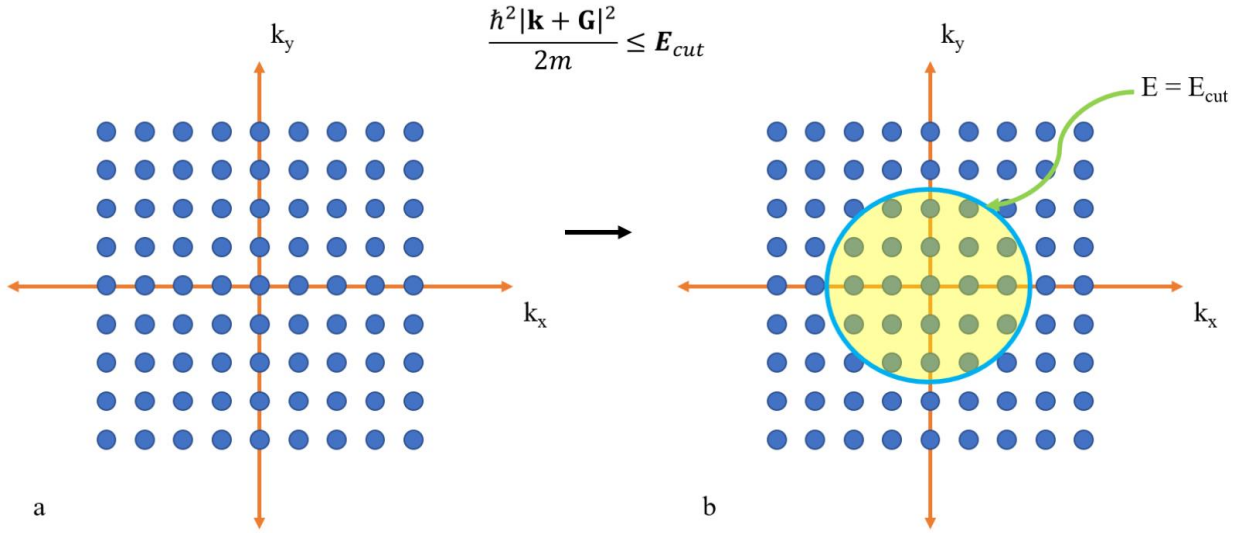


Figure 2.3. Visualization of the truncation of the plane wave basis in reciprocal space via the cutoff energy such that the cutoff energy is less than or equal to kinetic energy of the

Now, the application of Bloch's theorem is a wonderful computational simplification given that the total energy of the sample crystal can be computed simply by the knowledge of the periodic function of the lattice, $u_{\mathbf{k}}(\mathbf{r})$, given in Equation 2.33. However, the theorem also requires calculating wavefunctions for all boundary conditions (translational invariance under periodic boundary conditions). Therefore, for a finite crystal, the number of terms to be summed becomes equivalent to the number of unit cells in the system.[24,25] As a result, \mathbf{k} -space sampling becomes quite fine and we lose any computational advantage we once had. Therefore, we must take advantage of another approximation made by Monkhorst and Pack.[25] Their work utilizes the weak dependence of the lattice periodic part of the wave function, $u_{\mathbf{k}}(\mathbf{r})$, on wave vector \mathbf{k} . Given the weak dependence, a small, finite number of \mathbf{k} -points is sufficient to reach accurate energy minimization. However, it is important for certain systems, like phosphorene and other two-dimensional materials, to run multiple calculations, successively increasing the

number of k-points in order to ensure the most accurate ground state energy. Additionally, it can be quite useful to ensure that a gamma-shifted set of k-points is utilized in order to include the Γ -point, especially if it is physically significant, i.e., there are band maxima located at the Γ -point for a semiconductor (like phosphorene).

Choice of basis set is vital for accurate and timely results. For solid state materials and the use of the periodic software VASP, choosing a basis set whose phase shares the same periodicity of the system matters a great deal. Along these lines, for the systems explored utilizing VASP in the remainder of this dissertation, a plane wave basis set was utilized in the energy minimization of doped phosphorene and ligated phosphorene as well as preliminary results on doped MoS₂ with magnetic superatoms.

2.10 Non-Periodic, Cluster Model DFT Calculations

Molecular orbitals, in general, can be expressed as linear combinations of n basis functions, known as the **LCAO-MO** method, as follows:

$$\psi_i = \sum_{\mu} c_{\mu i} \phi_{\mu} \quad 2.40$$

Each orbital or one electron function, ψ_i , is a linear combination of basis functions ϕ_{μ} where the coefficients are defined as **molecular orbital expansion coefficients**, $c_{\mu i}$. [26]

There are a variety of options for non-periodic localized basis functions one can choose from based on the specifics of calculations. Two widely applicable methods for expansion of basis functions are **Slater type orbitals (STOs)** and **Gaussian type orbitals (GTOs)**.

Slater type orbitals contain a radial and spherical portion describing the radial extent of a particular orbital and description of the shape of a particular orbital;

$$\varphi_{nlm}(r, \theta, \varphi) = N_{nlm\zeta} Y_{lm}(\theta, \varphi) r^{n-1} e^{-\zeta r} \quad 2.41$$

where, the normalization constant N is chosen such that integration over the square of the basis function yields unity. The radial portion obviously depends on the distance, r , from the origin of the basis function exposing the cusp condition for a point nucleus of charge Z :

$$\left(\frac{dR}{dr} \right)_{r=0} = -Z \quad 2.42$$

The spherical harmonics depend upon angular and magnetic quantum numbers l and m respectively.

Gaussian type orbitals are similarly constructed of a radial and spherical part however, the spherical contribution is expressed in cartesian coordinates like so,

$$\chi_{abc}(r, \theta, \varphi) = N_{abc\alpha} x^a y^b z^c e^{-\alpha r^2} \quad 2.43$$

By which the angular momentum vector L can be expressed as the sum of integer exponents,

$L = a + b + c$. The normalization constant abides by similar restrictions for unity as STOs.

The major differences between the two functions occur at the bounds $r = 0$, $r \rightarrow \infty$. At $r = 0$ we have seen the cusp condition results in a function with finite slope in the Slater type orbitals while the Gaussian function has a zero-slope resulting in an incorrect behavior at the nucleus. For large values, $r \rightarrow \infty$, the radial portion of the GTO, $e^{-\alpha r^2}$, decays far more rapidly than its Slater type radial counterpart, $e^{-\zeta r}$. [26] STOs more accurately describe quantitative features of the molecular orbital than GTOs and, fewer STOs are needed in a basis function expansion of the orbital for comparable results.

GTOs show their prowess in the calculation of multicenter, multi-electron operators such as structured in the Fock matrix operator shown below:

$$\mathbf{F}\psi_i = \mathbf{h}\psi_i + (\mathbf{J} - \mathbf{K})\psi_i \quad 2.44$$

Where,

$$\mathbf{h} = -\frac{1}{2}\nabla_1^2 + \sum \frac{Z_A}{r_{1A}}$$

$$\mathbf{J}\psi_i = \left[\int \frac{\psi_i^*(r_2)\psi_i(r_2)}{r_{12}} dr_2 \right] \psi_i \quad 2.45$$

$$\mathbf{K}\psi_i = \left[\int \frac{\psi_j^*(r_2)\psi_i(r_2)}{r_{12}} dr_2 \right] \psi_i$$

Which have the advantage of integrating with respect to the same center.

2.11 Computational Details

Theoretical studies carried out on the **periodic phosphorene systems** are based on a dispersion corrected density functional theory (DFT) within generalized gradient approximation (GGA) using the gradient corrected functional proposed by Perdew, Burke and Ernzerhof (GGA PBE) for the exchange correlation functional.[40] The Vienna Ab-initio Simulation Package (VASP) was utilized for all periodic computations, individual ribbon and doped phosphorene, with a plane wave basis set and cutoff energy set to 400 eV.[41, 42, 43] While the GGA functionals are known to be quite accurate for ground state geometric optimizations, they are known to underestimate bandgaps; as such, for the work on doped phosphorene sheets, calculations of the electronic structure were carried out

using the HSE06 hybrid functional.[44] Upon examination of the results of bandgap as a function of ribbon type and width as well as hydrogen edge termination, obtained bandgap values were consistent with those previously presented in other works [45]. Projected density of states was plotted using sumo.[46] Thus, results presented on the energetics and bandgap as a function of width were obtained using GGA-PBE while results which investigated the more nuanced effects on the electronic structure by charge transfer doping of phosphorene monolayers used the hybrid functional (HSE06).

The calculations on the periodic sheets were performed in a large supercell with a 100-atom phosphorene sheet with a supercell of size 16.55 x 21.55 x 21.00 Å. The large size of the supercell ensured no interaction above and below the plane of the two-dimensional phosphorene sheets. The size of the supercell varied for calculations of individual phosphorene nanoribbons based on width and type (ZPNR or APNR). For ribbon calculations, the size of the supercell was adjusted in relation to the change in width of the various ribbons. For ribbon calculations with varying termination, the same size of the supercell was utilized (9.93 x 47.80 x 21.00 Å) constructed in relation to the change in width for N = 9 zigzag PNR. We tailored the supercell to include sufficient vacuum space above and to either side of the ribbon edges. As the VASP package treats all systems as periodic, this ensured no interaction above and below the plane of the phosphorus ribbon as well as to either side of the ribbon. Thus, each ribbon can be considered individually and absent of electronic effects of neighboring ribbons.

Bader charge analysis was initiated by including the INCAR tags, LCHARG = .TRUE. and LAECHG = .TRUE. and computed after convergence by first compiling the following two output files, AECCAR0 and AECCAR2, which describe the core charge and

valence charge respectively, to write the CHGCAR_sum file. Afterwards the bader script completes the bader analysis on the CHGCAR by the following command line: bader CHGCAR ref-CHGCAR_sum.

Work function calculations were also performed on ZPNRs. In this case, a dipole correction was incorporated along the z-axis of the ribbons. This dipole correction improves the convergence and allows for the calculation of the electrostatic potential in the vacuum which was used in the calculation of the work function of the system. Electron affinity calculations also make use of these settings as they are calculated by subtracting conduction band energy from the vacuum energy of the system.

Regarding the **non-periodic density functional theory** (DFT) based results reported in this dissertation, i.e., the phosphorene flakes, calculations are executed using the Amsterdam Density Functional (ADF) software.[29] The gradient-corrected Perdew, Burke, and Ernzerhof (PBE) functional was utilized for all reported results.[15] The Slater type triple ζ basis set with two polarization functions (TZ2P) core was chosen for all elements.[31,48] The frozen core orbitals of the elements are expressed as an auxiliary set of Slater-type basis functions. The relativistic effect of the heavy elements is accounted for by using the zero-order regular approximation (ZORA).[49,50] The dispersion correction is included by Grimme's DFT-D3 correction with the Becke-Johnson damping.[51] The hessian-based quasi-Newton method without symmetry constraints is used for all the geometry optimizations.[52] During all optimizations and single point energy evaluation, the energy convergence threshold is set to 1×10^{-7} Hartree, whereas the default convergence criteria are chosen for the geometric optimizations.[15,51] The spin contamination values are also checked for the spin-polarized systems, ensuring no significant deviation is

present. To determine the global minima of each structure, a wide range of spin multiplicities were examined, and only the lowest energy structures were chosen for all cases.

References

1. *Program: The 1st International Conference on Innovations for Computing, Engineering and Materials*, 2021 ICEM 2021. 2021, p. 010005. DOI.org (Crossref), <https://doi.org/10.1063/12.0007059>.
2. Pan, Jinbo, et al. “Auxetic Two-Dimensional Transition Metal Selenides and Halides.” *Npj Computational Materials*, vol. 6, no. 1, Oct. 2020, p. 154. DOI.org (Crossref), <https://doi.org/10.1038/s41524-020-00424-1>.
3. Attanayake, Nuwan H., et al. “Electrocatalytic CO₂ Reduction on Earth Abundant 2D Mo₂C and Ti₃C₂MXenes.” *Chemical Communications*, vol. 57, no. 13, 2021, pp. 1675–78. DOI.org (Crossref), <https://doi.org/10.1039/D0CC05822J.N>.
4. Hartree, D. R. “The Wave Mechanics of an Atom with a Non-Coulomb Central Field. Part I. Theory and Methods.” *Mathematical Proceedings of the Cambridge Philosophical Society*, vol. 24, no. 1, Jan. 1928, pp. 89–110. DOI.org (Crossref), <https://doi.org/10.1017/S0305004100011919>.
5. R. G. Parr and W. Yang, *Density-functional theory of atoms and molecules*, Oxford Univ. Press [u.a.], New York, NY, 1. iss. as ... paperback., 1994.
6. W. Koch and M. C. Holthausen, *A chemist’s guide to density functional theory*, Wiley-VCH, Weinheim, 2nd ed., 5. reprint., 2008.
7. *The VASP Manual - Vaspwiki*. https://www.vasp.at/wiki/index.php/The_VASP_Manual. Accessed 25 Apr. 2023.
8. Kohn, W. “Nobel Lecture: Electronic Structure of Matter—Wave Functions and Density Functionals.” *Reviews of Modern Physics*, vol. 71, no. 5, Oct. 1999, pp. 1253–66. DOI.org (Crossref), <https://doi.org/10.1103/RevModPhys.71.1253>.
9. Hohenberg, P., and W. Kohn. “Inhomogeneous Electron Gas.” *Physical Review*, vol. 136, no. 3B, Nov. 1964, pp. B864–71. DOI.org (Crossref), <https://doi.org/10.1103/PhysRev.136.B864>.
10. Kohn, W., and L. J. Sham. “Self-Consistent Equations Including Exchange and Correlation Effects.” *Physical Review*, vol. 140, no. 4A, Nov. 1965, pp. A1133–38. DOI.org (Crossref), <https://doi.org/10.1103/PhysRev.140.A1133>.
11. Sholl, David S., and Janice A. Steckel. *Density Functional Theory: A Practical Introduction*. Wiley, 2009
12. Perdew, John P. “Jacob’s Ladder of Density Functional Approximations for the Exchange-Correlation Energy.” *AIP Conference Proceedings*, vol. 577, AIP, 2001, pp. 1–20. DOI.org (Crossref), <https://doi.org/10.1063/1.1390175>.
13. Ceperley, D. M., and B. J. Alder. “Ground State of the Electron Gas by a Stochastic Method.” *Physical Review Letters*, vol. 45, no. 7, Aug. 1980, pp. 566–69. DOI.org (Crossref), <https://doi.org/10.1103/PhysRevLett.45.566>.
14. Perdew, John P., and Yue Wang. “Accurate and Simple Analytic Representation of the Electron-Gas Correlation Energy.” *Physical Review B*, vol. 45, no. 23, June 1992, pp. 13244–49. DOI.org (Crossref), <https://doi.org/10.1103/PhysRevB.45.13244>.
15. Perdew, John P., et al. “Generalized Gradient Approximation Made Simple.” *Physical Review Letters*, vol. 77, no. 18, Oct. 1996, pp. 3865–68. DOI.org (Crossref), <https://doi.org/10.1103/PhysRevLett.77.3865>.

16. Becke, A. D. “Density-Functional Exchange-Energy Approximation with Correct Asymptotic Behavior.” *Physical Review A*, vol. 38, no. 6, Sept. 1988, pp. 3098–100. DOI.org (Crossref), <https://doi.org/10.1103/PhysRevA.38.3098>.
17. Sham, L. J., and M. Schlüter. “Density-Functional Theory of the Energy Gap.” *Physical Review Letters*, vol. 51, no. 20, Nov. 1983, pp. 1888–91. DOI.org (Crossref), <https://doi.org/10.1103/PhysRevLett.51.1888>.
18. Sun, Jianwei, et al. “Strongly Constrained and Appropriately Normed Semilocal Density Functional.” *Physical Review Letters*, vol. 115, no. 3, July 2015, p. 036402. DOI.org (Crossref), <https://doi.org/10.1103/PhysRevLett.115.036402>.
19. Adhikari, Santosh, et al. “Molecule-Surface Interaction from van Der Waals-Corrected Semilocal Density Functionals: The Example of Thiophene on Transition-Metal Surfaces.” *Physical Review Materials*, vol. 4, no. 2, Feb. 2020, p. 025005. DOI.org (Crossref), <https://doi.org/10.1103/PhysRevMaterials.4.025005>.
20. Adamo, Carlo, and Vincenzo Barone. “Toward Reliable Density Functional Methods without Adjustable Parameters: The PBE0 Model.” *The Journal of Chemical Physics*, vol. 110, no. 13, Apr. 1999, pp. 6158–70. DOI.org (Crossref), <https://doi.org/10.1063/1.478522>.
21. Heyd, Jochen, et al. “Hybrid Functionals Based on a Screened Coulomb Potential.” *The Journal of Chemical Physics*, vol. 118, no. 18, May 2003, pp. 8207–15. DOI.org (Crossref), <https://doi.org/10.1063/1.1564060>.
22. Becke, Axel D. “Density-functional Thermochemistry. III. The Role of Exact Exchange.” *The Journal of Chemical Physics*, vol. 98, no. 7, Apr. 1993, pp. 5648–52. DOI.org (Crossref), <https://doi.org/10.1063/1.464913>.
23. Banjade, Huta R., et al. “Structure Motif–Centric Learning Framework for Inorganic Crystalline Systems.” *Science Advances*, vol. 7, no. 17, Apr. 2021, p. eabf1754. DOI.org (Crossref), <https://doi.org/10.1126/sciadv.abf1754>.
24. Ashcroft, Neil W., and N. David Mermin. *Solid State Physics*. 12. Indian repr, Cengage Learning, 2011.
25. Kratzer, Peter, and Jörg Neugebauer. “The Basics of Electronic Structure Theory for Periodic Systems.” *Frontiers in Chemistry*, vol. 7, Mar. 2019, p. 106. DOI.org (Crossref), <https://doi.org/10.3389/fchem.2019.00106>.
26. Majumdar, D., Samanta, P.N., Roszak, S., Leszczynski, J. (2021). Slater-Type Orbitals. In: Perl, E. (eds) *Basis Sets in Computational Chemistry*. Lecture Notes in Chemistry, vol 107. Springer, Cham. https://doi.org/10.1007/978-3-030-67262-1_2
27. Tsuneda, Takao, and Kimihiko Hirao. “Self-Interaction Corrections in Density Functional Theory.” *The Journal of Chemical Physics*, vol. 140, no. 18, May 2014, p. 18A513. DOI.org (Crossref), <https://doi.org/10.1063/1.4866996>.
28. Solomon, Edward I., et al., editors. *Computational Inorganic and Bioinorganic Chemistry*. Wiley, 2009.
29. Te Velde, G., et al. “Chemistry with ADF.” *Journal of Computational Chemistry*, vol. 22, no. 9, July 2001, pp. 931–67. DOI.org (Crossref), <https://doi.org/10.1002/jcc.1056>.
30. J. P. Perdew, K. Burke and M. Ernzerhof, *Phys. Rev. Lett.*, 1996, **77**, 3865–3868.
31. Van Lenthe, E., and E. J. Baerends. “Optimized Slater-Type Basis Sets for the Elements 1-118.” *Journal of Computational Chemistry*, vol. 24, no. 9, July 2003, pp. 1142–56. DOI.org (Crossref), <https://doi.org/10.1002/jcc.10255>.

32. Chong, D. P., et al. "Interpretation of the Kohn–Sham Orbital Energies as Approximate Vertical Ionization Potentials." *The Journal of Chemical Physics*, vol. 116, no. 5, Feb. 2002, pp. 1760–72. DOI.org (Crossref), <https://doi.org/10.1063/1.1430255>.
33. Fan, Liangyou, and Tom Ziegler. "Optimization of Molecular Structures by Self-consistent and Nonlocal Density-functional Theory." *The Journal of Chemical Physics*, vol. 95, no. 10, Nov. 1991, pp. 7401–08. DOI.org (Crossref), <https://doi.org/10.1063/1.461366>.
34. Van Lenthe, E., et al. "The Zero-order Regular Approximation for Relativistic Effects: The Effect of Spin–Orbit Coupling in Closed Shell Molecules." *The Journal of Chemical Physics*, vol. 105, no. 15, Oct. 1996, pp. 6505–16. DOI.org (Crossref), <https://doi.org/10.1063/1.472460>.
35. Blöchl, P. E. "Projector Augmented-Wave Method." *Physical Review B*, vol. 50, no. 24, Dec. 1994, pp. 17953–79. DOI.org (Crossref), <https://doi.org/10.1103/PhysRevB.50.17953>.
36. Kresse, G., and D. Joubert. "From Ultrasoft Pseudopotentials to the Projector Augmented-Wave Method." *Physical Review B*, vol. 59, no. 3, Jan. 1999, pp. 1758–75. DOI.org (Crossref), <https://doi.org/10.1103/PhysRevB.59.1758>.
37. Kresse, G. "Ab Initio Molecular Dynamics for Liquid Metals." *Journal of Non-Crystalline Solids*, vol. 192–193, Dec. 1995, pp. 222–29. DOI.org (Crossref), [https://doi.org/10.1016/0022-3093\(95\)00355-X](https://doi.org/10.1016/0022-3093(95)00355-X).
38. Grimme, Stefan, et al. "Effect of the Damping Function in Dispersion Corrected Density Functional Theory." *Journal of Computational Chemistry*, vol. 32, no. 7, May 2011, pp. 1456–65. DOI.org (Crossref), <https://doi.org/10.1002/jcc.21759>.
39. Krukau, A. V., Vydrov, O. A., Izmaylov, A. F. & Scuseria, G. E. Influence of the exchange screening parameter on the performance of screened hybrid functionals. *J. Chem. Phys.* 125, 224106 (2006).
40. J.P. Perdew, K. Burke, M. Ernzerhof, Generalized Gradient Approximation Made Simple, *Phys.Rev.Lett.* 77(1996)3865–3868. <https://doi.org/10.1103/PhysRevLett.77.3865>.
41. G. Kresse, J. Hafner, Ab initio molecular-dynamics simulation of the liquid-metal-amorphous-semiconductor transition in germanium, *Phys. Rev. B.* 49 (1994) 14251–14269. <https://doi.org/10.1103/PhysRevB.49.14251>.
42. G. Kresse, J. Furthmüller, Efficient iterative schemes for ab initio total-energy calculations using a plane-wave basis set, *Phys. Rev. B.* 54 (1996) 11169–11186. <https://doi.org/10.1103/PhysRevB.54.11169>.
43. G. Kresse, D. Joubert, From ultrasoft pseudopotentials to the projector augmented-wave method, *Phys. Rev. B.* 59 (1999) 1758–1775. <https://doi.org/10.1103/PhysRevB.59.1758>.
44. J. Heyd, G.E. Scuseria, M. Ernzerhof, Hybrid functionals based on a screened Coulomb potential, *J. Chem. Phys.* 118 (2003) 8207–8215. <https://doi.org/10.1063/1.1564060>.
45. H. Guo, N. Lu, J. Dai, X. Wu, X.C. Zeng, Phosphorene Nanoribbons, Phosphorus Nanotubes, and van der Waals Multilayers, *J. Phys. Chem. C.* 118 (2014) 14051–14059. <https://doi.org/10.1021/jp505257g>.
46. A.M. Ganose, A.J. Jackson, D.O. Scanlon, sumo: Command-line tools for plotting and analysis of periodic *ab initio* calculations, *Journal of Open Source Software.* 3 (2018) 717. <https://doi.org/10.21105/joss.00717>.

47. F. Yan, C.-K. Liao, M.A. Mahmoud, S.B. Bach, Electron Doping of Semiconducting MoS₂ Nanosheets by Silver or Gold Nanoclusters, *Langmuir*. 38 (2022) 4378–4388. <https://doi.org/10.1021/acs.langmuir.2c00120>.
48. Chong, D. P.; Van Lenthe, E.; Van Gisbergen, S.; Baerends, E. J. Even-Tempered Slater-Type Orbitals Revisited: From Hydrogen to Krypton. *J. Comput. Chem.* 2004, 25 (8), 1030–1036.
49. Lenthe, E. van; Snijders, J. G.; Baerends, E. J. The Zero-order Regular Approximation for Relativistic Effects: The Effect of Spin–Orbit Coupling in Closed Shell Molecules. *J. Chem. Phys.* **1996**, 105 (15), 6505–6516. <https://doi.org/10.1063/1.472460>.
50. Van Lenthe, E.; Ehlers, A.; Baerends, E.-J. Geometry Optimizations in the Zero Order Regular Approximation for Relativistic Effects. *J. Chem. Phys.* **1999**, 110 (18), 8943–8953.
51. Grimme, Stefan, et al. “Effect of the Damping Function in Dispersion Corrected Density Functional Theory.” *Journal of Computational Chemistry*, vol. 32, no. 7, May 2011, pp. 1456–65. DOI.org (Crossref), <https://doi.org/10.1002/jcc.21759>.
52. Fan, L.; Ziegler, T. Optimization of Molecular Structures by Self-Consistent and Nonlocal Density-Functional Theory. *J. Chem. Phys.* **1991**, 95 (10), 7401–7408.
53. Jacobsen, H.; Bérces, A.; Swerhone, D. P.; Ziegler, T. Analytic Second Derivatives of Molecular Energies: A Density Functional Implementation. *Comput. Phys. Commun.* **1997**, 100 (3), 263–276.

Chapter 3. Ligand and Width Effects: Fragmentation Pathways, Ribbon Stability, Band Gap, Work Function and Electron Affinity

3.1 Introduction

Throughout human history, the narrative of unquenchable fascination with our material surroundings has spun a thread of progress through the web of happenings over the course of our species' evolution. In tracing this thread, we see the connections that formed as a result of this exploration of the physical world form a theme of discovery. While not always with premeditated intent, like the fortuitous discovery of fire, humans are responsible for all the technological advancements we take for granted in the modern world. One such discovery which took millennia to develop, was the discernment of periodic trends within the matter that makes up our physical world. Marked by specific 'ages' in anthropology, e.g., stone age, copper age, bronze age, iron age, we can see the development of human interest in manipulating surroundings to our advantage but the noticing and subsequent exploration of patterns in abundance and types of materials were not well documented until the time of ancient Greeks. That burning question – what are the fundamental components of substances around us? – ultimately drove early philosophers and, later, scientists to concentrate efforts in pursuing a way to order elements around us. Dmitri Mendeleev is credited as the Father of the Periodic Table and the one who ultimately created a formalism by which we recognize characteristic patterns in the makeup of matter. Additional models of the atom and quantum mechanics gave us a

fundamental understanding of these patterns as well as the confidence to explore modifications in or harnessing documented properties.

As modern chemistry and materials science stand upon the shoulders of these giants, we perceive a new horizon on which the advent of new classes of materials is a reality. One such group showing considerable promise in the frontier of materials science is two-dimensional materials. The discovery of graphene in 2004 is commonly quoted as the birth of two-dimensional material research and at the time was all the rage. Since this date, the field has exploded, resulting in the discovery and experimental realization of a plethora of 2-D materials with a variety of different mechanical, optical, and electronic properties. Perhaps the biggest sources of demand for these materials is in battery technologies, photovoltaics, and chip manufacturing. Yet, despite demand for technological improvement and desire to meet this demand, challenges remain. Manufacturing at scale, precise control at the nanometer size regime, and incorporation of the materials into existing infrastructure prove major hurdles presently. The way forward is through the collective efforts of scientists and engineers to innovate solutions to the aforementioned trials. One integral piece to this complex puzzle is the shaping of fundamental knowledge through both theory and experiment in order to determine innate material properties. The understanding of a material's tendencies births the power to utilize the properties to our advantage and, importantly, imagine solutions to technological and infrastructural stymies.

One such modern material of intrigue is phosphorene. Many groups have contributed to the body of knowledge regarding the promising properties like high mobility, ambipolar conduction and tunable bandgap with layer number and ribbon

thickness. [20,23,24] Recently, our research group has contributed verification and new work to the known properties of phosphorene. The work on phosphorene is partially presented in this chapter, with a focus on the concepts of width-related bandgap control, effects of ligands on relative stability of ribbons, fragmentation pathways, an introduction to work function and scaling behavior with varying ribbon width, and, finally, bader charge analysis on binding between ligand and edge phosphorus atoms.

3.2 Discussion of Naming, Geometry, Relative Stability, and Potential Fragmentation Pathways:

It is helpful to have a general picture to provide some sort of clarity about what is happening structurally within a material. Especially at the small sizes which this research is focused, having a picture to construct a framework of operation can even be illuminating in finding explanations for observations that may seem counterintuitive when considering numbers alone. Thus, we will begin by outlining the parameters which define and differentiate armchair nanoribbons from zig-zag nanoribbons as well as the naming convention used in previous theoretical work on phosphorene nanoribbons (PNRs).[23] From our new understanding of what parameterizes a phosphorene nanoribbon, we can confidently begin the discussion on potential fragmentation pathways which utilizes energetics to demonstrate which “fragments” may be more likely to occur as the larger ribbons break apart. Furthermore, beyond the energetic arguments made, we will discuss the significant geometric reconstruction observed at small sizes that may also have a significant impact on strain-sensitive bandgap (revisited later in the discussion of band structure).

First, observe the distinction between zig-zag (ZPNR) or armchair (APNR) directions shown in Figure 3.1. The APNRs are defined by the propagation along the direction of the “armchair” generated by the bonding of each phosphorus atom with three nearest neighbors. As mentioned before, we can see clearly that the geometry is a result of the sp^3 – hybridized bonding leading to the “puckered honeycomb” seen in Figure 2.[14,23] Note, the edges of APNRs are formed by the edges of the armchairs themselves, constituted by roughly vertically oriented P-P dimers with bond angles of 102.1° between the next nearest neighbor P-atoms seen in Figure 3.1 a).[57] ZPNRs, in contrast, differ from their APNR counterparts as they propagate within the same plane but normal to the armchair axis. In other words, if we take a bird’s eye, or top-down, view looking down onto the ribbon, we would see propagation in the direction of “zig-zag” bonds within the ribbon. The general honeycomb geometry is still present but the edge geometry is quite different. Edges of ZPNRs are formed by single phosphorus atoms bonded to two nearest neighbors within the same plane forming 96.3° bond angles.

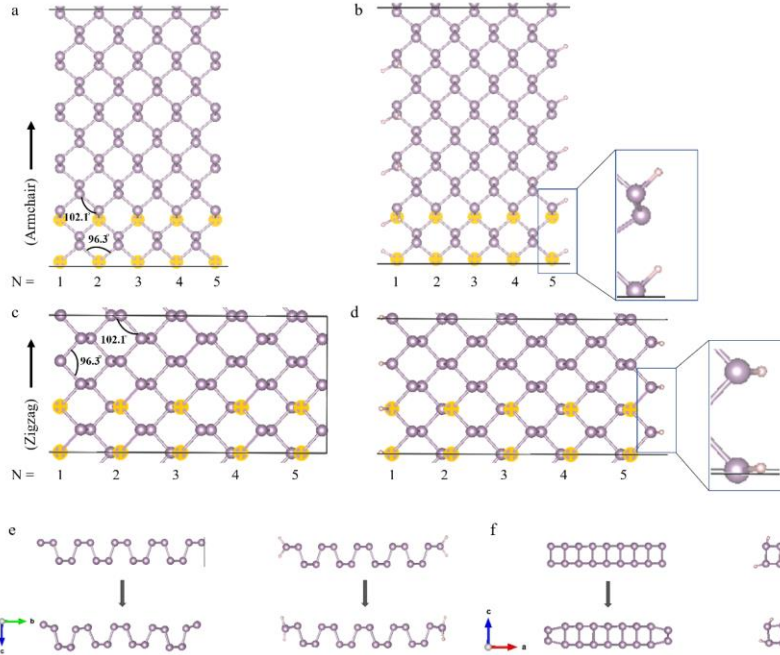


Figure 3.1. (a) Structure of non-terminated armchair phosphorene nanoribbon. (b) Hydrogen terminated armchair phosphorene nanoribbons. (c) Non-terminated and (d) hydrogen-terminated zig-zag ribbons. Note, also, highlighted atoms, labeled $N = 1-5$, identify the naming convention for the ribbon widths in both armchair (a)–(b) and zig-zag ribbons (c)–(d). (e) Comparison of optimized structures of non-terminated zigzag phosphorene nanoribbons (left) and hydrogen-terminated zigzag phosphorene nanoribbons (right). (f) Comparison of optimized structures of non-terminated armchair phosphorene nanoribbons (left) and hydrogen-terminated armchair phosphorene nanoribbons (right). Note the differences in edge reconstruction between non-terminated and hydrogen-terminated structures in both (e) and (f).

With this picture in mind, let us consider the naming convention used when generating these structures seen in Figure 3.1 (a-c). Similar to a previous study, by H. Guo et al., APNRs counted dimers constituting the “edges” of the armchairs, beginning with the outermost atoms, for a range of ribbon widths $N = 2-9$.^[23] Armchair edges were counted along the x-axis, thus generating the various widths, while ribbon lengths were extended along the y-axis of the unit cell to create APNRs. ZPNRs counted the “ridges,” constituted

by the upper plane of phosphorus atoms, beginning with the outermost atoms for a range of ribbon widths ($N = 2-9$). These ridges are counted along the y-axis of the unit cell to dictate the various widths, while ribbon length is propagated along the x-axis to create zig-zag nanoribbons. Both APNRs and ZPNRs were also terminated with hydrogen atoms on their respective edges for comparison of electronic properties, geometric reconstruction, and relative stabilities to their non-terminated counterparts. Figure 3.1 portrays the difference in ribbon geometry and shows the naming convention for each type of ribbon with various widths as well as a direct comparison of non-terminated and H-terminated APNRs and ZPNRs (a-d) for width $N = 5$. This specific choice of ribbon width was in the interest of providing concise but sufficient picture for the geometry of the structures. For a complete picture of both APNRs and ZPNRs all ribbon widths $N = 2-9$, refer to the supplemental information.

Now that that the distinction has been made between ribbon type and the naming convention outlined, let us revisit the results for edge reconstruction of non-terminated ribbons as well as the significant rearrangement of the atoms within non-terminated ribbons of small sizes ($N = 2,3$). The importance of these results is related to the understanding of relative stability of PNRs. Ideally, with unlimited computational power, one could carry out a variety of stability-related investigations including one of the most well-documented issues with several layer to monolayer phosphorene in ambient conditions – the adsorption of water at the surface leading to formation of phosphoric acid and dissolving of the material. Alas, computational capabilities are limited thus, the study focused on potential fragmentation pathways available to phosphorene during synthesis and obtained data that supports one specific pathway over others. These results also portray

the stabilization effects of edge-termination as the hydrogen edge-terminated species undergo far lower geometric reconstruction than do the nonterminated counterparts. The most extreme case is at the end-range size limits for non-terminated armchair PNRs. Figure 3.2 shows a direct comparison between the pre-optimized unit cell and optimized or ground state geometry (bottom) of non-terminated APNR (a) and terminated APNR (b) both of width $N = 5$. Note, the edge reconfiguration for non-terminated APNRs verified by H. Guo et al.[23]

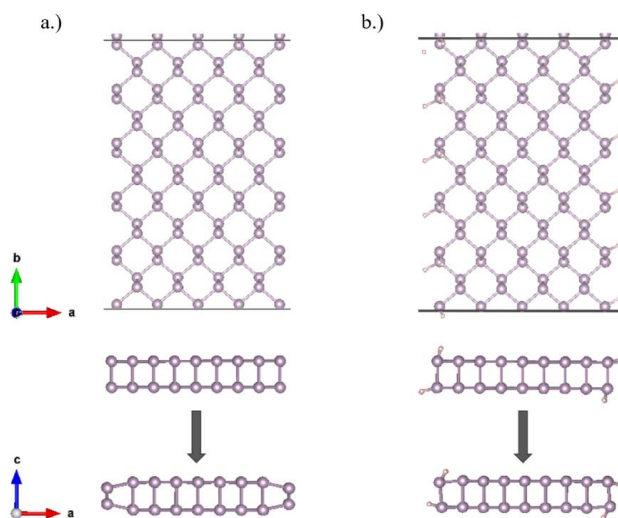


Figure 3.2. Visual comparison of geometry optimization for non-terminated (a.) and terminated (b.) APNRs of width $N = 5$.

We can see that the edges rearrange from their normal stacked dimer configuration characteristic of armchair geometry in the pre-optimized structure gives way to a flatter configuration with larger bond angles in the optimized geometry. In-plane angles increase from 96.3° to 111.1° while out of plane angles (affected by the stacked dimer edge reconfiguration) increase from 102.1° to 117.8° .

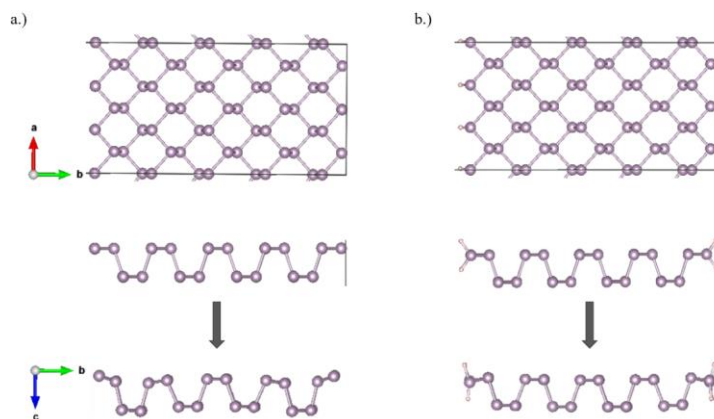


Figure 3.3. Visual comparison of geometry optimization for non-terminated (a.) and terminated (b.) ZPNRs of width $N = 5$.

Non-terminated zig-zag ribbons show much less reconfiguration in the ground state energy than their armchair counterparts. Though minor, there seems to be some slight deflection along the z -axis of the edge atoms out of plane of their nearest neighbors for ZPNRs as seen in Figure 3.3(a). In direct comparison to the terminated ZPNRs shown in Figure 3.3(b), non-terminated ribbons seem to take on more of a “curling” along the z -axis in addition to the deflection of the phosphorus atoms at the edges. Rearrangement effects are further exaggerated when approaching small sizes ($N = 2,3$) especially in the case of non-terminated APNRs which can be seen in the visualization of fragmentation given in Figure 3.4.

Figures 3.4-3.7 visually demonstrate the fragmentation of parent ribbon into component parts and, upon relaxation, the reconstruction that ensues. Figure 3.4 gives a visual pathway for non-terminated armchair PNRs while Figure 3.5 displays the same picture for the terminated case. Figure 3.6 shows the lowest energy fragmentation pathway for non-terminated zigzag PNRs while the terminated case is shown in Figure 3.7.

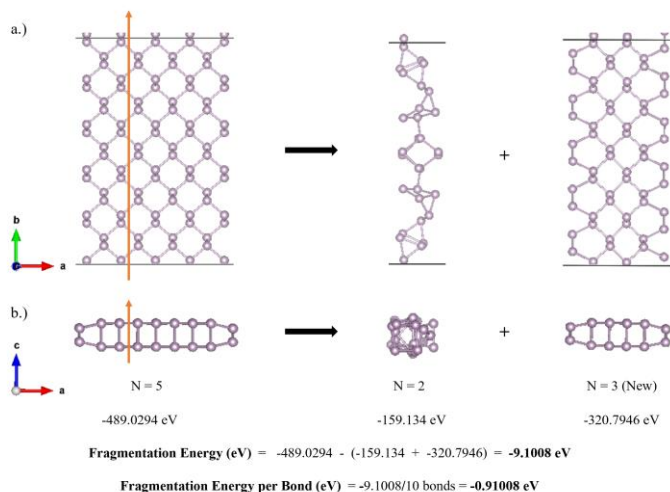


Figure 3.4. Lowest energy fragmentation pathway for non-terminated APNR, width $N = 5$, showing cleavage point as well as the subsequent geometry optimized fragments for top-down (a.) and face-on (b.) views. Note the significant reconstruction of the $N = 2$ fragment and persistent edge reconfiguration of the $N = 3$ (New) fragment.

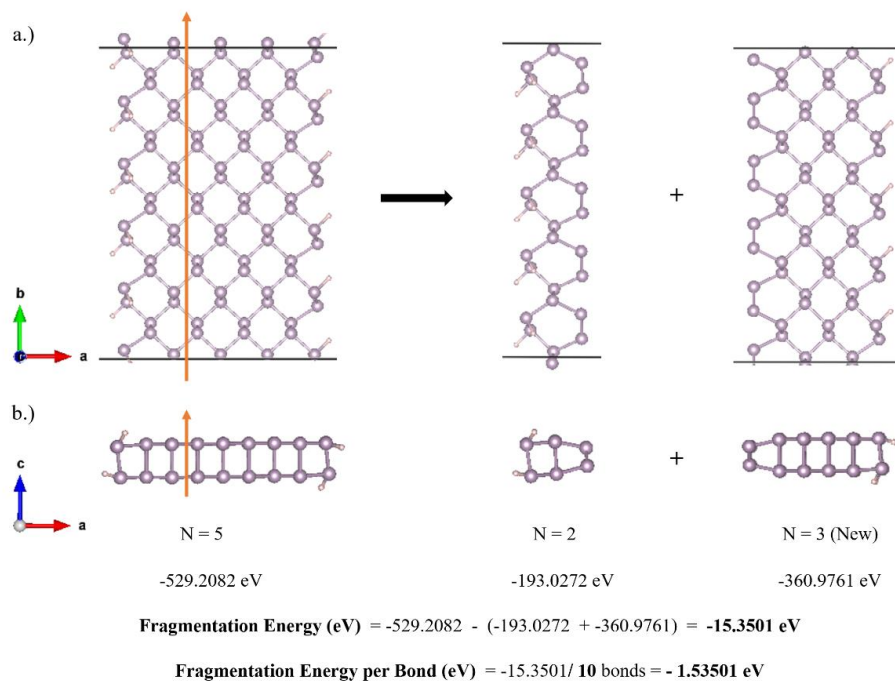


Figure 3.5. Lowest energy fragmentation pathway for terminated APNR, width $N = 5$, showing cleavage point as well as the subsequent geometry optimized fragments for top-down (a.) and face-on (b.) views.

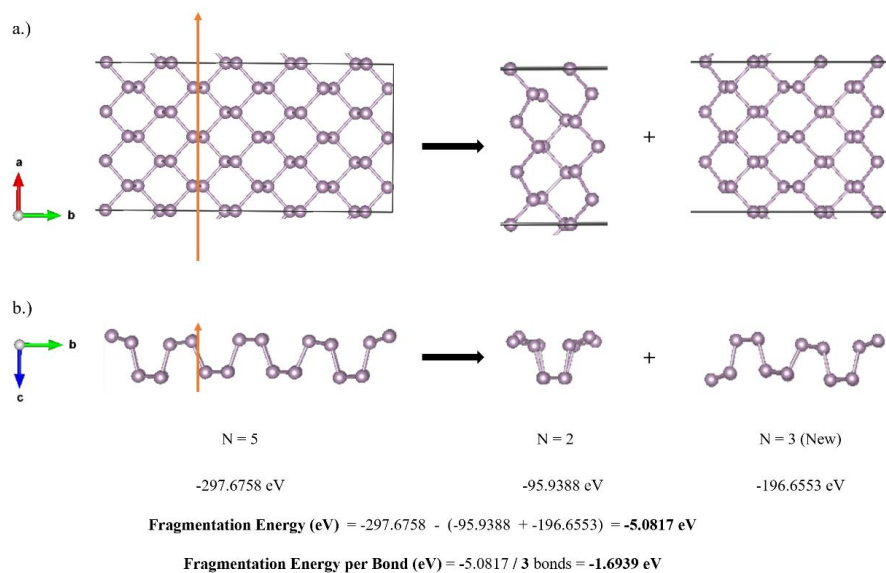


Figure 3.6. Lowest energy fragmentation pathway for non-terminated ZPNR, $N = 5$, showing cleavage point of the ribbon for top down (a.) and face on (b.) views as well as the geometry optimized fragments.

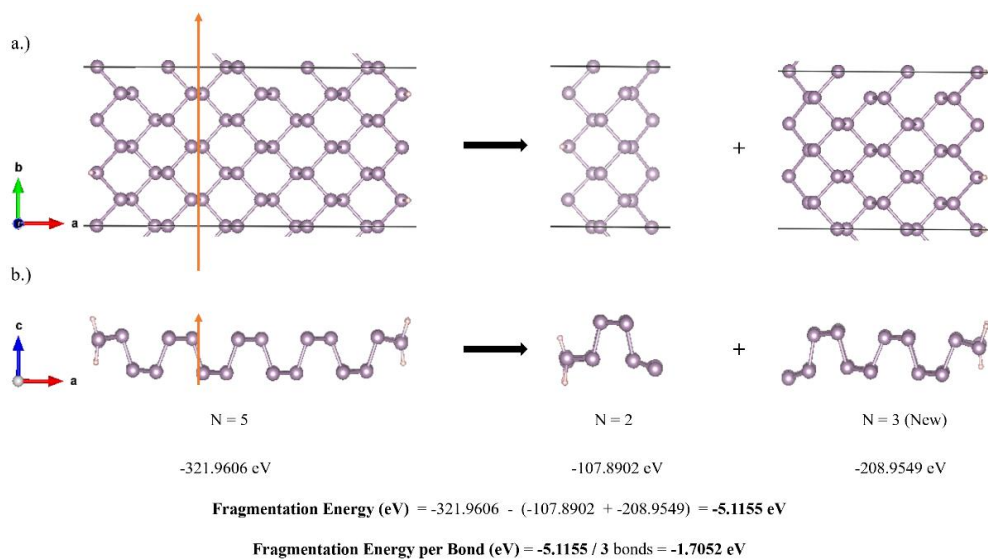


Figure 3.7. Lowest energy fragmentation pathway for terminated ZPNR, $N = 5$, showing cleavage point of the ribbon for top down (a.) and face on (b.) views as well as the geometry optimized fragments.

Experimental synthesis of phosphorene nanoribbons by Watts and Picco et al., highlighted the stability of the individual ribbons in ambient conditions compared to the two-dimensional sheets which are known to degrade in hours.[14,23] The zig-zag ribbons lasted up to six days in lab conditions before degrading and the degradation was observed at the edges of the ribbons as opposed to the surface.[14] Our interest in the stability of the ribbons stems from these findings but we have focused the research around potential fragmentation pathways or thermodynamic stability as opposed to looking into the chemical stability. In other words, the investigation explored the question - if larger ribbons were to break apart, which fragments would be the most energetically favorable? In answering this question, we may find trends in the way these ribbons fragment. Let us first visit the method by which the ribbons were generated and how exactly we defined fragmentation of the various ribbon widths. In order to generate fragments by splitting the larger ribbons into parts bonds must be broken along the length of the ribbon similar to the chemical scissors method outlined in the study by Watts, and Picco et al.[14] As it is impractical in some cases to consider all possible fragmentation pathways, we chose to mitigate dangling phosphorus atoms at the edges of the fragments when splitting the “whole/parent” ribbons. This was accomplished by careful choice of bond breaking location for each potential composition of fragments such that the edge geometry matched that of the parent ribbon. Locations for fragmentations are previously outlined in Figures 3.4-3.7 by a red arrow followed by the geometry optimized fragments. Fragment compositions varied by ribbon but followed the same method of utilizing every possible combination of two fragments which sum to the single parent ribbon. Combinations were limited by the perceived size limit of the smallest possible fragment i.e., a ribbon of width

$N = 2$. Beyond this ribbon width, armchair geometry does not persist. Additionally, there is terminology to consider in the fragmentation pathways. Since we chose to mitigate dangling phosphorus atoms in our exploration of fragmentation pathways, the ribbons cannot be split into fragments of equal size, nor can they fragment into two ribbons abiding by the naming convention outlined previously in this section. Instead, these constraints result in the formation of a fragment with an additional column of atoms and are subsequently labeled “new.”

In order to obtain fragmentation energy values a simple equation is followed in which the combined energies of individual fragments are subtracted from the larger or complete ribbon: $E_R - (E_{F1} + E_{F2})$, where E_R = energy of the complete ribbon, and $E_{F1,2}$ are energies of the respective fragments. It is important to note that use of this equation results in a fragmentation energy value which denotes how close in energy the complete ribbon is to its summed parts. Thus, a more negative value implies a larger energy difference between parts and whole and therefore the energy required to separate the complete structure into those parts is greater. As a result, we are looking for the minimum (smallest) fragmentation energy since it implies that there is a smaller energy difference between the lowest energy whole ribbon and the parts into which it fragments. Figure 3.8 graphs the smallest fragmentation energy per bond broken for structure for APNRs (a) and ZPNRs (b). These values are calculated by dividing the value obtained in the fragmentation energy equation by the number of bonds broken in the unit cell to generate the respective fragments. In other words, taking the value from the equation $-(E_R - (E_{F1} + E_{F2}))$, and dividing by number of bonds broken in order to generate the fragments to obtain fragmentation energy per bond.

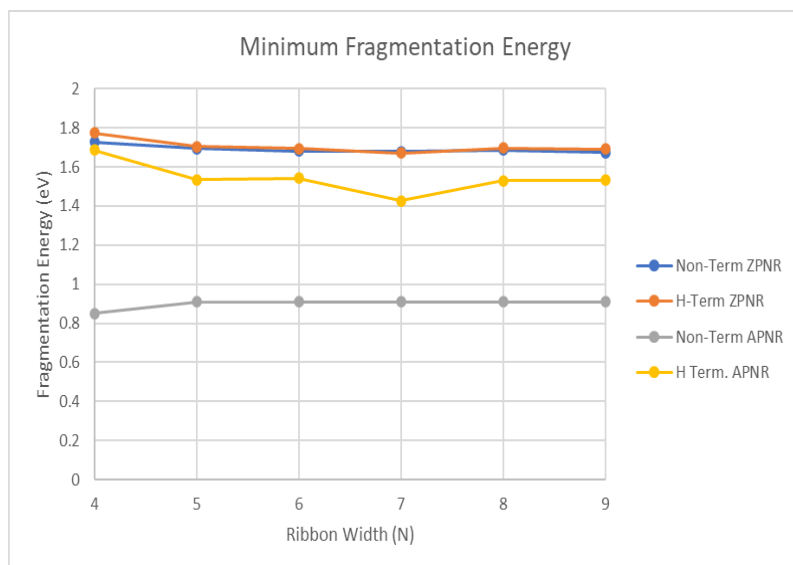


Figure 3.8. Graph of minimum fragmentation energies for respective ribbon types. Note, the significant shift in fragmentation energy for non-terminated APNRs could be a result of the rearrangement occurring in the small fragment ($N = 2$)

A theme emerged among fragmentation pathways for most of the structures including terminated and non-terminated APNRs as well as non-terminated ZPNRs. For each of these ribbons, $N = 4 - 9$, the lowest energy fragments contain an $N = 2$ fragment. The reason for this effect could be two-fold; a rearrangement of the smallest fragment to produce a significantly lower energy than the pre-relaxed structure, and, the fact that the other fragment is the largest possible fragment able to sum to the full ribbon width. The shift in fragmentation energy seen in the non-terminated APNRs could be an artifact of this pattern as well in which the most dramatic rearrangement occurs at small sizes, especially for the non-terminated ribbons as pictured in Figure 3.4. Thus, in this case, the dramatic rearrangement leading to an energy gain in combination with the larger fragment will produce a significant decrease in overall energy when largest and smallest fragments are summed together as opposed to two fragments of similar size.

Extreme reconstruction at the end range size limits for APNRs could be an effect of lack of coordination along the width of the ribbon resulting in a shift from the black phosphorus, puckered armchair configuration to something more reminiscent of tetrahedral phosphorus.

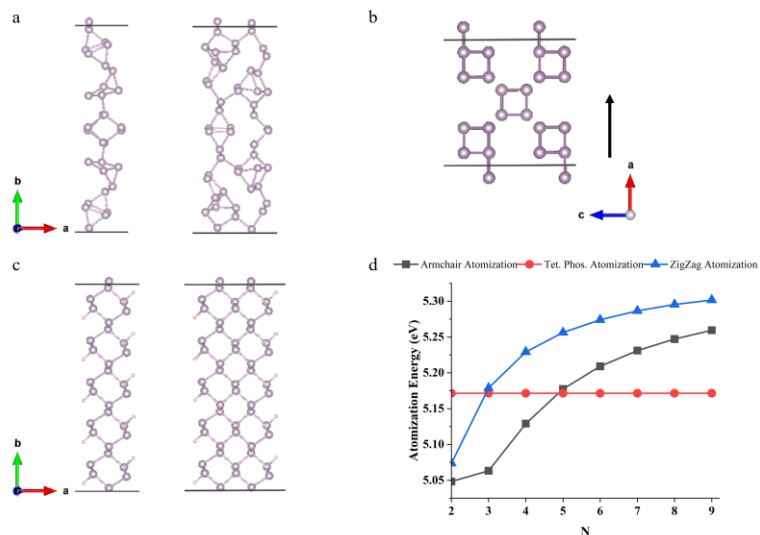


Figure 3.9. Comparison of geometric reconstruction in the small, non-terminated armchair ribbons ($N = 2$ (a), left and $N = 3$ (a), right). (b) Structure for tetrahedral phosphorous used to compare energies with the reconstructed non-terminated APNRs (c) The reconstruction demonstrated by the hydrogen terminated PNRs, showing minimal reconstruction. (d) Energy comparison of APNRs, $N = 2 - 9$, with tetrahedral phosphorous. Note, the horizontal axis, ‘N,’ is indicative of ribbon width.

To investigate further, “ribbons” of tetrahedral phosphorus were created and optimized in order to approximately compare the energetics of the $N = 2,3$ APNRs with ribbons consisting solely of tetrahedral phosphorus. The geometry of the tetrahedral ribbon can be seen in Figure 3.9b, while a comparison of the difference in atomization between tetrahedral phosphorus ribbon and APNRs for $N = 2, 3, 4$, and 5 can be seen in Figure 3.9d. Atomization energy values in both the tetrahedral ribbons and non-terminated

APNRs were obtained by simply taking the ground state energy for the individual ribbon, E_R , and dividing by the number of atoms in the unit cell to obtain energy per phosphorus atom, or, $\frac{E_R}{\# P \text{ atoms}} = E_{per \text{ atom}}$. To analyze these findings, we looked at the geometric reconstruction of non-terminated and terminated ribbons at small sizes. We were particularly interested in ribbons with N=2 and 3 that had non-terminated and edges terminated with H atoms, as they are the preferred fragmentation products. In each case, the structure was allowed to fully relax without any symmetry constraint. We can see that the preferential rearrangement at small sizes decays quickly for ribbon widths beyond N = 3 and the black phosphorus configuration is the more energetically favorable. Note, Figures 3.4-3.7 show that with the addition of edge passivation, or termination, with hydrogen atoms, the rearrangement does not happen to the same degree and the black phosphorus configuration persists even for small sizes N = 2,3. In the examination of fragmentation pathways, this atomic rearrangement reappears to a smaller extent for the edge-passivated ribbons (seen in Figure 3.5) due to the fact that a half-passivated ribbon is generated as a result of fragmenting the parent ribbon. Figure 3.9a shows the structure of the non-terminated reconstructed nanoribbon, Figure 3.9b shows the tetrahedral model, and Figure 3.9c shows the reconstructed H-terminated nanoribbon. Note that the ribbons with unterminated edges undergo strong reconstruction whereas ribbons with H terminated edges only undergo minor structural rearrangement. Relaxation considerably lowers the energy. The energy gain for unterminated N=2 is 0.42 eV per atom while it is 0.20 eV per atom for N=3. The relaxation energy is the difference between the energy for the structure based on the optimized structure of single layer phosphorene and the fully relaxed structure. The relatively large stability of the N=2 nanoribbon is responsible for the

preferred fragmentation pathway of the parent ribbon into N-2 (a fragment that is 2 layers less than the original nanoribbon) and N=2 component nanoribbons. For this reason, the non-terminated APNR is much easier to fragment than the other nanoribbons due to the N=2 nanoribbon being highly stable as compared to the black phosphorus structure. In the H-terminated, APNR, N=4 is the most stable nanoribbon, suggesting that armchair nanoribbons may be more stable as small nanoribbons than larger sheets. For the ZPNR, we see little size-dependence on the stability of the nanoribbon, but a slight enhancement at N=4. This size has the largest stability due to the fact that fragmentation forms two N=2 fragments which are not energetically favorable. It is useful to compare the fragmentation energy per bond to the corresponding energy per bond in a white phosphorus nanoribbon that consists of tetrahedral clusters. Or, in other words, a nanoribbon constructed of clusters, and not bulk white phosphorus. In Figure 3.9d we compare the atomization energy in ribbons of various widths with the corresponding energy in a ribbon of white phosphorus. The fragmentation energy crossover, with the nanoribbon being more stable than the white phosphorus form, at sizes larger than occurs at N=5 for the Armchair, and at N=3 for the Zigzag. This means that armchair is less stable than highly reconstructed fragments up until this size, while for Zigzag, the black phosphorus structure is more stable than the cluster form of phosphorus, so reconstruction is much less likely.

3.3 Band Structure and Band Gap Scaling with Width and Edge Passivation:

As discussed in the introduction a suite of literature has explored bandgap characteristics from bulk to single layer black phosphorus and variable ribbon width.[34-38] Bulk black phosphorus is known to have a direct bandgap value of 0.3eV while

monolayer black phosphorus (phosphorene) possesses a direct bandgap of 1.51eV.[35] In general, band gap value increases with decreasing number of layers or decreasing width of the PNR. Thus, it has been said that the increase in bandgap follows an increase in confinement effects from decreasing number of layers or increase in the contributions of edge states in the ribbons of decreasing width.[35] These confinement effects are a result of the edge states playing a more or less significant role as the physical width (and subsequent number of allowed states) increases or decreases. As a result, the nature of edge passivation and amount of reconstruction play a significant role in the bandgap values of the PNRs²⁰. For example, in the case of hydrogen edge termination, edge states are quenched leading to an increase in overall bandgap from the edge-unpassivated PNRs.[20] Additionally, due to phosphorene's anisotropy, bandgap values of the ribbons vary based on ribbon type as well as width while general scaling behavior depends on the ribbon type.[38] We can see these aspects displayed in Figure 3.10. Non-terminated APNRs have a lower bandgap than their hydrogen-terminated counterparts and non-terminated ZPNRs are metallic while the hydrogen-termination of ZPNRs' edges introduces a bandgap within the ribbons.

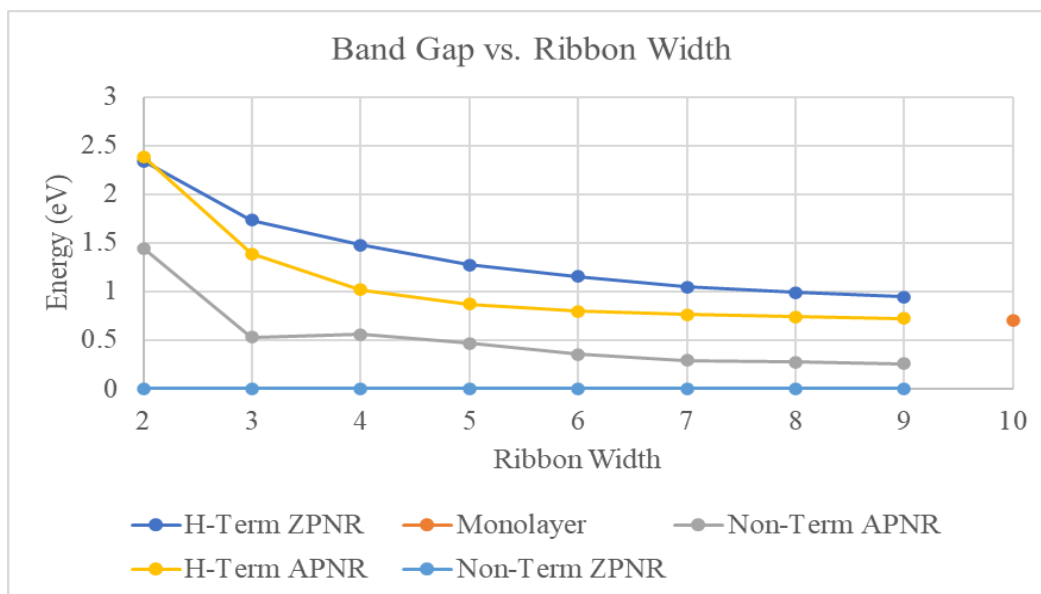


Figure 3.10. Band gap values as a function of PNR width in direct comparison with ribbon type, termination and the monolayer sheet.

Previous work by Tran et al. has defined this scaling behavior to be $1/w^2$ for hydrogen-terminated APNRs while hydrogen-terminated ZPNRs exhibit $1/w$ where $w =$ ribbon width in nanometers.[38] Interestingly, this scaling behavior is due to the character of charge carriers which is directly affected by how the width is confined in the nanoribbons. In general, this scaling behavior dictates that APNR bandgap values will decay more quickly than ZPNR counterparts of similar widths. Thus, ZPNRs tend to have larger gap values than do APNRs of nearly the same width.[38] This behavior can be seen in Figure 3.10 where, beyond widths $N = 3$, the bandgap trends follow those outlined by Tran et al. and others.[35,37,38] Band gap values do indeed decrease as ribbon width increases and values for hydrogen-terminated ZPNRs are larger than their hydrogen-terminated APNR counterparts. It is important to note the following: first, as discussed in the introduction, the results shown are a product of the PBE functional and are thus undervalued bandgaps compared to the use of hybrid functional HSE06.[55] Second,

results given in this dissertation are produced for ribbon widths ranging from $N = 2 - 9$. In the review of literature, the typical range of ribbon widths is around $N = 5 - 14$. [38] Therefore, the discrepancy in the scaling behavior for the ribbon width at small sizes ($N = 2,3$) may be twofold. First, their exclusion from previous work may indicate that the scaling behavior does not hold for such small sizes. Second, the significant geometric reconstruction seen in the previous section may cause a shift in bandgap which is not described by traditional scaling behavior. Thus, lack of hydrogen termination to stop reconstruction and quench edge states could be the reason that the scaling behavior is different in the non-terminated case. Note instead of immediate decay of bandgap values, minor oscillations are present at end-range sizes ($N = 2-4$) for non-terminated armchair PNRs. For hydrogen-terminated ZPNR and APNR the gap values for $N = 2$ are nearly identical which could also be an artifact of small size. In all cases the treatment of the exchange correlation term in the PBE functional could also play a role in the observed results.

Concerning the character of the bandgap (i.e. direct or indirect), similar trends were also observed for bandgap variance between the direct and indirect behavior. Tran et al. show that the local valence band maximum at the gamma point yields bandgap values which are within 20meV of the true indirect bandgap shifted slightly away from the gamma point. [38] Thus, the ground state character of the terminated ZPNR and APNRs' bandgaps is technically indirect, however, due to the bandgap's significant dependence upon strain, it is posited that this small difference would be difficult to detect experimentally. As such, we consider them functionally as direct bandgap materials. Similar trends were observed in this research under the PBE functional with terminated

PNRs. In contrast, however, non-terminated APNRs show a more significant difference of about 0.12eV on average between gamma point band gap and slightly shifted true bandgap. In this case strain induced by room temperature thermal energy may not be significant enough to ignore the indirect bandgap behavior. Additionally, with such a small size range the significance of confinement effects and strain become imperative upon deposition as ribbons interact with the substrate surface (Sorkin et al).[20] For the non-terminated N=5 armchair ribbon, our calculated value of the band gap energy is 0.47 eV as compared to 0.53 eV obtained by H. Guo et al. [23] The slight difference is most likely due to a different treatment of the van der Waals interactions between the two studies. We utilized DFT-D3 method with Becke-Johnson damping while the related study used the dispersion-corrected DFT method, optB88-vdW. [23]

3.4 Work Function and Electron Affinity Observations:

3.4.1 Hydrogen-Terminated Zigzag Phosphorene Nanoribbons

The work function of a material, or the minimum energy required to remove an electron from the material's surface, becomes indispensable knowledge when constructing devices which have some dependence upon thermionic or photoelectric emission. This knowledge becomes even more invaluable when the characteristics of the device are dependent upon tuning heterostructure materials at the nanoscale. In the interest of characterizing phosphorene nanoribbons in a fashion similar to which the single to multi-layer phosphorene has been studied, preliminary results for work function values of hydrogen-terminated ZPNRs of various widths were obtained. In a first principles study performed by Yongqing Cai et al., a trend of decreasing work function as the number of layers of 2D phosphorene sheets increases from 1 to 5.[24] A similar, less pronounced

trend can be seen in Figures 3.11 and 3.12 as the ribbon widths increase from $N = 2 - 9$. Work function values were obtained by subtracting the Fermi energy of the ribbons from the vacuum energy surrounding the ribbon, or,

$$W = -e\phi - E_F \quad 3.1$$

where $-e$ = charge of an electron, ϕ = electrostatic potential of the vacuum level near the surface of the material and E_F = the Fermi energy of the system. The work function value slowly approaches the single layer 2D sheet value of 4.50 eV quoted in previous literature.[24] Since work function is also dependent upon confinement effects one might expect the value to follow similar trends with ribbon width, i.e. as the ribbon increases in width the value of the work function decreases until it approaches the monolayer value.[24] This is indeed what the results show for zigzag PNRs.

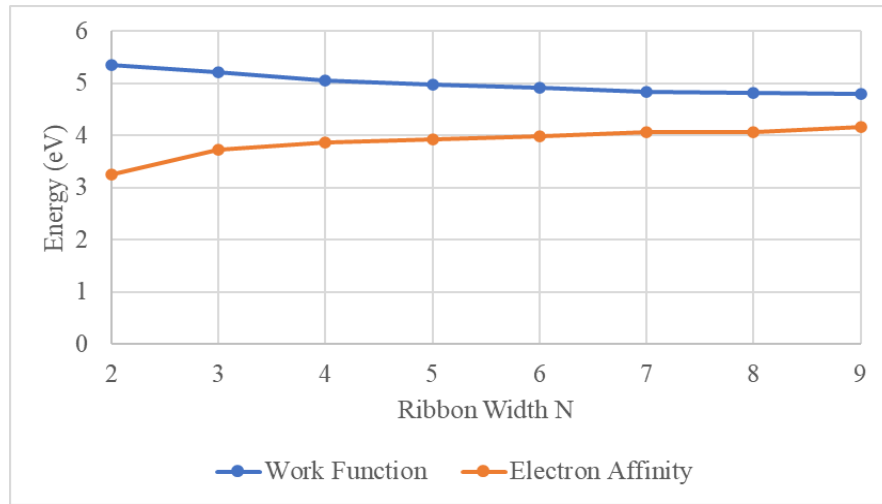


Figure 3.11. Work function and electron affinity as functions of increasing ribbon widths for hydrogen-terminated zigzag PNRs.

Of similar importance and close relation, but distinct from the work function and more commonly referred to when characterizing semiconductor materials is the electron affinity. In solid-state physics the electron affinity of a material is defined as the energy

gain achieved by an electron moving from vacuum, just outside the surface of the material, to the bottom of its conduction band within the semiconductor. This can be seen below in the Equation 3.2:

$$\mathbf{E}_{ea} = \mathbf{E}_{vac} - \mathbf{E}_C \quad 3.2$$

Where \mathbf{E}_{vac} is the vacuum energy and \mathbf{E}_C is the energy of the conduction band of the semiconductor. Since the electron affinity is a surface property, we might expect to see a similar trend to the work function arise when observing width-related confinement effects on a two-dimensional semiconductor. Figure 3.11 shows the results of varying width on hydrogen-terminated zigzag PNRs. Interestingly, we see inverse behavior when comparing the electron affinity to the work function with varying ribbon widths. While electron affinity should not necessarily change much for a bulk material with doping, at small sizes there are minor but relevant changes to the observed results. The fermi level shifts from -4.66 eV to -2.71 eV for armchair PNRs of ribbon width $N = 2$ to $N = 9$ while the conduction band remains somewhat constant. Additionally, there are some interesting shifts in the vacuum energy between even and odd numbered ribbons as widths increase. Ultimately, the upward shift in vacuum energy while conduction band energy remains mostly constant dictates the inverse relation between work function and electron affinity. Changes in fermi level, vacuum energy and conduction band energy can be seen in Figure 3.12.

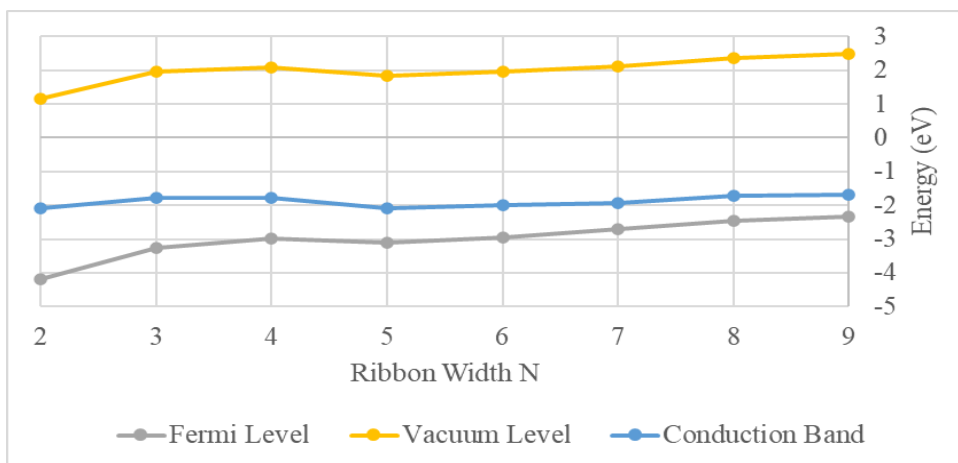


Figure 3.12. Comparison of Fermi level, vacuum level, and conduction band for zigzag PNRs. Note, Conduction band remains relatively constant with changes in width while the vacuum level and fermi level are pushed up overall.

3.4.2 Hydrogen-Terminated Armchair Phosphorene Nanoribbons

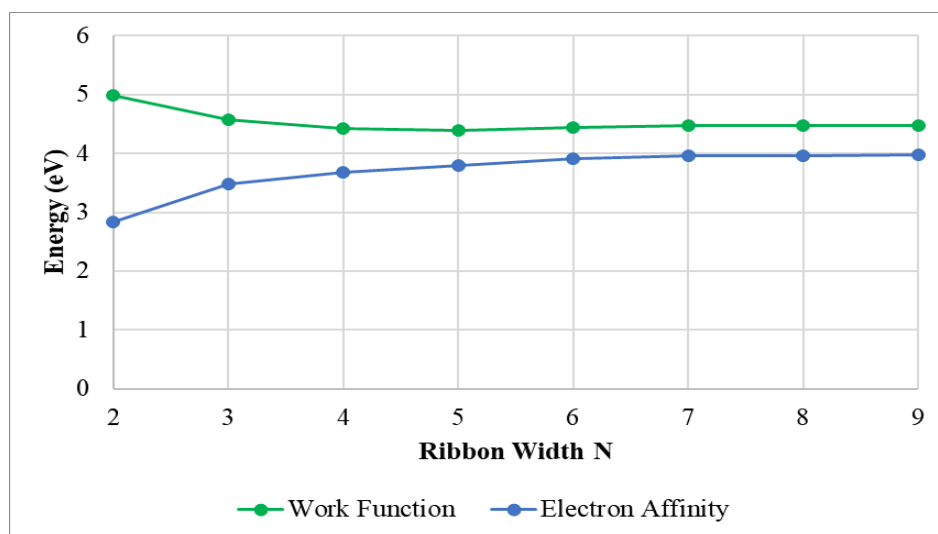


Figure 3.13. Work function and electron affinity as functions of increasing ribbon widths for hydrogen-terminated armchair PNRs.

We can see a similar trend for armchair PNRs in Figure 3.13 which shows the same inverse behavior when comparing the electron affinity to the work function with varying ribbon widths. The fermi level in armchair PNRs undergoes a significant change with respect to varying ribbon width while the conduction band shifts upwards slightly. In this case too there is an overall increase in vacuum level as the ribbons grow wider with the total difference between $N = 2$ and $N = 9$ proving larger than the shift for zigzag ribbons by about 0.13eV . Again, the upward shift in vacuum energy while conduction band energy remains mostly constant dictates the inverse relation between work function and electron affinity.

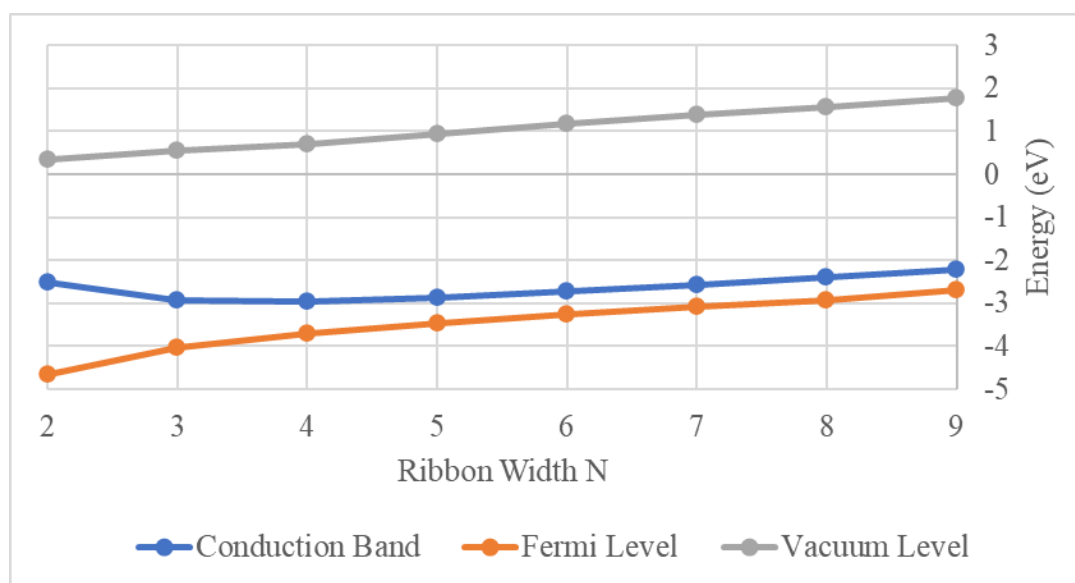


Figure 3.14. Comparison of Fermi level, vacuum level, and conduction band for hydrogen-terminated armchair PNRs. Note, Conduction band remains relatively constant with changes in width while the vacuum level and fermi level are pushed up overall.

3.5 Bader Charge Analysis:

Bader charge analysis was performed on all ribbons in the interest of deducing what might be happening with charge location associated with rearrangement of non-passivated

PNRs as well as how that behavior may shift with the addition of hydrogen atom edge passivation. It was found in the non-terminated case, that there was approximately even distribution of charge along the width of the ribbon with no large variance at the location of any phosphorus atom within the ribbon.

For the hydrogen-terminated ribbons, Bader charge was calculated at all edge atoms and all hydrogen atoms to observe the charge associated with binding between phosphorus and hydrogen.[66-69] Average Bader charge was then obtained for edge phosphorus and hydrogen atoms for all ribbon widths and recorded in Table 3.1 below. Note, in the calculation of Bader charge, one obtains the difference between effective valence given in the POTCAR for a particular atom and the Bader charge for each atom in the output file to obtain the residual charge left on each atom. A negative value indicates that there is additional charge beyond the given Z -value for a particular atom meaning that atom has accepted charge, in this case, as the result of bond formation. Charge located at the edge phosphorus atoms was about 0.33 on average for the armchair PNRs and 0.34 for all zigzag PNRs, compared to the inner phosphorus atoms, with approximately zero charge. Charge on hydrogen atoms averaged about -0.32 for armchair PNRs while zigzag PNRs maintained an average of approximately -0.33. This suggests that the phosphorus atoms are acting as donors while the hydrogen atoms act as acceptors in the formation of a bond between the two at the ribbon edges.

Table 3.1. Comparison of average Bader Charge for edge phosphorus and hydrogen atoms of various ribbon widths.

Average Bader Charge				
	APNR		ZPNR	
Ribbon Width	Hydrogen	Phosphorus	Hydrogen	Phosphorus
2	-0.3249	0.3399	-0.3387	0.3544
3	-0.3243	0.3352	-0.3388	0.3594
4	-0.3153	0.3278	-0.3333	0.3439
5	-0.3216	0.3354	-0.3232	0.3294
6	-0.3206	0.3378	-0.3335	0.3382
7	-0.3179	0.3311	-0.3370	0.3548
8	-0.3218	0.3383	-0.3335	0.3375
9	-0.3203	0.3372	-0.3267	0.3357

3.6 Summary and Conclusions

Work presented in this chapter verified that width and edge passivation indeed have significant effects on bandgap and minor effects on the material's work function and electron affinity, while the investigation of relative stability supports a particular fragmentation pathway for all ribbons. The parent ribbon splits into component fragments of width $N = 2$ and $N - 2$. Results inspire several questions which motivate and propel further study of alternative methods for tuning the electronic properties of phosphorene and phosphorene nanoribbons. Specifically, since termination or edge passivation plays a significant role in controlling and introducing a bandgap in ribbons, is it possible to fine-tune these effects by varying termination? If so, what impact is made on other electronic properties like work function or electron affinity which act as initial indicators of performance upon incorporation into a device setting? Is it possible to employ the ideas of

chemical doping to these materials to not only control band gap but the nature of carriers?

Chapter 4 continues the journey and makes a concerted effort to begin answering the former questions.

References

1. Novoselov, K. S. et al. Electric field effect in atomically thin carbon films. *Science* **306**, 666–669 (2004).
2. Akhtar, M., Anderson, G. et al. “Recent advances in synthesis, properties, and applications of phosphorene”. *npj 2D Materials and Applications* volume 1, Article number: 5 (2017)
3. Ashton, M.; Paul, J.; Sinnott, S. B.; Hennig, R. G. (2017). "Topology-Scaling Identification of Layered Solids and Stable Exfoliated 2D Materials". *Phys. Rev*
4. Prasad S.V.S., Mishra R.K., Gupta S., Prasad S.B., Singh S. (2021) Introduction, History, and Origin of Two Dimensional (2D) Materials. In: Singh S., Verma K., Prakash C. (eds) Advanced Applications of 2D Nanostructures. Materials Horizons: From Nature to Nanomaterials. Springer, Singapore.
5. Butler, S. Z. et al. Progress, challenges, and opportunities in two-dimensional materials beyond graphene. *ACS Nano* **7**, 2898–2926 (2013).
6. Bhimanapati, G. R. et al. Recent advances in two-dimensional materials beyond graphene. *ACS Nano* **9**, 11509–11539 (2015).
7. Thompson, Brianna C., et al. “Graphite Oxide to Graphene. Biomaterials to Bionics.” *Advanced Materials*, vol. 27, no. 46, Dec. 2015, pp. 7563–82. *DOI.org (Crossref)*, <https://doi.org/10.1002/adma.201500411>.
8. Duan, X., Wang, C., Pan, A., Yu, R. & Duan, X. Two-dimensional transition metal dichalcogenides as atomically thin semiconductors: opportunities and challenges. *Chem. Soc. Rev.* **44**, 8859–8876 (2015)
9. Gibaja, C. et al. Few-layer antimonene by liquid-phase exfoliation. *Angew. Chem. Int. Ed.* doi:10.1002/anie.201605298 (2016).
10. Ares, P. et al. Mechanical isolation of highly stable antimonene under ambient conditions. *Adv. Mater.* **28**, 6332–6336 (2016)
11. Li, Xinming et al. “Graphene and related two-dimensional materials: Structure-property relationships for electronics and optoelectronics.” *Applied physics reviews* **4** (2017): 021306.
12. Gosling, J.H., Makarovsky, O., Wang, F. et al. Universal mobility characteristics of graphene originating from charge scattering by ionised impurities. *Commun Phys* **4**, 30 (2021). <https://doi.org/10.1038/s42005-021-00518-2>
13. Ferrari, A. C. et al. Science and technology roadmap for graphene, related two-dimensional crystals, and hybrid systems. *Nanoscale* **7**, 4598–4810 (2015).
14. Watts, Mitchell C., et al. “Production of Phosphorene Nanoribbons.” *Nature*, vol. 568, no. 7751, Apr. 2019, pp. 216–20. *DOI.org (Crossref)*, <https://doi.org/10.1038/s41586-019-1074-x>.
15. Li, L. K. et al. Black phosphorus field-effect transistors. *Nat. Nanotechnol.* **9**, 372–377 (2014).
16. Qiao, J. S., Kong, X. H., Hu, Z. X., Yang, F. & Ji, W. High-mobility transport anisotropy and linear dichroism in few-layer black phosphorus. *Nat. Commun.* **5**, 4475 (2014).

17. Liu, H. et al. Phosphorene: an unexplored 2D semiconductor with a high hole mobility. *ACS Nano* **8**, 4033–4041 (2014).
18. Xia, F. N., Wang, H. & Jia, Y. C. Rediscovering black phosphorus as an anisotropic layered material for optoelectronics and electronics. *Nat. Commun.* **5**, 4458 (2014).
19. Lee, S. et al. Anisotropic in-plane thermal conductivity of black phosphorus nanoribbons at temperatures higher than 100 K. *Nat. Commun.* **6**, 8573 (2015).
20. Sorkin, V., Cai, Y., Ong, Z., Zhang, G. & Zhang, Y. W. Recent advances in the study of phosphorene and its nanostructures. *Crit. Rev. Solid State Mater. Sci.* **42**, 1–82 (2017).
21. Lewis, E. A., Brent, J. R., Derby, B., Haigh, S. J. & Lewis, D. J. Solution processing of two-dimensional black phosphorus. *Chem. Commun. (Camb.)* **53**, 1445–1458 (2017).
22. Li, W. F., Yang, Y. M., Zhang, G. & Zhang, Y. W. Ultrafast and directional diffusion of lithium in phosphorene for high-performance lithium-ion battery. *Nano Lett.* **15**, 1691–1697 (2015).
23. Hongyan Guo, Ning Lu, Jun Dai, Xiaojun Wu, and Xiao Cheng Zeng. Phosphorene Nanoribbons, Phosphorus Nanotubes, and van der Waals Multilayers. *J. Phys. Chem. C* **118** (25), 14051-14059 (2014).
24. Cai, Y., Zhang, G. & Zhang, YW. Layer-dependent Band Alignment and Work Function of Few-Layer Phosphorene. *Sci Rep* **4**, 6677 (2014).
<https://doi.org/10.1038/srep06677>
25. A. K. Geim and I. V. Grigorieva, *Nature* 499, 419 (2013).
26. Liu, N. O. Weiss, X. Duan, H. Cheng, Y. Huang, and X. Duan, *Nat. Rev. Mater.* **1**, 16042 (2016).
27. Jariwala, T. J. Marks, and M. C. Hersam, *Nat. Mater.* **16**, 170 (2017).
28. S. Novoselov, A. Mishchenko, A. Carvalho, and A. H. Castro Neto, *Science* **353**, aac9439 (2016).
29. Ajayan, P. Kim, and K. Banerjee, *Phys. Today* **69**(9), 38 (2016).
30. Li and H. Zhu, *Phys. Today* **69**(9), 46 (2016).
31. McKinney, R. W., et al. Ionic vs. van der Waals layered materials: identification and comparison of elastic anisotropy, *J. Mater. Chem. A*, 2018, **6**, 15828-15838
32. Toberer, Eric S., et al. “Electronic Structure and Transport in Thermoelectric Compounds AZn₂Sb₂ (A = Sr, Ca, Yb, Eu).” *Dalton Trans.*, vol. 39, no. 4, 2010, pp. 1046–54. DOI.org (Crossref), <https://doi.org/10.1039/B914172C>.
33. Preparation, Characterization and Electrochemical Properties of La₂CuO₄@Au as a Novel Bifunctional Oxygen Electrode.” *International Journal of Electrochemical Science*, Oct. 2020, pp. 9933–39. DOI.org (Crossref), <https://doi.org/10.20964/2020.10.74>
34. Na, Junhong, et al. “Few-Layer Black Phosphorus Field-Effect Transistors with Reduced Current Fluctuation.” *ACS Nano*, vol. 8, no. 11, Nov. 2014, pp. 11753–62. DOI.org (Crossref), <https://doi.org/10.1021/nm5052376>.
35. Zhang, J., et al. “Phosphorene Nanoribbon as a Promising Candidate for Thermoelectric Applications.” *Scientific Reports*, vol. 4, no. 1, Dec. 2014, p. 6452. DOI.org (Crossref), <https://doi.org/10.1038/srep06452>.

36. Guo, Hongyan, et al. "Phosphorene Nanoribbons, Phosphorus Nanotubes, and van Der Waals Multilayers." *The Journal of Physical Chemistry C*, vol. 118, no. 25, June 2014, pp. 14051–59. DOI.org (Crossref), <https://doi.org/10.1021/jp505257g>
37. Ploog, Klaus, and Gottfried H. Döhler. "Compositional and Doping Superlattices in III-V Semiconductors." *Advances in Physics*, vol. 32, no. 3, Jan. 1983, pp. 285–359. DOI.org (Crossref), <https://doi.org/10.1080/00018738300101561>.
38. Tran, Vy, and Li Yang. "Scaling Laws for the Band Gap and Optical Response of Phosphorene Nanoribbons." *Physical Review B*, vol. 89, no. 24, June 2014, p. 245407. DOI.org (Crossref), <https://doi.org/10.1103/PhysRevB.89.245407>.
39. W. D. Knight, K. Clemenger, W. A. de Heer, W. A. Saunders, M. Y. Chou, and M. L. Cohen, *Phys. Rev. Lett.* **52**, 2141 (1984).
40. Knight, W. D., et al. "Alkali Metal Clusters and the Jellium Model." *Chemical Physics Letters*, vol. 134, no. 1, Feb. 1987, pp. 1–5. DOI.org (Crossref), [https://doi.org/10.1016/0009-2614\(87\)80002-7](https://doi.org/10.1016/0009-2614(87)80002-7).
41. Khanna, Shiv N., et al. "The Superatomic State beyond Conventional Magic Numbers: Ligated Metal Chalcogenide Superatoms." *The Journal of Chemical Physics*, vol. 155, no. 12, Sept. 2021, p. 120901. DOI.org (Crossref), <https://doi.org/10.1063/5.0062582>.
42. Reber, Arthur C., and Shiv N. Khanna. "Co₆Se₈(PEt₃)₆ Superatoms as Tunable Chemical Dopants for Two-Dimensional Semiconductors." *Npj Computational Materials*, vol. 4, no. 1, Dec. 2018, p. 33. DOI.org (Crossref), <https://doi.org/10.1038/s41524-018-0092-9>.
43. Martin, T. P., et al. "Shell Structure of Clusters." *The Journal of Physical Chemistry*, vol. 95, no. 17, Aug. 1991, pp. 6421–29. DOI.org (Crossref), <https://doi.org/10.1021/j100170a009>.
44. Harbola, M. K. "Magic Numbers for Metallic Clusters and the Principle of Maximum Hardness." *Proceedings of the National Academy of Sciences*, vol. 89, no. 3, Feb. 1992, pp. 1036–39. DOI.org (Crossref), <https://doi.org/10.1073/pnas.89.3.1036>.
45. D. E. Bergeron, P. J. Roach, A. W. Castleman, N. O. Jones, and S. N. Khanna, *Science* 307, 231 (2005).
46. D. E. Bergeron, A. W. Castleman, T. Morisato, and S. N. Khanna, *Science* 304, 84 (2004).
47. J. U. Reveles, S. N. Khanna, P. J. Roach, and A. W. Castleman, *Proc. Natl. Acad. Sci. U. S. A.* 103, 18405 (2006).
48. A. C. Reber, S. N. Khanna, and A. W. Castleman, *J. Am. Chem. Soc.* 129, 10189 (2007).
49. Spear, W. E. & Le Comber, P. G. Substitutional doping of amorphous silicon. *Solid State Commun.* 17, 1193–1196 (1975).
50. Erwin, S. C. et al. Doping semiconductor nanocrystals. *Nature* 436, 91–94 (2005).
51. Yu, J. et al. Patterning superatom dopants on transition metal dichalcogenides. *Nano Lett.* 16, 3385–3389 (2016).
52. Wang, Q. H., Kalantar-Zadeh, K., Kis, A., Coleman, J. N. & Strano, M. S. Electronics and optoelectronics of two-dimensional transition metal dichalcogenides. *Nat. Nanotechnol.* 7, 699–712 (2012).

53. Kiriya, D., Tosun, M., Zhao, P., Kang, J. S. & Javey, A. Air-stable surface charge transfer doping of MoS₂ by benzyl viologen. *J. Am. Chem. Soc.* 136, 7853–7856 (2014).
54. Schellenberger, A., Schlaf, R., Pettenkofer, C. & Jaegermann, W. Synchrotroninduced surface-photovoltage saturation at intercalated NaWSe₂ interfaces. *Phys. Rev. B* 45, 3538–3545 (1992).
55. Perdew, J. P., Burke, K. & Ernzerhof, M. Generalized gradient approximation made simple. *Phys. Rev. Lett.* 77, 3865–3868 (1996).
56. Krukau, A. V., Vydrov, O. A., Izmaylov, A. F. & Scuseria, G. E. Influence of the exchange screening parameter on the performance of screened hybrid functionals. *J. Chem. Phys.* 125, 224106 (2006).
57. Ling, Xi, et al. “The Renaissance of Black Phosphorus.” *Proceedings of the National Academy of Sciences*, vol. 112, no. 15, Apr. 2015, pp. 4523–30. *DOI.org (Crossref)*, <https://doi.org/10.1073/pnas.1416581112>.
58. Welch, Eric J., and Jeffrey R. Long. “Atom-Like Building Units of Adjustable Character: Solid-State and Solution Routes to Manipulating Hexanuclear Transition Metal Chalcogenide Clusters.” *ChemInform*, vol. 37, no. 2, Jan. 2006. *DOI.org (Crossref)*, <https://doi.org/10.1002/chin.200602221>.
59. Hafner, Juergen. “ChemInform Abstract: Ab-Initio Simulations of Materials Using VASP: Density-Functional Theory and Beyond.” *ChemInform*, vol. 39, no. 47, Nov. 2008. *DOI.org (Crossref)*, <https://doi.org/10.1002/chin.200847275>.
60. Yang, Y., Castano, C. E., Gupton, B. F., Reber, A. C. & Khanna, S. N. A fundamental analysis of enhanced cross-coupling catalytic activity for palladium clusters on graphene supports. *Nanoscale* 8, 19564–19572 (2016).
61. Yang, Y. et al. More than just a support: graphene as a solid-state ligand for palladium-catalyzed cross-coupling reactions. *J. Catal.* 360, 20–26 (2018).
62. Grimme, S. Semiempirical GGA-type density functional constructed with a longrange dispersion correction. *J. Comput. Chem.* 27, 1787–1799 (2006).
63. Kresse, G. & Furthmüller, J. Efficient iterative schemes for ab initio total-energy calculations using a plane-wave basis set. *Phys. Rev. B* 54, 11169–11186 (1996).
64. Neugebauer, J. & Scheffler, M. Adsorbate-substrate and adsorbate-adsorbate interactions of Na and K adlayers on Al(111). *Phys. Rev. B* 46, 16067–16080 (1992).
65. Roberts, F. S., Anderson, S. L., Reber, A. C. & Khanna, S. N. Initial and final state effects in the ultraviolet and X-ray photoelectron spectroscopy (UPS and XPS) of size-selected Pd_n clusters supported on TiO₂(110). *J. Phys. Chem. C* 119, 6033–6046 (2015).
66. W. Tang, E. Sanville, and G. Henkelman A grid-based Bader analysis algorithm without lattice bias, *J. Phys.: Condens. Matter* 21, 084204 (2009).
67. E. Sanville, S. D. Kenny, R. Smith, and G. Henkelman An improved grid-based algorithm for Bader charge allocation, *J. Comp. Chem.* 28, 899-908 (2007).
68. G. Henkelman, A. Arnaldsson, and H. Jónsson, A fast and robust algorithm for Bader decomposition of charge density, *Comput. Mater. Sci.* 36, 354-360 (2006).
69. M. Yu and D. R. Trinkle, Accurate and efficient algorithm for Bader charge integration, *J. Chem. Phys.* 134, 064111 (2011).

Chapter 4. Controlling the Location of Quantum States in Phosphorene Nanoribbons via Edge Passivation with Various Ligands

4.1 Introduction

Chapter 3 showed our work in verifying previously observed properties of phosphorene nanoribbons. Tuning bandgap via controlling width and edge-passivation offer promising levers in the proverbial tool kit of materials engineering which one can utilize in future device settings. However, there has not been a demonstration of control over p-/n- character of phosphorene. Nor has there been convincing evidence one can pointedly manipulate the work function or electron affinity. The key objective of the present work is to propose a novel approach to controlling the placement of conduction and valence band edges. It is demonstrated that this can be accomplished by passivating the edge sites with charge transfer ligands. By attaching charge transfer ligands, one can create dipoles at the edges which can effectively change the vacuum level. It is interesting to highlight that the addition of ligands does change the Fermi energy but this change is not driven by a change in the valence count but by the formation of charge transfer dipoles at the edges. These intriguing features are observed by first considering a cluster model of phosphorene in which a flake with 141 phosphorus atoms is ligated with the following ligands, NH₂, OH, H, SCH₃, SH, Cl, OCN, and OCH₃. These flakes have approximate dimensions of 2.9 nm length x 1.9 nm width. Use of the cluster model enabled a more direct investigation of ligand effects as dipole moments and adiabatic ionization energies could be calculated for all structures with the additional support of unbalanced ligations to

single out dipole effects. Periodic structures of zigzag phosphorene nanoribbons of width $N = 9$ possessed edges decorated with donor or acceptor ligands. Ligand choice is governed by the groups that have electro-negativities different from phosphorus to passivate the edges which could lead to the formation of polar bonds that, in turn, could affect the work function. The following group of ligands was used to terminate the phosphorene nanoribbon edges: NH_2 , OH , H , SCH_3 , SH , Cl , and OCN . It is worth noting these ligands are ordered in terms of their widely accepted donor strength – increasing from left to right. However, phosphorene is an exceptional electron donor and, as shown in Bader charge analysis, acts accordingly to varying degrees rendering the convention moot in this specific environment. Results show that it is likely the effects of the cumulative dipoles which act to change the vacuum energy and subsequently work function of the system. In the cluster model, a change in ionization energy can be directly related to an energetic shift in the highest occupied molecular orbital (HOMO) and lowest unoccupied molecular orbital (LUMO). A direct manifestation of this change is the removal of electrons from HOMO. Consequently, the first results presented are on cluster models where it is shown that the shifts in HOMO/LUMO result in subsequent change in the ionization energy. Thus, we relate HOMO/LUMO shifts with the formation of dipoles at the ligand-ribbon edge interface. In the periodic nanoribbon model, the effect of edge passivation with various ligands on the material's work function are considered.

4.2 Cluster Model – an Investigation of the Nature of Edge Ligands Leading to a Shift in Molecular Orbitals and Ionization Energy

To understand the effect of ligands on the ionization energy and work function of phosphorene, a cluster model of phosphorene was utilized. This allowed for the direct

determination of ionization energy for each sheet. The cluster model was constructed from 141 P atoms and 35 H atoms, as shown in Figure 4.1. This leads to a sheet with length of about 2.9 nm and a width of 1.7 nm. The cluster shows slight bending as the hydrogen termination is in the cis position, and the HOMO-LUMO gap of the phosphorene model is 1.24 eV. The adiabatic ionization energy, the energy difference between the optimized neutral and cationic structure is 5.68 eV. A Hirshfeld charge analysis finds that there is relatively little charge transfer between the phosphorus and the hydrogen termination with the charge on the H being from -0.01 to -0.02 e^- , and the average charge on the phosphorus being less than +0.01 e^- . The HOMO of the cluster is constructed from lone pair on the phosphorus, and the LUMO of the cluster is also constructed from the lone pair on phosphorus, but the LUMO has a node running through the central plane of the cluster (Appendix A). The cluster has a small dipole of 2.3 Debye that runs roughly perpendicular to the plane of the cluster due to the preponderance of P-H bonds pointing up as seen in Figure 4.1.

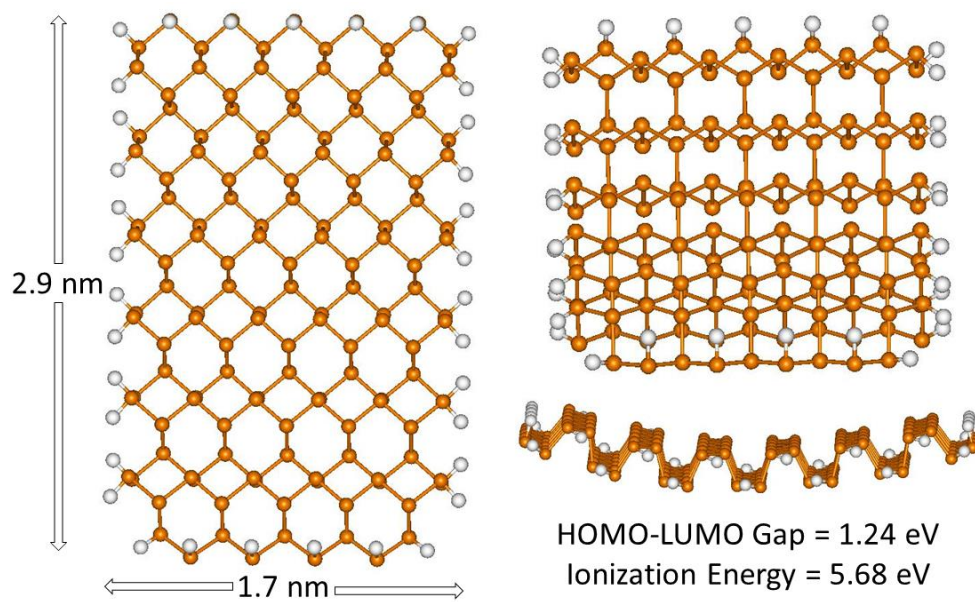


Figure 4.1 The structure of the Phosphorene cluster model, $P_{141}H_{35}$, top view, front view, and side view.

To understand the effect of terminating the phosphorene sheet with different ligands on the redox and electronic properties, we systematically replaced the H atom with a series of other ligands. These ligands were OCN, Cl, OH, H, OCH_3 , SCH_3 , and NH_2 . The structures of the cluster models are shown in Figure 4.2. Substituting the H termination has little effect on the HOMO-LUMO gap, as the lowest HOMO-LUMO gap is for NH_2 with a gap of 1.18 eV, and largest is OCH_3 with a gap of 1.26 eV. The absolute value of the HOMO and LUMO versus the vacuum level are plotted in Figure 4.3. We see that while the HOMO-LUMO gap is mostly unchanged, there is a dramatic change in the absolute value of HOMO and LUMO. OCN has the lowest lying HOMO, and the absolute value of HOMO increases monotonically as we move to Cl, SH, H, OH, OCH_3 , SCH_3 , and NH_2 . This suggests that the ionization energy of the phosphorene sheets with different termination will have significantly different ionization energies.

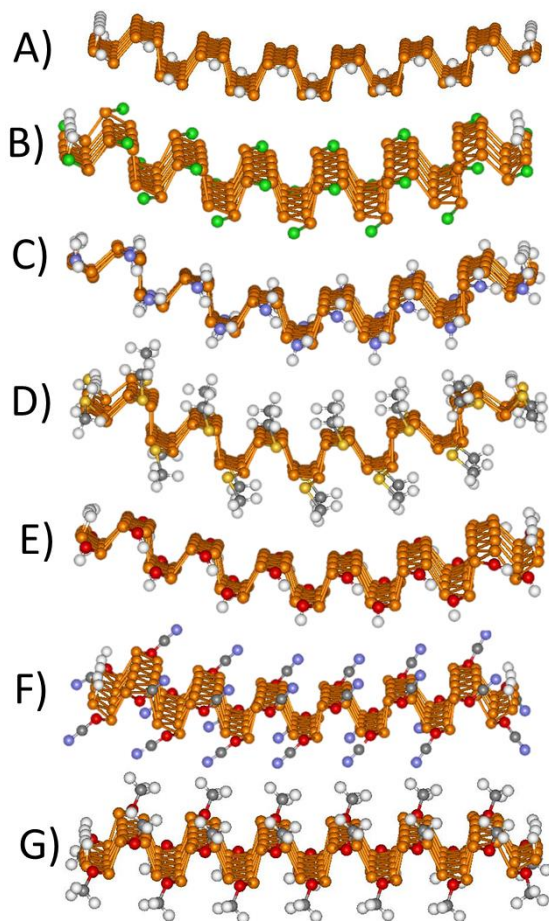


Figure 4.2 The structure of the Phosphorene cluster models with the following termination, A) H B) Cl, C) NH₂, D) SCH₃, E) OH, F) OCN, and G) OCH₃.

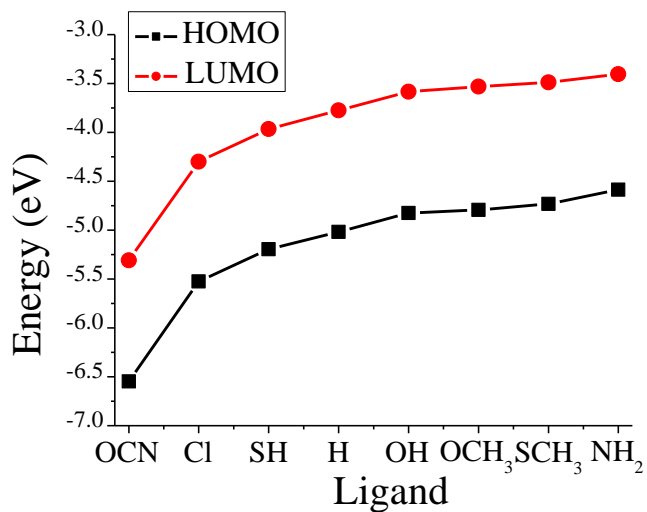


Figure 4.3 The HOMO and LUMO energy of the Phosphorene cluster models as a function of the ligand.

We next examine the electronic properties of the phosphorene cluster models with differing termination. Figure 4.4 shows the ionization energy of the phosphorene cluster model as a function of the termination. We see that the largest ionization energy is OCN, with an ionization energy of 7.09 eV, followed by Cl with an ionization energy of 6.20 eV. The next lowest ionization energy is SH, followed by H, OH, OCH₃, SCH₃, and NH₂. Notice that this follows the same pattern as the HOMO energies. This means that the changes in the ionization energy are due to initial state effects. In other words, the trend in the ionization energy is not due to the electronic relaxation of the cation, but rather, the effect is due to the dipole induced band bending or the bonding between the ligand and cluster. Observations subsequently discussed suggest that the most likely explanation of the changing ionization energy is the band bending due to the dipole formed by the ligand.

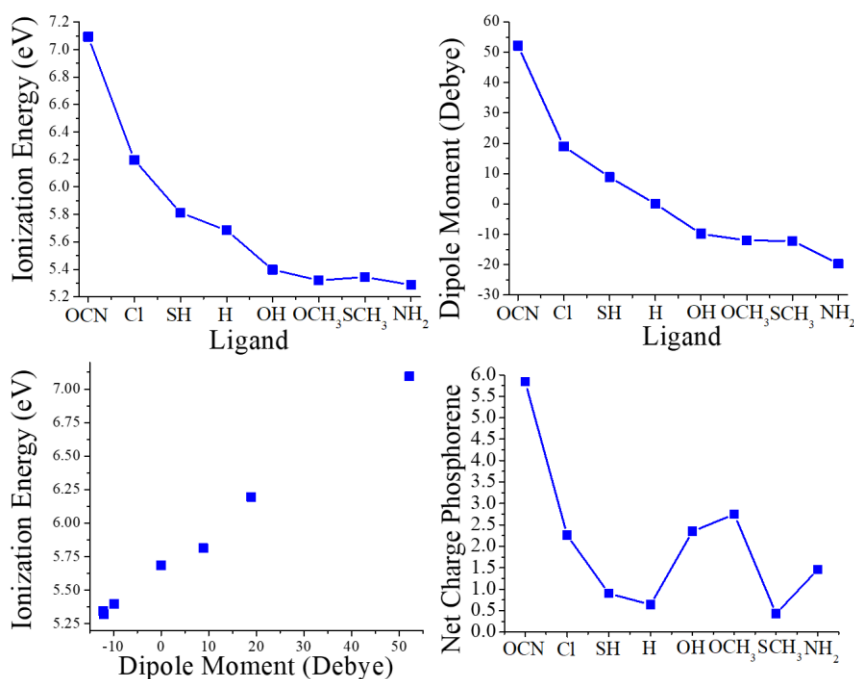


Figure 4.4 The ionization energy, dipole moment, a comparison of the ionization energy and dipole moment, and the net charge on the phosphorene as compared to the ligand. The dipole moment is calculated by binding one side of the sheet with the ligand and the other

side is hydrogen terminated. The dipole moment is positive if it is pointing from the ligand to the phosphorene, and negative if it is pointing from the phosphorene to the ligand.

To test whether the shift in the ionization energy was due to a dipole-induced band bending, we next analyzed phosphorene model clusters that are H-terminated on one side, and terminated by our list of ligands on the other. From this, we can find the dipole moment across the cluster. The hypothesis we are testing is that the dipole that is formed by the ligand terminating the phosphorene sheet causes band bending that raises or lowers the HOMO energy versus the vacuum energy. By comparing the dipole moment with the changes in the ionization energy, we may test this hypothesis. Note, that when we analyze a cluster with the same ligands on both sides, there is no significant net dipole moment as the charge distributions across both sides of the sheet are roughly symmetric counteract each other. This is an advantage of the cluster model as we can find the dipole moment and compare it with the ionization energy. In Figure 4.4, we see the dipole moment in Debye as a function of the terminal ligand. The structure of the half-ligated model clusters are shown in Figure 5, along with the dipole moment vector. The dipole vector points from negative charge to positive charge. We note that the trend in the dipole moment matches exactly with trend in the ionization energy. In Figure 4.4, we plot the ionization energy versus the component of the dipole moment that is perpendicular to the ligand-phosphorene interface, and we see an extremely strong correlation between the strength and direction of the dipole vector and the ionization energy. The largest dipole which is pointing to the right is for the OCN cluster. This is due Nitrogen having a large negative charge of $-0.23 e^-$, with the C having an average charge of $+0.10 e^-$, and the O having an average charge of $-0.10 e^-$. This produces a net dipole of 52.1 Debye pointing from the ligand towards the phosphorene

sheet. Note that the dipole is not primarily caused by the charge transfer between the ligand and the phosphorene sheet, but instead it is caused by the dipole of the ligand itself. In comparison, Cl results in an 18.9 Debye dipole moment pointing from the Cl to the phosphorene sheet. This is caused by charge transfer from the Cl to the phosphorene, with the Cl having an average Hirshfeld charge of $-0.10 e^-$. Note that this is less than the charge on N in OCN, and for this reason, the dipole moment is lower. Next is OH which has a dipole moment of 9.8 Debye pointing from the phosphorene to the ligand. This is caused by the OH itself where the dipole points from the O atom to the H atom. OCH₃ and SCH₃ are next with dipole moments of 12.0 and 12.2 Debye pointing from the phosphorene to the ligand. The dipole is caused by the ligand itself, the H atoms are charged at $+0.04 e^-$, while the O and S atoms are negatively charged at $-0.17 e^-$, and $-0.01 e^-$, respectively, and the C is $-0.04 e^-$ when paired with O, and $-0.12 e^-$ when paired with S. The result of this is a dipole pointing from the negatively charged O and S to the positively charged H. Finally, we have NH₂ which has a dipole pointing from the negatively charged N at $-0.22 e^-$, which points towards the positively charged H at $+0.10 e^-$. This results in the large dipole that is pointing away from the phosphorene sheet. We also analyzed the charge transfer between the phosphorene and the ligand, as shown in Figure 4.4, to determine if this is a significant factor in the changing ionization energy. The hypothesis here is that a more positive phosphorene will lead to a larger ionization energy as it is more difficult to remove an electron from a more positive material. While OCN has the most positive phosphorene sheet, which is consistent with that ligand causing a large ionization energy in the phosphorene sheet, the remaining ligands show no significant correlation between the amount of charge on phosphorene and the ionization energy. OCN having a very positive

phosphorene sheet is expected at OCN is the only ligand that is expected to have a formal negative charge. OCH₃ has one of the most positive net charges on phosphorene, yet it has one of the lowest ionization energies. This tells us that it is the dipole moment and not the charge transfer that controls the changes in the ionization energy. This analysis finds that the majority of the shift in the ionization energy is due to the dipole moment caused by the ligand leading to band bending.

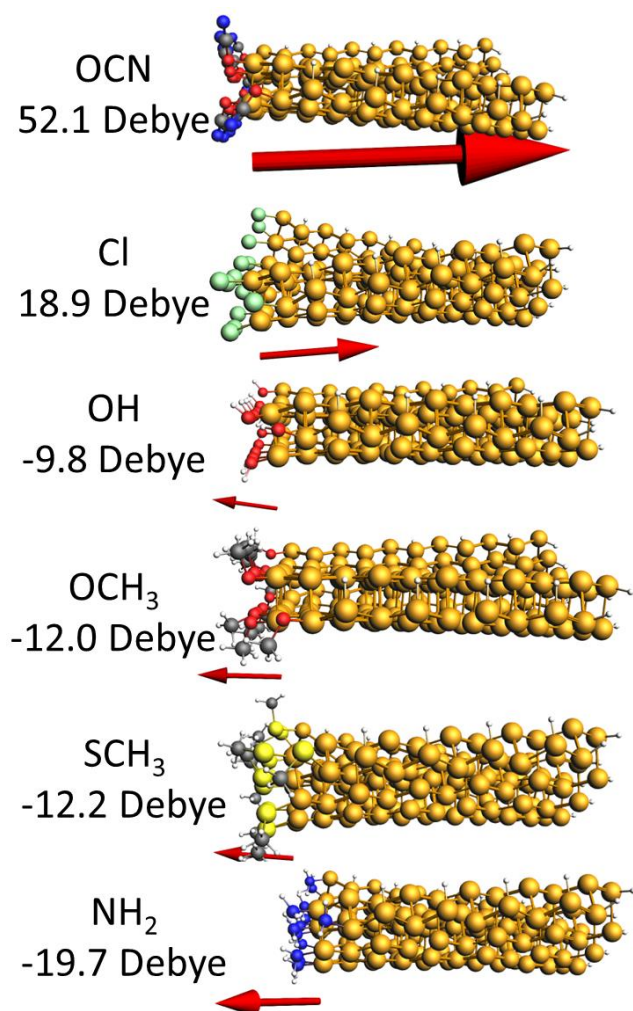


Figure 4.5 The structure of the cluster model of phosphorene with one side ligated with OCN, Cl, OH, OCH₃, SCH₃, and NH₂. The dipole vector is shown in red, and the vector points from the ligand either towards or away from the phosphorene sheet depending on the sign of the dipole moment.

4.3 Effects of Varying Ligation on the Electronic Structure of Periodic Phosphorene Nanoribbons and Chemical Doping via Sodium Adatoms

Following the work on cluster models, are periodic studies on phosphorene nanoribbons. As in the case of cluster models, edge passivation with various ligands leads to change in the work function. A detailed analysis indicated that the change is affected by the cumulative electrostatic potential from the ligands which shifts the valence and conduction band energies. Charge density visualizations show that these effects are non-localized and are spread over the entire surface of the ribbon. The possibility of changing the p-/n- character was also explored. Inspired by the concept of chemical doping, the aim was to alter the Fermi energy by changing the valence count of the system via the adsorption of atoms that can donate or accept charge from the surface. If the Fermi energy can be changed without altering the gap could lead to n or p- type semiconductor. The initial attempt focused on the donation of charge to the phosphorene surface – a potentially difficult feat given the excellent oxidation capabilities of phosphorene. Sodium atoms were adsorbed on the surface of ribbons; given the sodium atom has a low ionization energy of 5.14 eV, one could expect Na atoms to donate charge. However, as seen in the inspection of projected density of states and visualization of charge distribution, Na atoms are close enough to one another to interact forming dimers or other molecules resulting in overlap with the phosphorene p-states and the introduction of vacant states within the gap. Above 2 sodium atoms per unit cell, the Fermi level crosses the conduction band making the material metallic.

4.4 Control of Work Function by Various Edge-Passivation of N = 9 Zigzag Phosphorene Nanoribbon

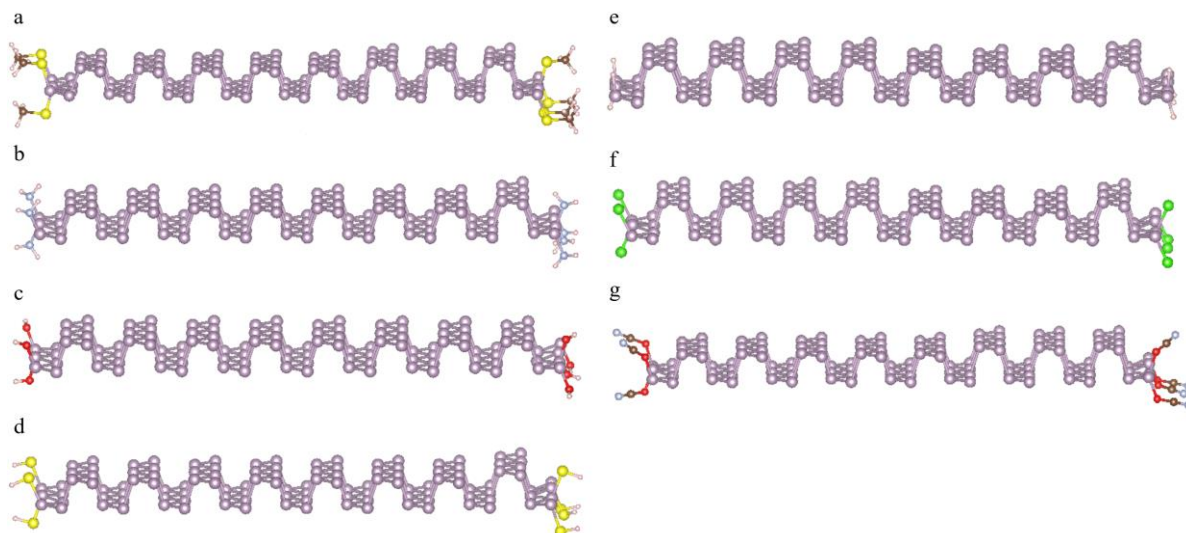


Figure 4.6 Visualization of geometry for various termination/ligations of N=9 zigzag PNR. a) SCH₃ – Terminated, b) NH₂ – Terminated, c) OH – Terminated, d) SH – Terminated, e) H – Terminated, f) Cl – terminated, g) OCN – terminated

Figure 4.6 gives a visualization of the converged zigzag geometry as well as the varying edge-passivation. Here, we can see that there is negligible rearrangement of phosphorene atoms and no effect of strain on the material. Additionally, it is important to note the relative difference in number of phosphorus atoms compared to the number of ligands at the edge sites. As shown later in the PDOS, this leads to a low overall contribution of states from ligands which further supports the theory that observed shifts in work function come, instead, from the dipole effects of the ligands.

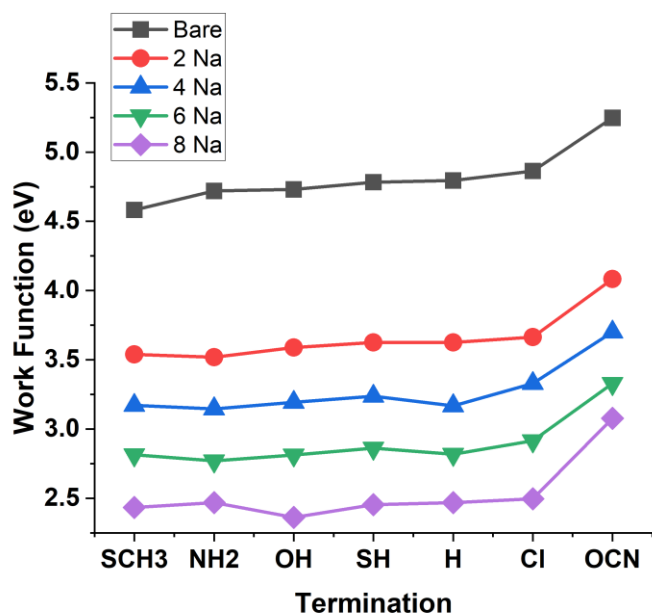


Figure 4.7 Work Function various termination and Na – adsorption with varying concentration

The change in work function as a result of termination from 4.58 eV for SCH₃ to 5.25 eV in the case of OCN termination can be seen in Figure 4.7. Adsorption of sodium at various concentrations (0 to 8 Na atoms per unit cell) has a pronounced effect on the work function of the material as seen in Figure 4.7. However, the result provides an incomplete story as there is also a significant change in bandgap of the material associated with an increasing concentration of adsorbed sodium.

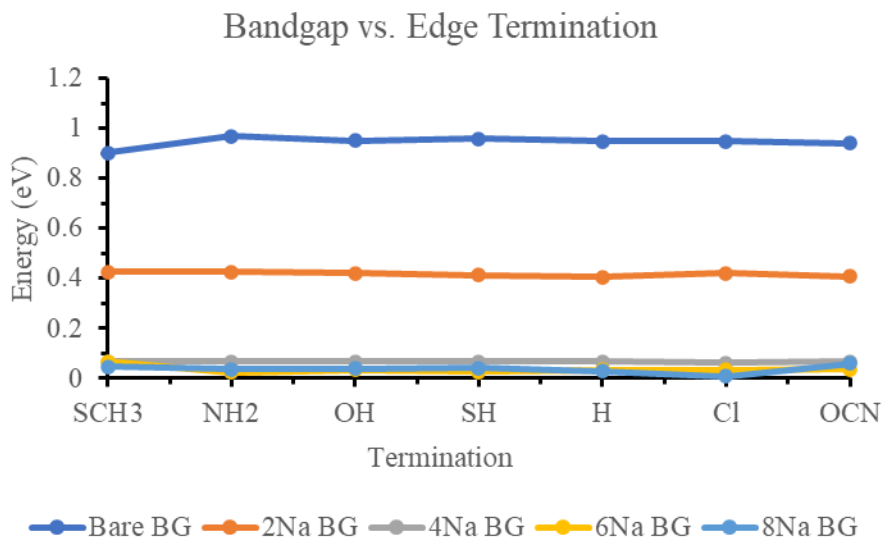


Figure 4.8 Bandgap vs edge termination with adsorbed Na concentration for 0, 2, 4, 6, and 8 Na

As shown in Figure 4.8, there is a shift in bandgap from about 0.94 eV in the case of bare phosphorene nanoribbon to about 0.42 eV when two sodium atoms are adsorbed and metallic past this concentration (4, 6, and 8 Na). Interestingly, the bandgap of the material is unaffected by varying the termination while the work function does change. Figure 4.9 directly compares the constant bandgap and changing work function for the case of a bare phosphorene nanoribbon as ligands differ. Nanoribbons do exhibit minor shifts in the energy of the valence and conduction band as well as the fermi energy, however, they are proportional and the average bandgap value is maintained. The significant effects are the shift in fermi level relative to the vacuum energy leading to the observed change in work function. This is attributed to the dipole effects from ligands as discussed in detail in the previous section explicitly outlining dipole effects in the cluster model.

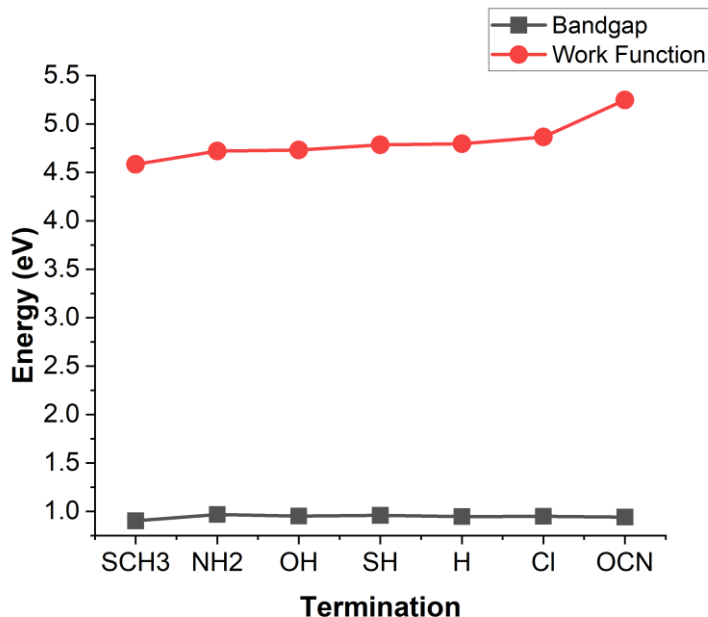
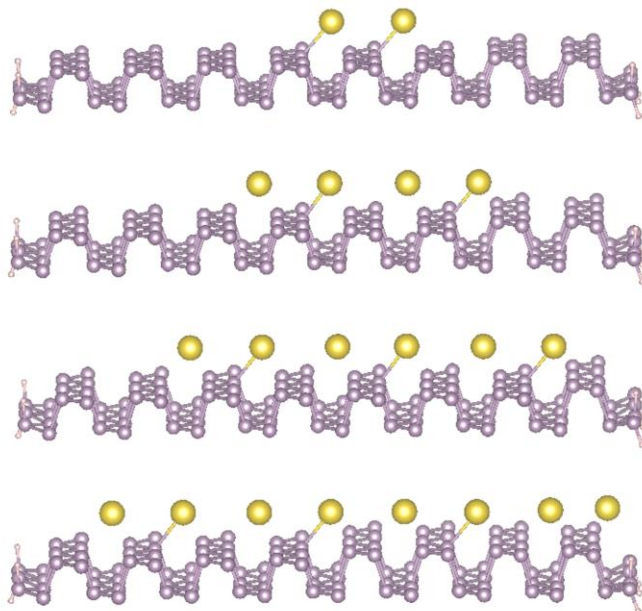


Figure 4.9 Work function and Bandgap vs. Termination for comparison of bandgap change with termination to work function change with termination. B.G. remains constant pointing to level change as a result of dipole effects of edge terminal groups/ ligands.

4.5 Controlling Bandgap and Inducing a Metallic Transition via Sodium Atom Deposition on Phosphorene Nanoribbon Surface

The visualization of nanoribbons with varying sodium concentration can be seen in Figure 4.10. Comparison between 2, 4, 6, and 8 sodium atoms per unit cell are shown for the case of hydrogen termination, however, the method and placement of sodium is consistent for all ligand cases. Additionally, using the hydrogen edge-passivated example structure Figure 4.10 b gives a visualization of the unit cell dimensions used for all terminations of phosphorene nanoribbons. Here we can see clearly the vacuum to either side of the passivated edges as the ribbon propagates in the a-direction. Note, the vacuum space added above the ribbon is about 16.5 angstroms.

a



b

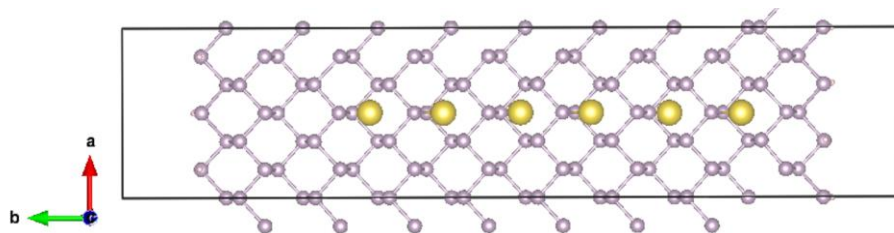


Figure 4.10 Visualization of converged geometry with sodium adsorption. (a) various concentrations of sodium adsorbed on hydrogen edge-passivated $N = 9$ zigzag PNR. (b) Example of standard unit cell dimensions for all nanoribbons using hydrogen edge-passivation.

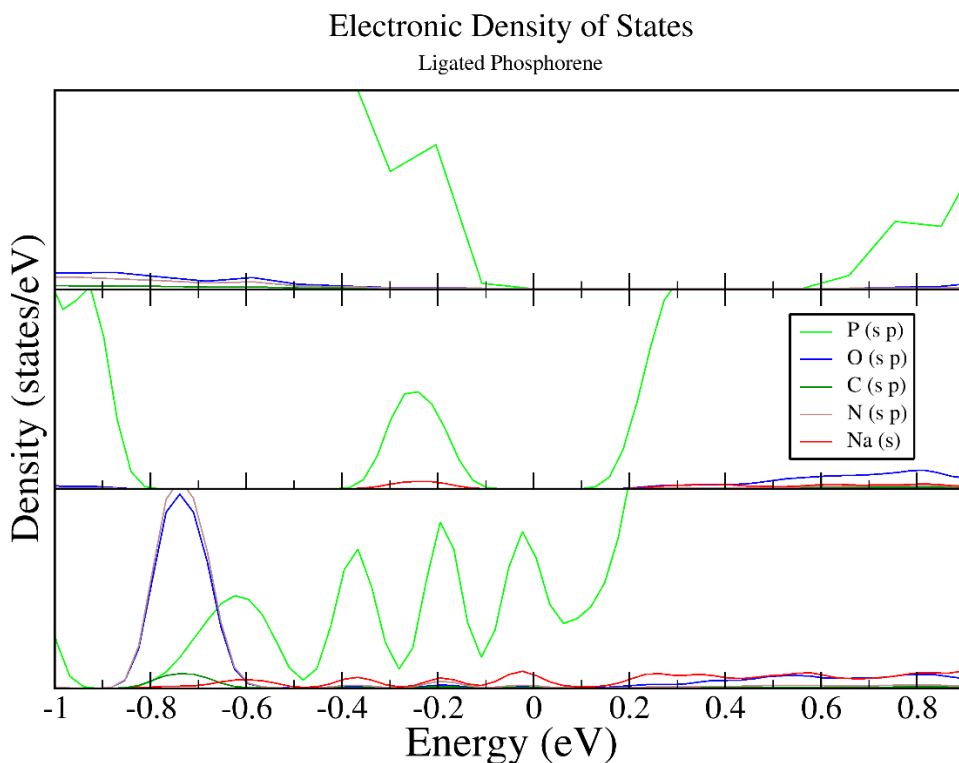


Figure 4.11 Comparison of projected density of states for OCN-Terminated 0, 2, and 8 Na cases, top, middle, and bottom respectively.

Density of states calculations were performed on all sodium-adsorbed structures which yielded similar results. For reference, the case of OCN edge passivation has been included in this discussion to illustrate the underlying mechanism at work for all structures. Observing the density of states in Figure 4.11 in conjunction with the visualization of the wavefunction associated with valence and conduction bands for sodium adsorbed on phosphorene nanoribbons (Figure 4.12) reveals the mechanism of electron donation by sodium is more complex than ionic bonding. In the 2 Na case, it seems that sodium forms a dimer on the surface of phosphorene which then forms a bond akin to a dipolar covalent bond with phosphorene. As such, the dimer interacts as a molecule meaning the donation of charge from the hybridized sodium s-orbitals overlaps with phosphorus lone pairs (p-

orbitals). This interaction leads to the injection of occupied states or electrons into the bandgap creating a new valence band thereby decreasing the bandgap of the material from an average of 0.94 eV to 0.42 eV for the 2 Na case. These findings can be observed in the density of states given by FIGURE 4.11. At higher concentrations, we see the formation of multiple peaks in the density of states from overlapping sodium and phosphorus orbitals. In these cases, the distances between sodium atoms differs with conformational changes resulting in various combinations of dimers and larger groups or single sodium atoms. The dimer picture is rendered inconsistent at these higher concentrations of sodium atoms. However, the increased concentration yields higher charge transfer to the conduction band, thus the emergence of multiple peaks in the DOS (FIGURE 4.11). Continued filling of the conduction band pushes the fermi level above the conduction band producing the observed metallic behavior. A shift from semiconducting to metallic is 4 Na per unit cell. It is possible that the threshold concentration lies at 3 Na, thus further work could be completed to investigate the effects of a single sodium adatom and three sodium adatoms.

The visualization of the wave functions associated with valence and conduction bands shows a picture consistent with that of the projected density of states. The valence band consists of sodium and phosphorus states which have shifted into the bandgap in the 2 Na case while the conduction band lies on the phosphorus atoms. These are marked in Figure 4.12 below.

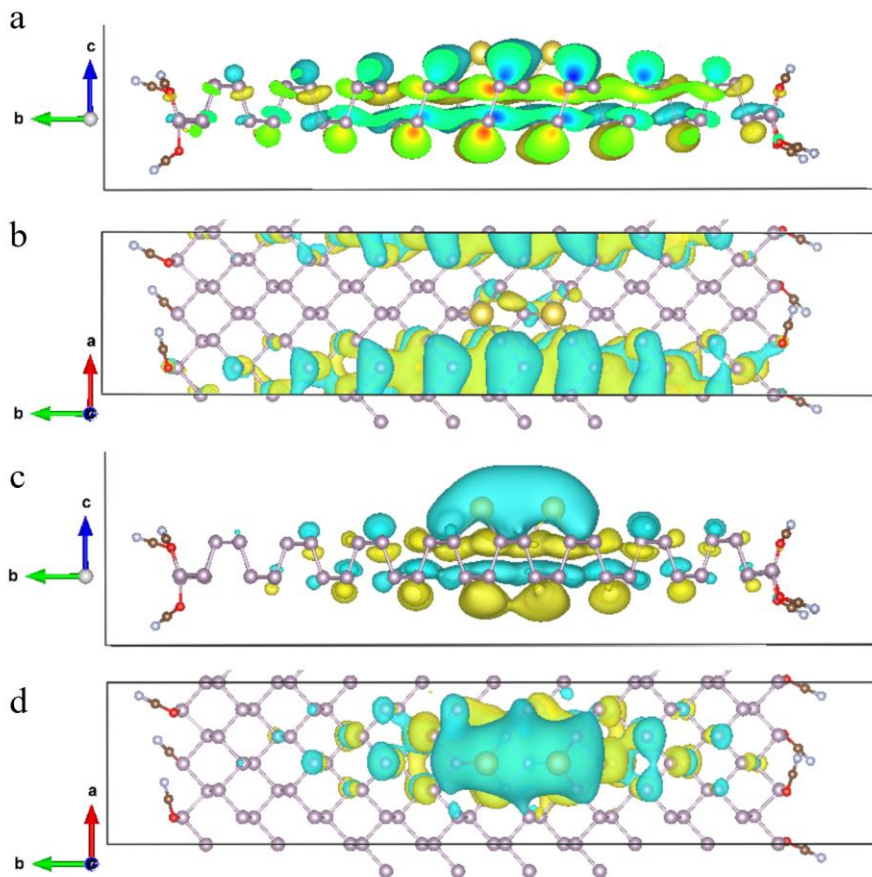


Figure 4.12 Visualization of charge density distribution for conduction band (a, b) and valence band (c, d) in different orientations of the unit cell.

4.6 Bader Charge Analysis of Phosphorene Nanoribbons with Various Edge-Passivation

In order to investigate the charge transfer behavior between the ligands and phosphorene nanoribbons, as well as the adsorbed sodium atoms in the chemical doping example, Bader charge analysis was performed. This indicates which atoms are donating and which are accepting charge further enabling the understanding of what role ligands play in adjusting the quantum states of phosphorene nanoribbons.

Bader charge was calculated at all edge atoms and all hydrogen atoms to observe the charge associated with binding between phosphorus and hydrogen.[48-51] Average Bader charge was then obtained for edge phosphorus and hydrogen atoms for all ribbon widths and recorded in Tables 1 and 2 below. Note, in the calculation of Bader charge, one obtains the difference between effective valence given in the POTCAR file (containing pseudopotential information in the Vienna Ab initio Simulation Package (VASP)) for a particular atom and the Bader charge for each atom in the output file to obtain the residual charge left on each atom. A negative value indicates that there is additional charge beyond the given effective valence for a particular atom meaning that atom has accepted charge, in this case, as the result of bond formation. Thus, we can deduce that a positive value indicates electron donation while a negative value indicates electron acceptance.

Table 4.1 Bader charge of bare zigzag phosphorene nanoribbon of width N = 9

Bare PNR		
Termination	AVERAGE CHARGE P	AVG CHARGE Lig.
NH2	0.6869	-0.1977
OH	0.6892	-0.3389
H	0.3357	-0.3267
SCH3	0.2373	-0.048
SH	0.232	-0.1259
Cl	0.4414	-0.4657
OCN	0.6687	-0.2386

Table 4.2 Bader charge of sodium adsorbed zigzag phosphorene nanoribbon of width N = 9

Na - Adsorbed PNR				
Termination	AVG CHARGE EDGE P	AVG CHARGE Lig.	AVG CHARGE P_Na	AVG CHG Na
NH2	0.6759	-0.1964	-0.2014	0.7128
OH	0.6875	-0.3405	-0.1894	0.7168
H	0.3244	-0.3300	-0.1934	0.7160
SCH3	0.2227	-0.0497	-0.1942	0.7127
SH	0.2446	-0.1313	-0.1956	0.7167
Cl	0.4247	-0.472	-0.1976	0.7198
OCN	0.6482	-0.2401	-0.1861	0.7268

As we can see in Tables 4.1 and 4.2, phosphorene is a phenomenal electron donor and ends up donating charge to the ligand in all cases. However, in the case of sodium adsorbed structures, sodium ends up being a better donor and phosphorene accepts charge from sodium. This affirms what is observed in the density of states and charge density visualization. Sodium forms a dipolar-covalent-like bond with phosphorene and injects states into the gap for the two-sodium case and leads to metallic behavior when four or more sodium are adsorbed.

4.7 Conclusions

From the cluster model, with a direct comparison of ionization energy to dipole moment attributed to the ligands, the strong positive correlation between the two becomes obvious suggesting that the dipole moment located on the ligand is indeed causing the effective change in ionization energy or shift in molecular orbitals. Furthermore, adding support to this conclusion, there seems to be no correlation between the charge on the phosphorus sheet and ionization energy. If charge transfer were the mechanism causing the observed shift in quantum states and subsequent change in ionization energy, we should see a positive correlation between the charge on phosphorene and ionization energy. Thus, we deduce that the dipole located on the ligands is causing the shift in molecular orbitals.

Comparing these results to the periodic nanoribbons, we see the increase in work function follow the same trend, or ligand order, as the ionization energy. Additionally, changes in bandgap values for various ligation are negligible supporting the conclusion hypothesis that charge transfer between phosphorene ribbon and ligand resulting from the binding action is not responsible for the observed shift in work function.

Finally, the addition of sodium atoms in various concentrations was able to change the value of the bandgap from approximate 0.94 eV in the 0 Na case to 0.42 eV in the 2 Na case and transition to metallic nature at greater than or equal to 4 Na. However, these results showed that sodium adsorption had no effect on the p-/n-character of the material. Chapter 5 presents an adaptation of the surface doping approach taken with sodium atoms in this chapter in order to attempt a more targeted approach in controlling the nature of carriers for phosphorene.

References

1. A.K. Geim, K.S. Novoselov, The rise of graphene, *Nat Mater.* 6 (2007) 183–191. <https://doi.org/10.1038/nmat1849>.
2. K.S. Novoselov, A.K. Geim, S.V. Morozov, D. Jiang, M.I. Katsnelson, I.V. Grigorieva, S.V. Dubonos, A.A. Firsov, Two-dimensional gas of massless Dirac fermions in graphene, *Nature.* 438 (2005) 197–200. <https://doi.org/10.1038/nature04233>.
3. M. Ashton, J. Paul, S.B. Sinnott, R.G. Hennig, Topology-Scaling Identification of Layered Solids and Stable Exfoliated 2D Materials, *Phys. Rev. Lett.* 118 (2017) 106101. <https://doi.org/10.1103/PhysRevLett.118.106101>.
4. S.Z. Butler, S.M. Hollen, L. Cao, Y. Cui, J.A. Gupta, H.R. Gutiérrez, T.F. Heinz, S.S. Hong, J. Huang, A.F. Ismach, E. Johnston-Halperin, M. Kuno, V.V. Plashnitsa, R.D. Robinson, R.S. Ruoff, S. Salahuddin, J. Shan, L. Shi, M.G. Spencer, M. Terrones, W. Windl, J.E. Goldberger, Progress, Challenges, and Opportunities in Two-Dimensional Materials Beyond Graphene, *ACS Nano.* 7 (2013) 2898–2926. <https://doi.org/10.1021/nn400280c>.
5. G.R. Bhimanapati, Z. Lin, V. Meunier, Y. Jung, J. Cha, S. Das, D. Xiao, Y. Son, M.S. Strano, V.R. Cooper, L. Liang, S.G. Louie, E. Ringe, W. Zhou, S.S. Kim, R.R. Naik, B.G. Sumpter, H. Terrones, F. Xia, Y. Wang, J. Zhu, D. Akinwande, N. Alem, J.A. Schuller, R.E. Schaak, M. Terrones, J.A. Robinson, Recent Advances in Two-Dimensional Materials beyond Graphene, *ACS Nano.* 9 (2015) 11509–11539. <https://doi.org/10.1021/acsnano.5b05556>.
6. X. Duan, C. Wang, A. Pan, R. Yu, X. Duan, Two-dimensional transition metal dichalcogenides as atomically thin semiconductors: opportunities and challenges, *Chem. Soc. Rev.* 44 (2015) 8859–8876. <https://doi.org/10.1039/C5CS00507H>.
7. M.C. Watts, L. Picco, F.S. Russell-Pavier, P.L. Cullen, T.S. Miller, S.P. Bartuś, O.D. Payton, N.T. Skipper, V. Tileli, C.A. Howard, Production of phosphorene nanoribbons, *Nature.* 568 (2019) 216–220. <https://doi.org/10.1038/s41586-019-1074-x>.
8. A. Carvalho, M. Wang, X. Zhu, A.S. Rodin, H. Su, A.H. Castro Neto, Phosphorene: from theory to applications, *Nat Rev Mater.* 1 (2016) 1–16. <https://doi.org/10.1038/natrevmats.2016.61>.
9. H. Liu, A.T. Neal, Z. Zhu, Z. Luo, X. Xu, D. Tománek, P.D. Ye, Phosphorene: An Unexplored 2D Semiconductor with a High Hole Mobility, *ACS Nano.* 8 (2014) 4033–4041. <https://doi.org/10.1021/nn501226z>.
10. L. Kou, C. Chen, S.C. Smith, Phosphorene: Fabrication, Properties, and Applications, *J. Phys. Chem. Lett.* 6 (2015) 2794–2805. <https://doi.org/10.1021/acs.jpcllett.5b01094>.

11. V. Tran, L. Yang, Scaling laws for the band gap and optical response of phosphorene nanoribbons, *Phys. Rev. B.* 89 (2014) 245407. <https://doi.org/10.1103/PhysRevB.89.245407>.
12. Y. Cai, G. Zhang, Y.-W. Zhang, Layer-dependent Band Alignment and Work Function of Few-Layer Phosphorene, *Sci Rep.* 4 (2014) 6677. <https://doi.org/10.1038/srep06677>.
13. S. Lee, F. Yang, J. Suh, S. Yang, Y. Lee, G. Li, H. Sung Choe, A. Suslu, Y. Chen, C. Ko, J. Park, K. Liu, J. Li, K. Hippalgaonkar, J.J. Urban, S. Tongay, J. Wu, Anisotropic in-plane thermal conductivity of black phosphorus nanoribbons at temperatures higher than 100 K, *Nat Commun.* 6 (2015) 8573. <https://doi.org/10.1038/ncomms9573>.
14. F. Xia, H. Wang, Y. Jia, Rediscovering black phosphorus as an anisotropic layered material for optoelectronics and electronics, *Nat Commun.* 5 (2014) 4458. <https://doi.org/10.1038/ncomms5458>.
15. H. Guo, N. Lu, J. Dai, X. Wu, X.C. Zeng, Phosphorene Nanoribbons, Phosphorus Nanotubes, and van der Waals Multilayers, *J. Phys. Chem. C.* 118 (2014) 14051–14059. <https://doi.org/10.1021/jp505257g>.
16. E. Taghizadeh Sisakht, M.H. Zare, F. Fazileh, Scaling laws of band gaps of phosphorene nanoribbons: A tight-binding calculation, *Phys. Rev. B.* 91 (2015) 085409. <https://doi.org/10.1103/PhysRevB.91.085409>.
17. X. Peng, Q. Wei, A. Copple, Strain-engineered direct-indirect band gap transition and its mechanism in two-dimensional phosphorene, *Phys. Rev. B.* 90 (2014) 085402. <https://doi.org/10.1103/PhysRevB.90.085402>.
18. J. Zhang, H.J. Liu, L. Cheng, J. Wei, J.H. Liang, D.D. Fan, J. Shi, X.F. Tang, Q.J. Zhang, Phosphorene nanoribbon as a promising candidate for thermoelectric applications, *Sci Rep.* 4 (2014) 6452. <https://doi.org/10.1038/srep06452>.
19. S. Das, M. Demarteau, A. Roelofs, Ambipolar Phosphorene Field Effect Transistor, *ACS Nano.* 8 (2014) 11730–11738. <https://doi.org/10.1021/nn505868h>.
20. C. Guo, L. Wang, H. Xing, X. Chen, The study of ambipolar behavior in phosphorene field-effect transistors, *Journal of Applied Physics.* 120 (2016) 215701. <https://doi.org/10.1063/1.4970851>.
21. G. Wang, W.J. Slough, R. Pandey, S.P. Karna, Degradation of phosphorene in air: understanding at atomic level, *2D Mater.* 3 (2016) 025011. <https://doi.org/10.1088/2053-1583/3/2/025011>.
22. K.L. Kuntz, R.A. Wells, J. Hu, T. Yang, B. Dong, H. Guo, A.H. Woomer, D.L. Druffel, A. Alabanza, D. Tománek, S.C. Warren, Control of Surface and Edge

- Oxidation on Phosphorene, *ACS Appl. Mater. Interfaces*. 9 (2017) 9126–9135. <https://doi.org/10.1021/acsami.6b16111>.
23. J. Pang, A. Bachmatiuk, Y. Yin, B. Trzebicka, L. Zhao, L. Fu, R.G. Mendes, T. Gemming, Z. Liu, M.H. Rummeli, Applications of Phosphorene and Black Phosphorus in Energy Conversion and Storage Devices, *Advanced Energy Materials*. 8 (2018) 1702093. <https://doi.org/10.1002/aenm.201702093>.
 24. Z. Liu, Y. Sun, H. Cao, D. Xie, W. Li, J. Wang, A.K. Cheetham, Unzipping of black phosphorus to form zigzag-phosphorene nanobelts, *Nat Commun*. 11 (2020) 3917. <https://doi.org/10.1038/s41467-020-17622-6>.
 25. V. Sresht, A.A.H. Pádua, D. Blankschtein, Liquid-Phase Exfoliation of Phosphorene: Design Rules from Molecular Dynamics Simulations, *ACS Nano*. 9 (2015) 8255–8268. <https://doi.org/10.1021/acsnano.5b02683>.
 26. J.F. Corrigan, O. Fuhr, D. Fenske, Metal chalcogenide clusters on the border between molecules and materials, *Advanced Materials*. 21 (2009) 1867–1871.
 27. V. Chauhan, A.C. Reber, S.N. Khanna, Metal chalcogenide clusters with closed electronic shells and the electronic properties of alkalis and halogens, *Journal of the American Chemical Society*. 139 (2017) 1871–1877.
 28. S.N. Khanna, A.C. Reber, D. Bista, T. Sengupta, R. Lambert, The superatomic state beyond conventional magic numbers: Ligated metal chalcogenide superatoms, *J. Chem. Phys.* 155 (2021) 120901. <https://doi.org/10.1063/5.0062582>.
 29. A.C. Reber, S.N. Khanna, $\text{Co}_6\text{Se}_8(\text{PEt}_3)_6$ superatoms as tunable chemical dopants for two-dimensional semiconductors, *Npj Computational Materials*. 4 (2018) 1–6.
 30. V. Chauhan, A.C. Reber, S.N. Khanna, Transforming Ni_9Te_6 from electron donor to acceptor via ligand exchange, *The Journal of Physical Chemistry A*. 120 (2016) 6644–6649.
 31. A.C. Reber, V. Chauhan, D. Bista, S.N. Khanna, Superatomic molecules with internal electric fields for light harvesting, *Nanoscale*. 12 (2020) 4736–4742.
 32. V. Chauhan, A.C. Reber, S.N. Khanna, Strong lowering of ionization energy of metallic clusters by organic ligands without changing shell filling, *Nature Communications*. 9 (2018) 1–7.
 33. A.C. Reber, D. Bista, V. Chauhan, S.N. Khanna, Transforming Redox Properties of Clusters Using Phosphine Ligands, *J. Phys. Chem. C*. 123 (2019) 8983–8989. <https://doi.org/10.1021/acs.jpcc.9b00039>.
 34. X. Roy, C.-H. Lee, A.C. Crowther, C.L. Schenck, T. Besara, R.A. Lalancette, T. Siegrist, P.W. Stephens, L.E. Brus, P. Kim, M.L. Steigerwald, C. Nuckolls, Nanoscale Atoms in Solid-State Chemistry, *Science*. 341 (2013) 157–160. <https://doi.org/10.1126/science.1236259>.

35. C.E. Anson, A. Eichhöfer, I. Issac, D. Fenske, O. Fuhr, P. Sevillano, C. Persau, D. Stalke, J. Zhang, Synthesis and Crystal Structures of the Ligand-Stabilized Silver Chalcogenide Clusters $[\text{Ag}_{154}\text{Se}_{77}(\text{dppxy})_{18}]$, $[\text{Ag}_{320}(\text{StBu})_{60}\text{S}_{130}(\text{dppp})_{12}]$, $[\text{Ag}_{352}\text{S}_{128}(\text{StC}_5\text{H}_{11})_{96}]$, and $[\text{Ag}_{490}\text{S}_{188}(\text{StC}_5\text{H}_{11})_{114}]$, *Angewandte Chemie International Edition*. 47 (2008) 1326–1331.
36. C.A. Goddard, J.R. Long, R.H. Holm, Synthesis and characterization of four consecutive members of the five-member $[\text{Fe}_6\text{S}_8(\text{PEt}_3)_6]^{n+}$ ($n = 0-4$) cluster electron transfer series, *Inorganic Chemistry*. 35 (1996) 4347–4354.
37. A.M. Champsaur, J. Yu, X. Roy, D.W. Paley, M.L. Steigerwald, C. Nuckolls, C.M. Bejger, Two-dimensional nanosheets from redox-active superatoms, *ACS Central Science*. 3 (2017) 1050–1055.
38. A. Pinkard, A.M. Champsaur, X. Roy, Molecular clusters: nanoscale building blocks for solid-state materials, *Accounts of Chemical Research*. 51 (2018) 919–929.
39. J. Yu, C.-H. Lee, D. Bouilly, M. Han, P. Kim, M.L. Steigerwald, X. Roy, C. Nuckolls, Patterning Superatom Dopants on Transition Metal Dichalcogenides, *Nano Lett.* 16 (2016) 3385–3389. <https://doi.org/10.1021/acs.nanolett.6b01152>.
40. J.P. Perdew, K. Burke, M. Ernzerhof, Generalized Gradient Approximation Made Simple, *Phys. Rev. Lett.* 77 (1996) 3865–3868. <https://doi.org/10.1103/PhysRevLett.77.3865>.
41. G. Kresse, J. Hafner, Ab initio molecular-dynamics simulation of the liquid-metal–amorphous-semiconductor transition in germanium, *Phys. Rev. B*. 49 (1994) 14251–14269. <https://doi.org/10.1103/PhysRevB.49.14251>.
42. G. Kresse, J. Furthmüller, Efficient iterative schemes for ab initio total-energy calculations using a plane-wave basis set, *Phys. Rev. B*. 54 (1996) 11169–11186. <https://doi.org/10.1103/PhysRevB.54.11169>.
43. G. Kresse, D. Joubert, From ultrasoft pseudopotentials to the projector augmented-wave method, *Phys. Rev. B*. 59 (1999) 1758–1775. <https://doi.org/10.1103/PhysRevB.59.1758>.
44. J. Heyd, G.E. Scuseria, M. Ernzerhof, Hybrid functionals based on a screened Coulomb potential, *J. Chem. Phys.* 118 (2003) 8207–8215. <https://doi.org/10.1063/1.1564060>.
45. A.M. Ganose, A.J. Jackson, D.O. Scanlon, sumo: Command-line tools for plotting and analysis of periodic *ab initio* calculations, *Journal of Open Source Software*. 3 (2018) 717. <https://doi.org/10.21105/joss.00717>.
46. G. Liu, A. Pinkard, S.M. Ciborowski, V. Chauhan, Z. Zhu, A.P. Aydt, S.N. Khanna, X. Roy, K.H. Bowen, Tuning the electronic properties of hexanuclear

- cobalt sulfide superatoms via ligand substitution, *Chem. Sci.* 10 (2019) 1760–1766. <https://doi.org/10.1039/C8SC03862G>.
47. G. Liu, V. Chauhan, A.P. Aydin, S.M. Ciborowski, A. Pinkard, Z. Zhu, X. Roy, S.N. Khanna, K.H. Bowen, Ligand Effect on the Electronic Structure of Cobalt Sulfide Clusters: A Combined Experimental and Theoretical Study, *J. Phys. Chem. C* 123 (2019) 25121–25127. <https://doi.org/10.1021/acs.jpcc.9b04153>.
 48. W. Tang, E. Sanville, and G. Henkelman A grid-based Bader analysis algorithm without lattice bias, *J. Phys.: Condens. Matter* 21, 084204 (2009).
 49. E. Sanville, S. D. Kenny, R. Smith, and G. Henkelman An improved grid-based algorithm for Bader charge allocation, *J. Comp. Chem.* 28, 899-908 (2007).
 50. G. Henkelman, A. Arnaldsson, and H. Jónsson, A fast and robust algorithm for Bader decomposition of charge density, *Comput. Mater. Sci.* 36, 354-360 (2006).
 51. M. Yu and D. R. Trinkle, Accurate and efficient algorithm for Bader charge integration, *J. Chem. Phys.* 134, 064111 (2011).

Chapter 5. Transforming the Electronic Properties of Phosphorene through Charge Transfer Superatomic Doping

5.1 Introduction

The work presented in Chapter 4 gave a promising outlook for tuning phosphorene nanoribbons via selective ligation or edge-passivation with various ligand types. By now, we also have an understanding of the directional and layer-dependent properties including high carrier mobility (up to $1000 \text{ cm}^2/\text{Vs}$) and a direct bandgap of 1.51 which have led to such excitement surrounding phosphorene.[11–15] Verification of properties outlined in previous studies indicate that the bandgap in phosphorene nanoribbons is highly tunable with changes in ribbon width. Excitingly, we have also shown that the electronic spectrum can be shifted by varying termination groups. However, we have yet to demonstrate a potential avenue for controlling the p-/n- character of phosphorene. Ideally, control over all elements of semiconductor properties, bandgap, band location, and character of charge carriers, gives the freedom to apply a material to a wide range of potential application settings. In this sense we continue the investigation of chemical doping by extending the concept to formation of charge transfer complexes between superatomic clusters and phosphorene monolayer support.

The key objective in this chapter is to propose a novel approach to controlling the band gap and even altering the p-/n-character of phosphorene by depositing ligated metal chalcogenide superatoms. Extensive work over the past few years has shown that stable metal-chalcogenide clusters[26–33] can be synthesized in solutions or in solid-state using wet chemical methods. These clusters are highly stable, and have charge donor/acceptor characteristics that can be controlled by their composition or the nature of ligands.[26,34–

38] For example, recent work by Khanna, Reber, and coworkers has shown that the addition of PEt_3 ligands to the metal chalcogenide cores can dramatically lower the first few ionization potentials making them excellent donors.[32] On the other hand, addition of CO ligands can make them excellent acceptors. The ability to design donor and acceptor superatoms has also led to the possibility of charge transfer doping, (the term charge transfer doping refers to clusters or molecules supported on a surface acting as a donor or acceptor) for two dimensional semiconductors that does not require creating defects or substituting atoms in the underlying lattice. These developments have come from experiments from the groups of Nuckolls and Roy at Columbia University.[39] In their experiments, they doped two-dimensional transition metal chalcogenide MoS_2 using supported $\text{Co}_6\text{Se}_8(\text{PEt}_3)_6$ superatoms as electron donors. Their experiments indicate that electron-rich superatoms could transform MoS_2 from moderately to heavily electron doped state by controlling the concentration of superatoms in the solution. Even more interesting was that for WSe_2 , where the characteristics of the film changed from hole transporting to electron transporting upon doping. They further used a lithographic mask (h-BN) to selectively dope areas of WSe_2 film thereby creating p-n junctions effectively creating a diode. These experimental findings could open the pathway to novel class of charge transfer doped semiconductors and the key objective of the current work is to explore these possibilities for phosphorene monolayer.

In the first iteration of charge transfer doping of phosphorene with superatoms, we first examine $\text{Co}_6\text{S}_8(\text{PH}_3)_{5-n}(\text{CO})_n$ ligated clusters supported on phosphorene surface. We show that the phosphorene surface acts as a better ligand than the PH_3 ligand subsequently enabling the superatom to bind preferentially to the phosphorene surface. The addition of

$\text{Co}_6\text{S}_8(\text{PH}_3)_{5-n}(\text{CO})_n$ superatoms changes the width of the bandgap but is unable to change the p- or n- character of the underlying film. This is because the HOMO-LUMO gap in the deposited cluster is smaller than the desired gap to affect the change. We then show that $\text{Re}_6\text{Se}_8(\text{PH}_3)_{5-n}\text{Cl}_n$ superatoms offers a wider HOMO-LUMO gap energy and can effect a change in the p- or n- type of the phosphorene sheet.

5.2 Controlling the Band Gap in Phosphorene by depositing Superatoms:

As seen in Chapter 3 and 4, nanoribbons provide an approach for controlling the electronic features in phosphorene. By varying the width of the ribbon and by terminating the edges with various ligands, zigzag ribbons can be converted from metallic to semiconducting state with band gaps as large as 2.34 eV. We would like to control band gap energy and, ideally, exhibit a method for controlling the p- and n- character of the phosphorene sheet through charge transfer dopants. This allows for doping to occur without substitutional doping that is likely to induce additional defects. For two-dimensional films, one way is to provide electrons or holes by depositing super donors and acceptors that can donate/accept multiple electrons. The ligated metal-chalcogenide superatomic clusters offer this unique possibility of donating or accepting multiple electrons.[33]

The redox properties of transition metal chalcogenide clusters can be controlled by adding organic ligands. In the case of adding donor ligands like PH_3 , the first few ionization energies of Co_6S_8 and similar clusters can be lowered by several eV making them excellent donors.[33,46,47] On the other hand, attaching acceptor ligands such as CO increases the electron affinity making them acceptors.[27] Taking advantage of the

previous findings on shifting electronic spectrum, and subsequently, ionization energy and electron affinity, we explored the possibility of controlling the band gap energy and the Fermi level by depositing the $\text{Co}_6\text{S}_8(\text{PH}_3)_{5-n}(\text{CO})_n$ clusters. The goal was to see if the band gap energy and the n-/p- character could be changed by depositing superatomic clusters, and exchanging the ligands, starting from electron donating PH_3 and switching to the electron accepting CO. Figure 5.1 gives a picture of the ligand exchange idea for $\text{Co}_6\text{S}_8(\text{PH}_3)_{5-n}(\text{CO})_n$ clusters on phosphorene monolayer. Here we can see the successive exchange between PH_3 and CO.

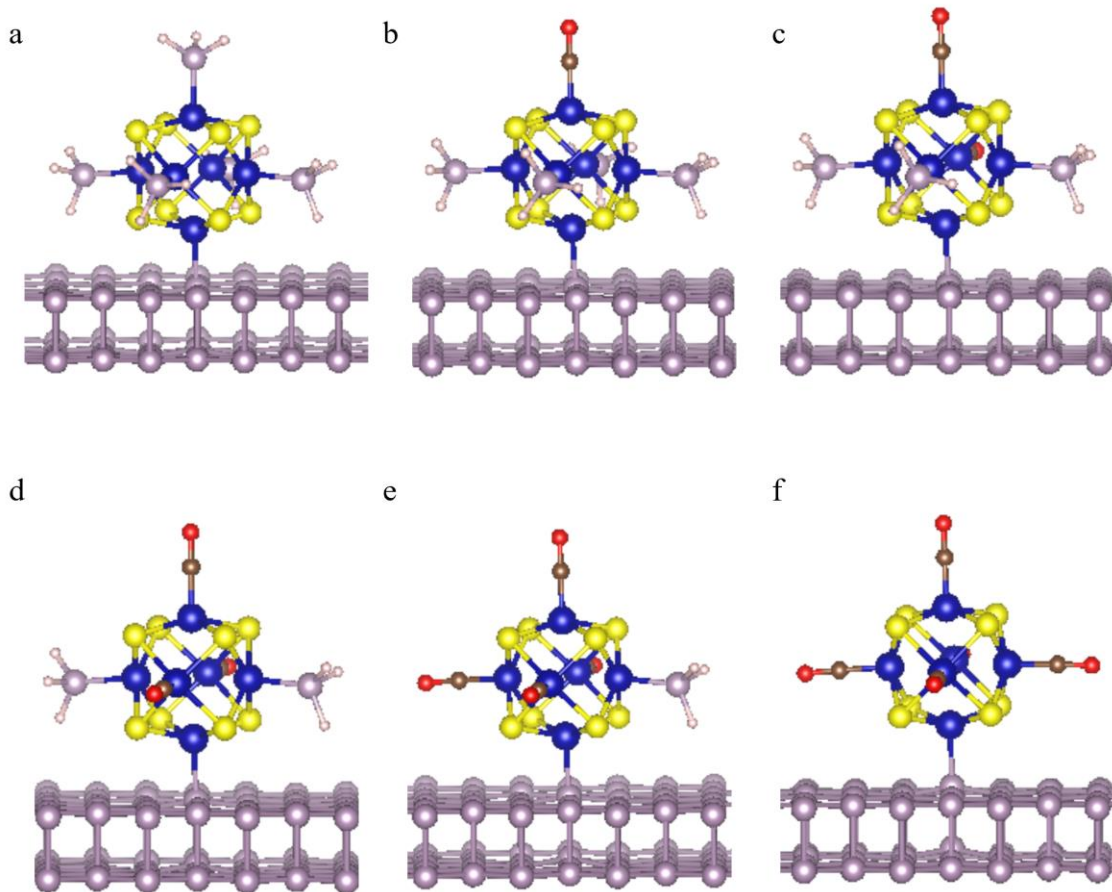


Figure 5.1. Complete picture of all CONTCAR geometry for $\text{Co}_6\text{S}_8(\text{PH}_3)_{5-n}(\text{CO})_n$ doped phosphorene monolayer as a function of n from 0 – 5 (a-f).

Since the absorption of the ligated clusters to the surface usually proceeds by preparing the fully ligated clusters in solution and depositing them on the surface, we first compared the binding energy of a 6th phosphine ligand to the binding energy of phosphorene if the 6th ligand is replaced with the phosphorene sheet. In order to take advantage of the unique properties of the ligated metal chalcogenide clusters we must show that the cluster can bind preferentially with the sheet over the sixth PH₃ ligand or CO ligand. Table 5.1 gives all values of binding energy.

Table 5.1. Comparison of binding energies for ligand-to-cluster and cluster-to-surface showing that all cases, for both (a) Co₆S₈(PH₃)_{5-n}(CO)_n and (b) Re₆Se₈(PH₃)_{5-n}(Cl)_n superatomic clusters, the cluster binds preferentially to the surface of the phosphorene monolayer.

(a) Co₆S₈(PH₃)_{5-n}(CO)_n		
# of CO Ligands	Ligand-to-Cluster B.E. (eV)	Cluster-to-Surface B.E. (eV)
0	2.0687	4.01877
1	2.1048	3.829
2	2.1125	3.7051
3	2.2007	3.6649
4	2.3096	3.6593
5	2.4017	3.6269

(b) Re₆Se₈(PH₃)_{5-n}(Cl)_n		
# of Cl Ligands	Ligand-to-Cluster B.E. (eV)	Cluster-to-Surface B.E. (eV)
0	0.7863	4.224
1	0.8237	3.3691
2	1.6669	3.2329
3	1.6954	3.3529

A plot comparison, given in Figure 5.2, of the relative binding energies ensures that the replacement of the ligand by the surface is energetically favorable. It becomes quite obvious upon observation of Figure 5.2 comparing binding energy of the ligand and the phosphorene film for various compositions of the cluster, that the binding energy of the

phosphorene film is significantly higher than the phosphine ligand in all cases. This shows that the phosphorene surface may act as a ligand and ligand replacement by the phosphorene surface is energetically favorable.

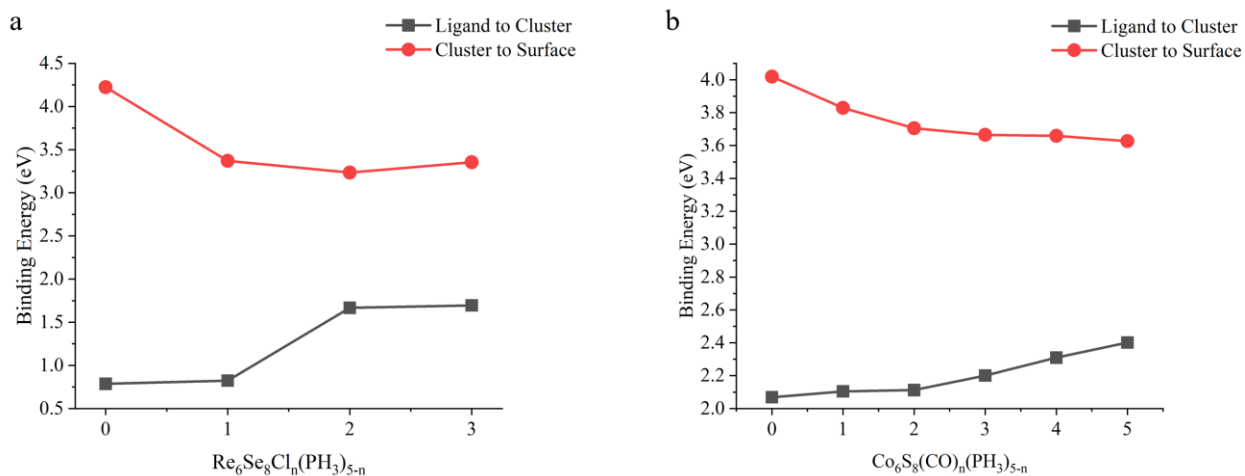


Figure 5.2. Binding energies of phosphine ligands to cluster and cluster to surface as ligands are exchanged as a function of n for both (a) $\text{Re}_6\text{Se}_8(\text{Cl})_n(\text{PH}_3)_{5-n}$ and (b) $\text{Co}_6\text{S}_8(\text{CO})_n(\text{PH}_3)_{5-n}$ respectively.

Since the cluster does bind preferentially to the phosphorene substrate, we direct our attention to the anticipated task of charge transfer doping with the aim of sufficiently shifting the electronic spectrum of the clusters within the bandgap of phosphorene. In order to effectively induce a change from traditional semiconductor to p-type character the LUMO of the cluster must insert into the bandgap below the conduction band of the phosphorene support, supplying available states lower in energy than the conduction band. For n-type doping to occur, the HOMO of the cluster must lie above the valence band of the phosphorene support subsequently injecting electrons into the bandgap. Figure 5.3 outlines the results for $\text{Co}_6\text{S}_8(\text{PH}_3)_{5-n}(\text{CO})_n$ clusters. Importantly, we note the use of HSE06

hybrid functional in order to model the electronic structure of the doped phosphorene more accurately.[44]

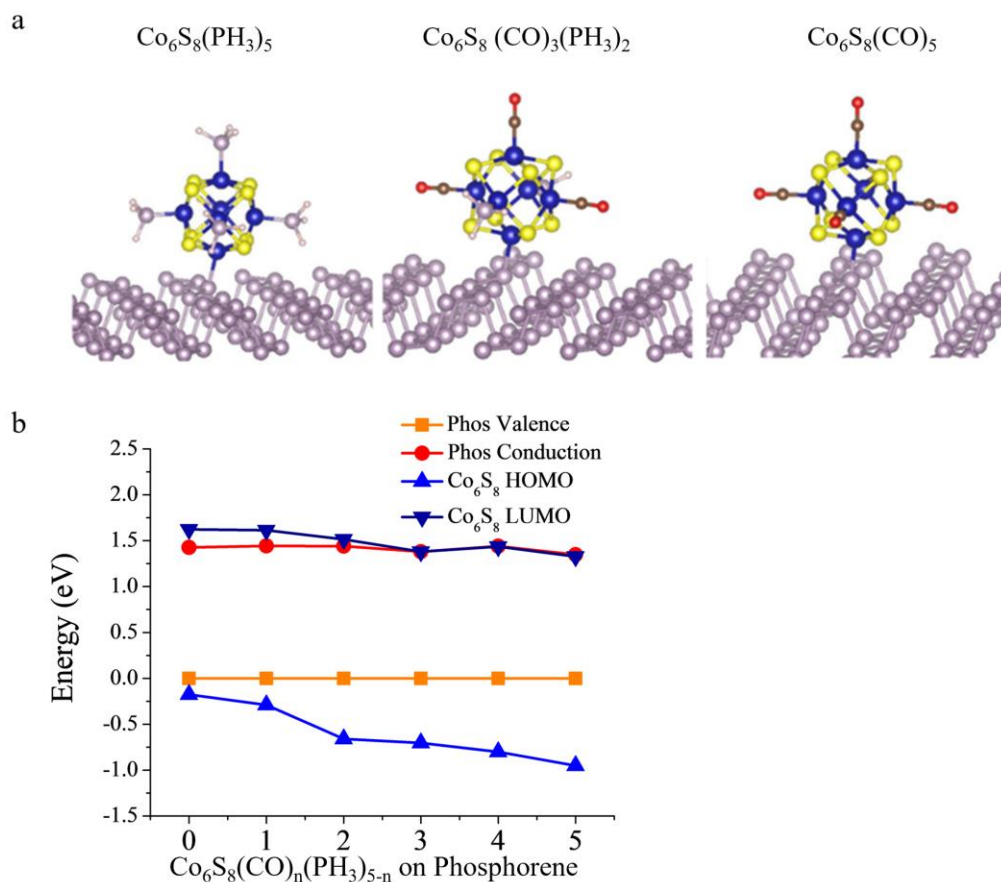


Figure 5.3. (a) The structure of $\text{Co}_6\text{S}_8(\text{PH}_3)_5$, $\text{Co}_6\text{S}_8(\text{CO})_3(\text{PH}_3)_2$, and $\text{Co}_6\text{S}_8(\text{CO})_5$, supported on Phosphorene. (b) The position of the valence and conduction band of phosphorene, and the HOMO and LUMO of the $\text{Co}_6\text{S}_8(\text{CO})_n(\text{PH}_3)_{5-n}$ cluster as a function of n . Note, the valence band maximum is set to zero in the presentation of the band energy levels.

As the PH_3 ligands are replaced with CO ligands, the effective gap between the occupied and unoccupied states that are both localized on the cluster changes from 1.44 to 1.33 eV for the complete coverage with CO ligands, as seen in Figure 5.3b. The conduction band of the phosphorene and the LUMO of the cluster are pinned at the same energy level. For 0 and 1 CO molecules, the HOMO of the cluster lies slightly below the valence band of phosphorene. Further exchange of PH_3 with CO ligands lowers the HOMO of the cluster

significantly below the valence band. This means that phosphine is not a strong enough electron donor to add to the high lying valence band of the phosphorene support. This shows that, while the cluster does change the effective band gap, it is not able to alter the p- or n- character of the underlying film.

Projected density of states for the $\text{Co}_6\text{S}_8(\text{CO})_n(\text{PH}_3)_{5-n}$ clusters are shown in Figure 5.4. If charge transfer p-/n-type doping was taking place we would be able to see an associated peak corresponding to states from the cluster inserted into the bandgap of phosphorene. In other words, while the phosphorene peaks associated with valence and conduction bands would change slightly in energy, there would be noticeable peaks between the conduction and valence band leading to the idealized doping behavior. Instead, we see the cluster HOMO states are deep to the valence band while the cluster LUMO states are hybridized with the phosphorene conduction band effectively pinning the energy.

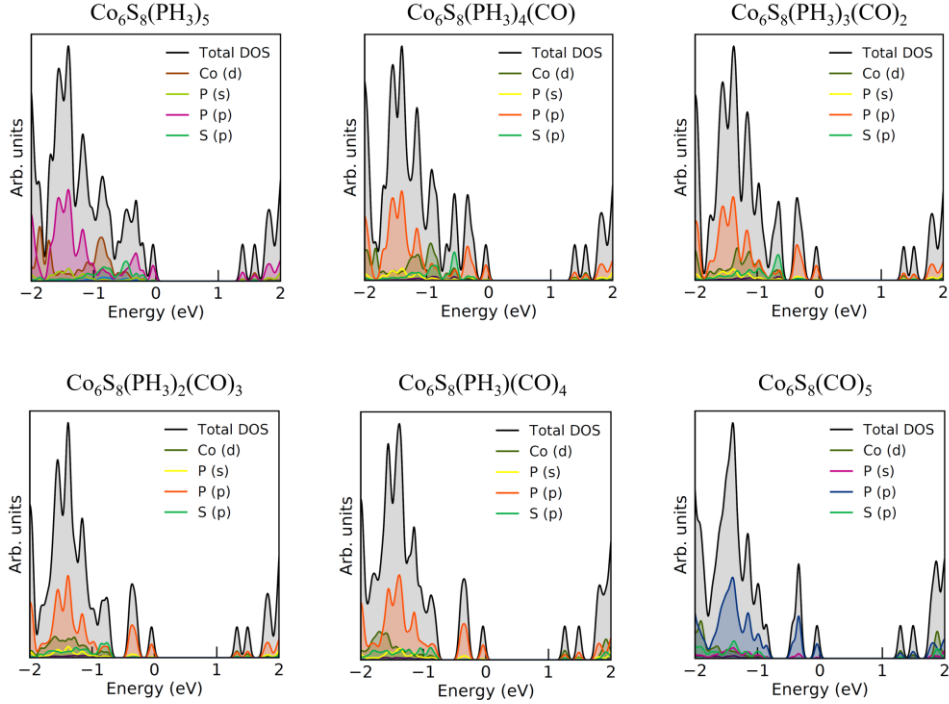


Figure 5.4. Projected density of states for $\text{Co}_6\text{S}_8(\text{PH}_3)_{5-n}(\text{CO})_n$ as a function of n , plotted from results obtained using the HSE06 hybrid functional. Note, for sumo software, the legend cutoff for PDOS is 3% thus, C and O are not included in the legend due to their low contribution to overall number of states in the plotted energy range.

In conventional doping, local sites are substituted by a heterogeneous atom, and when this occurs, the impurity states have a large radius due to screened coulomb repulsion and lead to impurity band even for low concentrations. Here, the cluster electronic states are expected to be largely localized around the cluster and therefore one must consider the valence and conduction band of the underlying lattice as well as the HOMO and LUMO of the cluster. Fig. 5.5 shows the location of these states where the HOMO and LUMO of the cluster were identified by projecting the electronic states on the cluster. To examine how the cluster states mix with phosphorus states of the underlying phosphorene support, we show in Fig. 5.5 the charge density distribution of LUMO along with HOMO. We found that HOMO of cluster states initially remains close to valence band of the underlying

lattice before dropping below the valence band while the LUMO is close to conduction band throughout the ligand exchange. We therefore tried a cluster where some of the CO ligands were replaced with Cl atoms to form a cluster with large HOMO-LUMO gap and desired placement of levels. We now show how a change in the cluster can lead to a control of the Fermi level of the underlying film.

5.3 Controlling p-/n- Character using $\text{Re}_6\text{Se}_8\text{Cl}_n(\text{PH}_3)_{5-n}$ Clusters as Charge Transfer Dopants:

As shown in the previous section, $\text{Co}_6\text{S}_8(\text{CO})_n(\text{PH}_3)_{5-n}$ was unable to change the Fermi level of the system. Since it was our aim to demonstrate that a suitable choice of

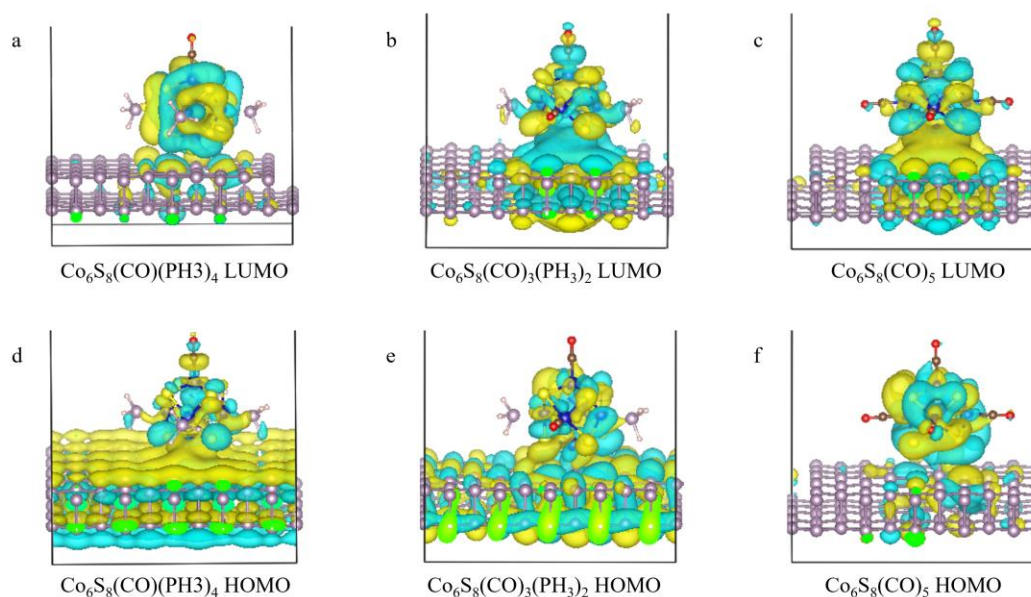


Figure 5.5. Charge density associated with LUMO (a-c) and HOMO (d-f) states of the cluster for $\text{Co}_6\text{S}_8(\text{CO})_{1,3,5}(\text{PH}_3)_{4,2,0}$

superatomic cluster can lead to states located within the gap of the phosphorene support, there needs to be a more dramatic shift in the electronic spectrum of the cluster with ligand exchange than the predecessor has displayed. With the knowledge that phosphorene has such a high valence band relative to the $\text{Co}_6\text{S}_8(\text{CO})_n(\text{PH}_3)_{5-n}$ cluster an adjustment to the

cluster electronic spectrum is needed. A difference in cluster core and ligation could provide a sufficient shift to the electronic spectrum such that HOMO and LUMO levels are able to insert into the bandgap of phosphorene. Given the unsatisfactory performance of the previous choice of cluster, the next choice of superatomic charge transfer dopant was guided by previous studies done by our group.[46,47] Figure 5.6 displays the adsorbed $\text{Re}_6\text{Se}_8(\text{Cl})_n(\text{PH}_3)_{5-n}$ on phosphorene monolayer through ligand exchange between CO and Cl ligands.

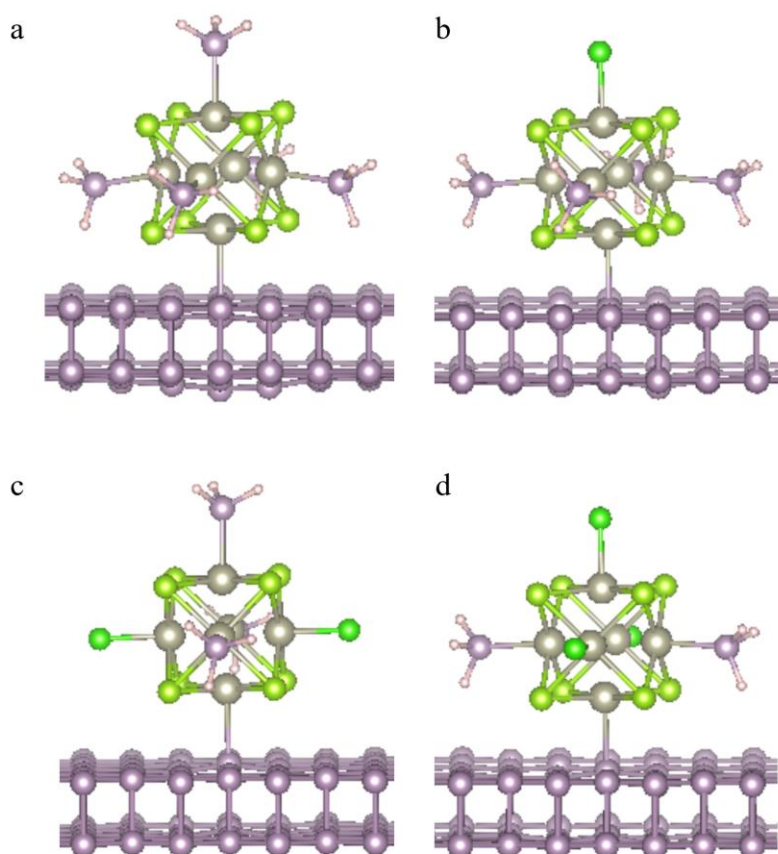


Figure 5.6. Complete picture of all CONTCAR geometry for $\text{Re}_6\text{Se}_8(\text{PH}_3)_{5-n}(\text{Cl})_n$ doped phosphorene monolayer as a function of n from 0 – 3 (a-d).

The $\text{Re}_6\text{Se}_8(\text{Cl})_n(\text{PH}_3)_{5-n}$ cluster has a larger HOMO-LUMO gap than $\text{Co}_6\text{S}_8(\text{CO})_n(\text{PH}_3)_{5-n}$ which, with successive ligand exchange, leads to either the injection of

electrons into the bandgap or the introduction of low-lying states to which an electron may be excited from the valence band of the phosphorene support. In so doing, we exhibit control over the Fermi level of the material thereby changing p-/n- character. The ground state of the of a $\text{Re}_6\text{Se}_8(\text{PH}_3)_5$ cluster, shown in Figure 5.6 a), is a spin triplet with LUMO located close to the conduction band of phosphorene. Also, the HOMO-LUMO gap is larger than the band gap of the phosphorene. This provides an ideal situation if the LUMO of the cluster could be lowered by replacing PH_3 ligands with Cl towards the valence band of the phosphorene sheet. To explore such a possibility, the cluster was supported on the phosphorene surface and we carried out electronic structure calculations as 1-3 PH_3 ligands were replaced with Cl atoms. In each case, the resulting electronic structure was analyzed to identify the valence band, the conduction band, and the HOMO and LUMO states of the cluster. The position of the valence and conduction band of phosphorene, and the HOMO and LUMO of Re_6Se_8 can be seen in Figure 5.7 b). Additionally, the Fermi energy of the system, obtained by broadening the electronic states with a Gaussian of width 0.05 eV, has been included. The location of Fermi energy helps to identify if the highest occupied state is located on the cluster or phosphorene (in case the cluster state is embedded in the valence band region). For a $\text{Re}_6\text{Se}_8(\text{PH}_3)_5$ and $\text{Re}_6\text{Se}_8\text{Cl}(\text{PH}_3)_4$ clusters, the highest occupied states are located on the cluster and are close to conduction band indicating a n-type semiconducting behavior. The slight change in the HOMO and LUMO levels as a single PH_3 is replaced by Cl is related to the even/odd electron count. The successive exchange of PH_3 with an additional Cl atom lowers the LUMO state, while the resulting system has a closed electronic shell and a band gap energy of 1.48 eV. For $\text{Re}_6\text{Se}_8\text{Cl}_3(\text{PH}_3)_2$ cluster, the LUMO of the cluster is slightly above the valence band and

the system behaves like a p-type semiconductor. This is remarkable as it shows that one can transform phosphorene into n- or p- type by depositing the appropriate superatoms and via ligand exchange.

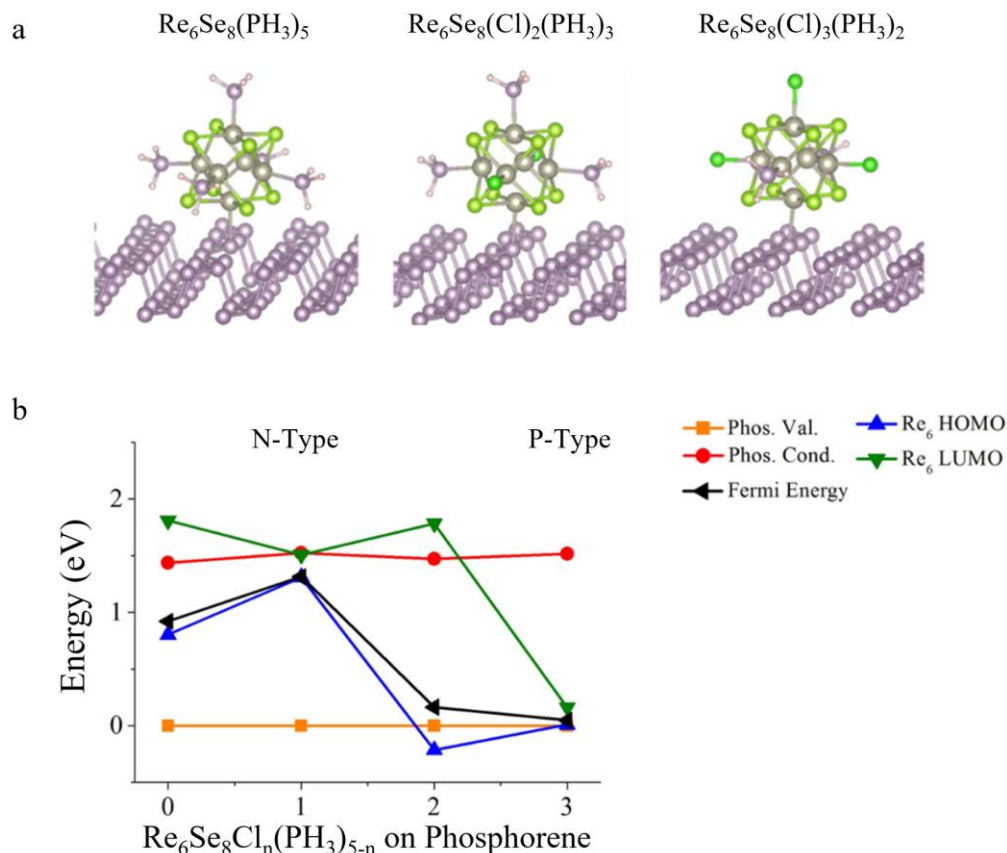


Figure 5.7. (a) The structure of $\text{Re}_6\text{Se}_8(\text{PH}_3)_5$, $\text{Re}_6\text{Se}_8\text{Cl}_2(\text{PH}_3)_4$, and $\text{Re}_6\text{Se}_8\text{Cl}_3(\text{PH}_3)_2$, supported on Phosphorene. (b) The position of the valence and conduction band of phosphorene, and the HOMO and LUMO of the $\text{Re}_6\text{Se}_8\text{Cl}_n(\text{PH}_3)_{5-n}$ cluster as a function of n .

As additional evidence, the combination of charge density visualization and projected density of states provides support to the observations from the electronic spectrum. Singling out the cluster HOMO gives a visualization of hybridization occurring with phosphorus and an indication of whether electrons at the observed energy given in

Figure 5.7 are indeed associated with the cluster states. Similar reasoning is followed for the cluster LUMO seen in Figure 5.8.

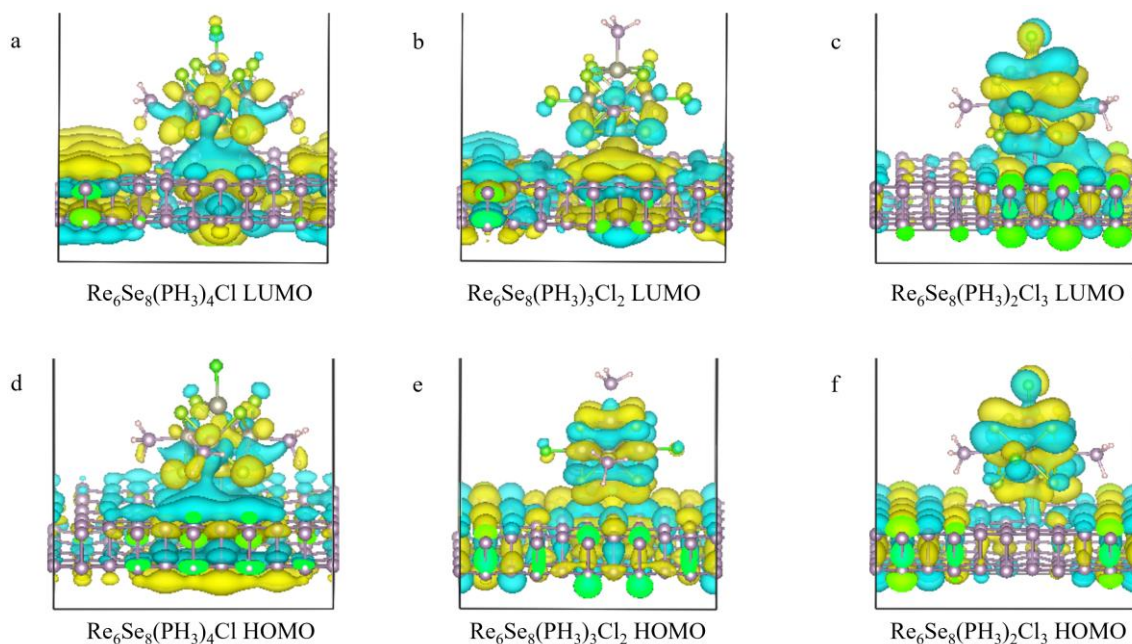


Figure 5.8. Charge density associated with HOMO and LUMO states of the cluster for $\text{Re}_6\text{Se}_8\text{Cl}_{1,2,3}(\text{PH}_3)_{4,3,2}$.

Figure 5.8 displays the electronic wavefunctions associated with the HOMO/LUMO for the $\text{Re}_6\text{Se}_8\text{Cl}_3(\text{PH}_3)_2$ cluster to identify the spread of the electronic states, while Figure 5.9 displays the projected density of states for the same levels. The HOMO is marked by cluster orbitals that are strongly hybridized with the phosphorene states (Figure 5.8 (d-f)). This is also clear in Figure 5.9 which shows that the valence band edge is composed of states derived from P as well as Cl p-states in the $\text{Re}_6\text{Se}_8(\text{PH}_3)_2\text{Cl}_3$ case. In the previous result, hybridization of the valence band edge can also be seen for Co d-states from figure 5.4. Similarly, the conduction band edge is marked by states derived from the deposited cluster and the phosphorus states. Thus, it is this collective evidence that leads to the belief that the strong hybridization results in the formation of impurity band spread over both the phosphorene and cluster. This shows that the impurity bands in

charge transfer doping can also have a large radius but are not necessarily pinned to the conduction band as they are for the Co_6S_8 cluster.

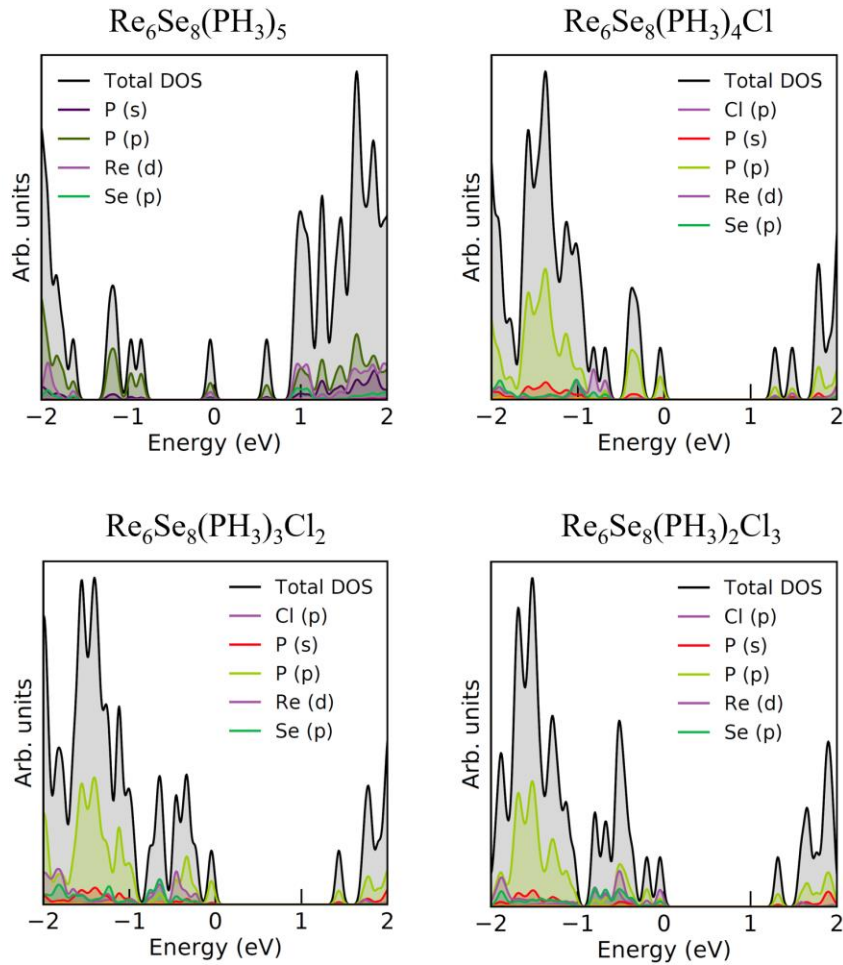


Figure 5.9. The projected density of states of $\text{Re}_6\text{Se}_8(\text{PH}_3)_5$, $\text{Re}_6\text{Se}_8\text{Cl}(\text{PH}_3)_4$, $\text{Re}_6\text{Se}_8\text{Cl}_2(\text{PH}_3)_3$, and $\text{Re}_6\text{Se}_8\text{Cl}_3(\text{PH}_3)_4$. In this case, the VBM energy is set to zero.

The promising results obtained from charge transfer doping utilizing the $\text{Re}_6\text{Se}_8\text{Cl}_n(\text{PH}_3)_{5-n}$ cluster deposited on phosphorene also leads to the belief that these strategies provide a valid method for surface doping as we have shown that not only can we impact concentration of charge carriers but also the nature of carriers. Given the result for a high valence band material, we are intrigued by the prospect of expanding these techniques in investigations of other two-dimensional materials, including ribbons.

5.4 Conclusions

The two most significant characteristics of any semiconductor are the band gap energy and the nature of carriers. In conventional semiconductors, the nature of carriers can be controlled via doping that involves replacement of host atoms with impurity atoms of a different chemical valence. Such replacements induce structural distortions limiting the amount of doping. The present work offers an alternative approach where the band gap and/or the nature of carriers can be changed by supporting ligated clusters on the surface. Here, we show that the band gap in phosphorene can be altered by supporting $\text{Co}_6\text{S}_8(\text{CO})_n(\text{PH}_3)_{5-n}$ clusters with different combination of PH_3 and CO ligands. We then show that the nature of carriers can be controlled by depositing $\text{Re}_6\text{Se}_8\text{Cl}_n(\text{PH}_3)_{5-n}$ clusters. A larger concentration of Cl favors a p-type character while a larger number of PH_3 ligands favor a n-type character. We believe charge transfer doping via supported superatoms offers another feature, hot electrons, which was recently presented in experimental work by F. Yan et al.[48] The absorption of photons in surface-supported clusters can create hot electrons since the absorbed radiation cannot lead to plasmonic excitations as a result of the few nm cluster size. The hot electrons can then be transferred to the supporting surface resulting in exciton formation and subsequent shifts of the bandgap energy.[48] We are currently exploring these effects and how the simultaneous absorption of different adjacent clusters can be used to create nano p-/n- junctions. Additionally, we raise a question for future work – could we combine the effects of ligands on two-dimensional ribbons with charge transfer doping to obtain more desirable results by shifting the electronic spectrum of the support into an optimal range such that the cluster HOMO and LUMO states may insert into the bandgap?

References

- [1] A.K. Geim, K.S. Novoselov, The rise of graphene, *Nat Mater.* 6 (2007) 183–191. <https://doi.org/10.1038/nmat1849>.
- [2] K.S. Novoselov, A.K. Geim, S.V. Morozov, D. Jiang, M.I. Katsnelson, I.V. Grigorieva, S.V. Dubonos, A.A. Firsov, Two-dimensional gas of massless Dirac fermions in graphene, *Nature.* 438 (2005) 197–200. <https://doi.org/10.1038/nature04233>.
- [3] M. Ashton, J. Paul, S.B. Sinnott, R.G. Hennig, Topology-Scaling Identification of Layered Solids and Stable Exfoliated 2D Materials, *Phys. Rev. Lett.* 118 (2017) 106101. <https://doi.org/10.1103/PhysRevLett.118.106101>.
- [4] S.Z. Butler, S.M. Hollen, L. Cao, Y. Cui, J.A. Gupta, H.R. Gutiérrez, T.F. Heinz, S.S. Hong, J. Huang, A.F. Ismach, E. Johnston-Halperin, M. Kuno, V.V. Plashnitsa, R.D. Robinson, R.S. Ruoff, S. Salahuddin, J. Shan, L. Shi, M.G. Spencer, M. Terrones, W. Windl, J.E. Goldberger, Progress, Challenges, and Opportunities in Two-Dimensional Materials Beyond Graphene, *ACS Nano.* 7 (2013) 2898–2926. <https://doi.org/10.1021/nn400280c>.
- [5] G.R. Bhimanapati, Z. Lin, V. Meunier, Y. Jung, J. Cha, S. Das, D. Xiao, Y. Son, M.S. Strano, V.R. Cooper, L. Liang, S.G. Louie, E. Ringe, W. Zhou, S.S. Kim, R.R. Naik, B.G. Sumpter, H. Terrones, F. Xia, Y. Wang, J. Zhu, D. Akinwande, N. Alem, J.A. Schuller, R.E. Schaak, M. Terrones, J.A. Robinson, Recent Advances in Two-Dimensional Materials beyond Graphene, *ACS Nano.* 9 (2015) 11509–11539. <https://doi.org/10.1021/acsnano.5b05556>.
- [6] X. Duan, C. Wang, A. Pan, R. Yu, X. Duan, Two-dimensional transition metal dichalcogenides as atomically thin semiconductors: opportunities and challenges, *Chem. Soc. Rev.* 44 (2015) 8859–8876. <https://doi.org/10.1039/C5CS00507H>.
- [7] M.C. Watts, L. Picco, F.S. Russell-Pavier, P.L. Cullen, T.S. Miller, S.P. Bartus, O.D. Payton, N.T. Skipper, V. Tileli, C.A. Howard, Production of phosphorene nanoribbons, *Nature.* 568 (2019) 216–220. <https://doi.org/10.1038/s41586-019-1074-x>.
- [8] A. Carvalho, M. Wang, X. Zhu, A.S. Rodin, H. Su, A.H. Castro Neto, Phosphorene: from theory to applications, *Nat Rev Mater.* 1 (2016) 1–16. <https://doi.org/10.1038/natrevmats.2016.61>.
- [9] H. Liu, A.T. Neal, Z. Zhu, Z. Luo, X. Xu, D. Tománek, P.D. Ye, Phosphorene: An Unexplored 2D Semiconductor with a High Hole Mobility, *ACS Nano.* 8 (2014) 4033–4041. <https://doi.org/10.1021/nn501226z>.
- [10] L. Kou, C. Chen, S.C. Smith, Phosphorene: Fabrication, Properties, and Applications, *J. Phys. Chem. Lett.* 6 (2015) 2794–2805. <https://doi.org/10.1021/acs.jpcllett.5b01094>.
- [11] V. Tran, L. Yang, Scaling laws for the band gap and optical response of phosphorene nanoribbons, *Phys. Rev. B.* 89 (2014) 245407. <https://doi.org/10.1103/PhysRevB.89.245407>.
- [12] Y. Cai, G. Zhang, Y.-W. Zhang, Layer-dependent Band Alignment and Work Function of Few-Layer Phosphorene, *Sci Rep.* 4 (2014) 6677. <https://doi.org/10.1038/srep06677>.
- [13] S. Lee, F. Yang, J. Suh, S. Yang, Y. Lee, G. Li, H. Sung Choe, A. Suslu, Y. Chen, C. Ko, J. Park, K. Liu, J. Li, K. Hippalgaonkar, J.J. Urban, S. Tongay, J. Wu,

- Anisotropic in-plane thermal conductivity of black phosphorus nanoribbons at temperatures higher than 100 K, *Nat Commun.* 6 (2015) 8573. <https://doi.org/10.1038/ncomms9573>.
- [14] F. Xia, H. Wang, Y. Jia, Rediscovering black phosphorus as an anisotropic layered material for optoelectronics and electronics, *Nat Commun.* 5 (2014) 4458. <https://doi.org/10.1038/ncomms5458>.
- [15] H. Guo, N. Lu, J. Dai, X. Wu, X.C. Zeng, Phosphorene Nanoribbons, Phosphorus Nanotubes, and van der Waals Multilayers, *J. Phys. Chem. C.* 118 (2014) 14051–14059. <https://doi.org/10.1021/jp505257g>.
- [16] E. Taghizadeh Sisakht, M.H. Zare, F. Fazileh, Scaling laws of band gaps of phosphorene nanoribbons: A tight-binding calculation, *Phys. Rev. B.* 91 (2015) 085409. <https://doi.org/10.1103/PhysRevB.91.085409>.
- [17] X. Peng, Q. Wei, A. Copple, Strain-engineered direct-indirect band gap transition and its mechanism in two-dimensional phosphorene, *Phys. Rev. B.* 90 (2014) 085402. <https://doi.org/10.1103/PhysRevB.90.085402>.
- [18] J. Zhang, H.J. Liu, L. Cheng, J. Wei, J.H. Liang, D.D. Fan, J. Shi, X.F. Tang, Q.J. Zhang, Phosphorene nanoribbon as a promising candidate for thermoelectric applications, *Sci Rep.* 4 (2014) 6452. <https://doi.org/10.1038/srep06452>.
- [19] S. Das, M. Demarteau, A. Roelofs, Ambipolar Phosphorene Field Effect Transistor, *ACS Nano.* 8 (2014) 11730–11738. <https://doi.org/10.1021/nn505868h>.
- [20] C. Guo, L. Wang, H. Xing, X. Chen, The study of ambipolar behavior in phosphorene field-effect transistors, *Journal of Applied Physics.* 120 (2016) 215701. <https://doi.org/10.1063/1.4970851>.
- [21] G. Wang, W.J. Slough, R. Pandey, S.P. Karna, Degradation of phosphorene in air: understanding at atomic level, *2D Mater.* 3 (2016) 025011. <https://doi.org/10.1088/2053-1583/3/2/025011>.
- [22] K.L. Kuntz, R.A. Wells, J. Hu, T. Yang, B. Dong, H. Guo, A.H. Woomer, D.L. Druffel, A. Alabanza, D. Tománek, S.C. Warren, Control of Surface and Edge Oxidation on Phosphorene, *ACS Appl. Mater. Interfaces.* 9 (2017) 9126–9135. <https://doi.org/10.1021/acsami.6b16111>.
- [23] J. Pang, A. Bachmatiuk, Y. Yin, B. Trzebicka, L. Zhao, L. Fu, R.G. Mendes, T. Gemming, Z. Liu, M.H. Rummeli, Applications of Phosphorene and Black Phosphorus in Energy Conversion and Storage Devices, *Advanced Energy Materials.* 8 (2018) 1702093. <https://doi.org/10.1002/aenm.201702093>.
- [24] Z. Liu, Y. Sun, H. Cao, D. Xie, W. Li, J. Wang, A.K. Cheetham, Unzipping of black phosphorus to form zigzag-phosphorene nanobelts, *Nat Commun.* 11 (2020) 3917. <https://doi.org/10.1038/s41467-020-17622-6>.
- [25] V. Sresht, A.A.H. Pádua, D. Blankschtein, Liquid-Phase Exfoliation of Phosphorene: Design Rules from Molecular Dynamics Simulations, *ACS Nano.* 9 (2015) 8255–8268. <https://doi.org/10.1021/acs.nano.5b02683>.
- [26] J.F. Corrigan, O. Fuhr, D. Fenske, Metal chalcogenide clusters on the border between molecules and materials, *Advanced Materials.* 21 (2009) 1867–1871.
- [27] V. Chauhan, A.C. Reber, S.N. Khanna, Metal chalcogenide clusters with closed electronic shells and the electronic properties of alkalis and halogens, *Journal of the American Chemical Society.* 139 (2017) 1871–1877.

- [28] S.N. Khanna, A.C. Reber, D. Bista, T. Sengupta, R. Lambert, The superatomic state beyond conventional magic numbers: Ligated metal chalcogenide superatoms, *J. Chem. Phys.* 155 (2021) 120901. <https://doi.org/10.1063/5.0062582>.
- [29] A.C. Reber, S.N. Khanna, $\text{Co}_6\text{Se}_8(\text{PET}_3)_6$ superatoms as tunable chemical dopants for two-dimensional semiconductors, *Npj Computational Materials*. 4 (2018) 1–6.
- [30] V. Chauhan, A.C. Reber, S.N. Khanna, Transforming Ni_9Te_6 from electron donor to acceptor via ligand exchange, *The Journal of Physical Chemistry A*. 120 (2016) 6644–6649.
- [31] A.C. Reber, V. Chauhan, D. Bista, S.N. Khanna, Superatomic molecules with internal electric fields for light harvesting, *Nanoscale*. 12 (2020) 4736–4742.
- [32] V. Chauhan, A.C. Reber, S.N. Khanna, Strong lowering of ionization energy of metallic clusters by organic ligands without changing shell filling, *Nature Communications*. 9 (2018) 1–7.
- [33] A.C. Reber, D. Bista, V. Chauhan, S.N. Khanna, Transforming Redox Properties of Clusters Using Phosphine Ligands, *J. Phys. Chem. C*. 123 (2019) 8983–8989. <https://doi.org/10.1021/acs.jpcc.9b00039>.
- [34] X. Roy, C.-H. Lee, A.C. Crowther, C.L. Schenck, T. Besara, R.A. Lalancette, T. Siegrist, P.W. Stephens, L.E. Brus, P. Kim, M.L. Steigerwald, C. Nuckolls, Nanoscale Atoms in Solid-State Chemistry, *Science*. 341 (2013) 157–160. <https://doi.org/10.1126/science.1236259>.
- [35] C.E. Anson, A. Eichhöfer, I. Issac, D. Fenske, O. Fuhr, P. Sevillano, C. Persau, D. Stalke, J. Zhang, Synthesis and Crystal Structures of the Ligand-Stabilized Silver Chalcogenide Clusters $[\text{Ag}_{154}\text{Se}_{77}(\text{dppxy})_{18}]$, $[\text{Ag}_{320}(\text{StBu})_{60}\text{S}_{130}(\text{dppp})_{12}]$, $[\text{Ag}_{352}\text{S}_{128}(\text{StC}_5\text{H}_{11})_{96}]$, and $[\text{Ag}_{490}\text{S}_{188}(\text{StC}_5\text{H}_{11})_{114}]$, *Angewandte Chemie International Edition*. 47 (2008) 1326–1331.
- [36] C.A. Goddard, J.R. Long, R.H. Holm, Synthesis and characterization of four consecutive members of the five-member $[\text{Fe}_6\text{S}_8(\text{PET}_3)_6]^{n+}$ ($n = 0-4$) cluster electron transfer series, *Inorganic Chemistry*. 35 (1996) 4347–4354.
- [37] A.M. Champsaur, J. Yu, X. Roy, D.W. Paley, M.L. Steigerwald, C. Nuckolls, C.M. Bejger, Two-dimensional nanosheets from redox-active superatoms, *ACS Central Science*. 3 (2017) 1050–1055.
- [38] A. Pinkard, A.M. Champsaur, X. Roy, Molecular clusters: nanoscale building blocks for solid-state materials, *Accounts of Chemical Research*. 51 (2018) 919–929.
- [39] J. Yu, C.-H. Lee, D. Bouilly, M. Han, P. Kim, M.L. Steigerwald, X. Roy, C. Nuckolls, Patterning Superatom Dopants on Transition Metal Dichalcogenides, *Nano Lett.* 16 (2016) 3385–3389. <https://doi.org/10.1021/acs.nanolett.6b01152>.
- [40] J.P. Perdew, K. Burke, M. Ernzerhof, Generalized Gradient Approximation Made Simple, *Phys. Rev. Lett.* 77 (1996) 3865–3868. <https://doi.org/10.1103/PhysRevLett.77.3865>.
- [41] G. Kresse, J. Hafner, Ab initio molecular-dynamics simulation of the liquid-metal--amorphous-semiconductor transition in germanium, *Phys. Rev. B*. 49 (1994) 14251–14269. <https://doi.org/10.1103/PhysRevB.49.14251>.
- [42] G. Kresse, J. Furthmüller, Efficient iterative schemes for ab initio total-energy calculations using a plane-wave basis set, *Phys. Rev. B*. 54 (1996) 11169–11186. <https://doi.org/10.1103/PhysRevB.54.11169>.

- [43] G. Kresse, D. Joubert, From ultrasoft pseudopotentials to the projector augmented-wave method, *Phys. Rev. B.* 59 (1999) 1758–1775. <https://doi.org/10.1103/PhysRevB.59.1758>.
- [44] J. Heyd, G.E. Scuseria, M. Ernzerhof, Hybrid functionals based on a screened Coulomb potential, *J. Chem. Phys.* 118 (2003) 8207–8215. <https://doi.org/10.1063/1.1564060>.
- [45] A.M. Ganose, A.J. Jackson, D.O. Scanlon, sumo: Command-line tools for plotting and analysis of periodic *ab initio* calculations, *Journal of Open Source Software.* 3 (2018) 717. <https://doi.org/10.21105/joss.00717>.
- [46] G. Liu, A. Pinkard, S.M. Ciborowski, V. Chauhan, Z. Zhu, A.P. Aydt, S.N. Khanna, X. Roy, K.H. Bowen, Tuning the electronic properties of hexanuclear cobalt sulfide superatoms via ligand substitution, *Chem. Sci.* 10 (2019) 1760–1766. <https://doi.org/10.1039/C8SC03862G>.
- [47] G. Liu, V. Chauhan, A.P. Aydt, S.M. Ciborowski, A. Pinkard, Z. Zhu, X. Roy, S.N. Khanna, K.H. Bowen, Ligand Effect on the Electronic Structure of Cobalt Sulfide Clusters: A Combined Experimental and Theoretical Study, *J. Phys. Chem. C.* 123 (2019) 25121–25127. <https://doi.org/10.1021/acs.jpcc.9b04153>.

Chapter 6. Proposed Future Work: Extending Charge Transfer Doping to Various Two-Dimensional Systems and Magnetic Superatoms

Semiconductor materials are ubiquitous in a vast number of technologies utilized by consumers and large research and development companies alike. As such, the ability to control or tune the most important properties of a semiconductor – the band gap energy, the location of energy levels, and the nature of carriers, becomes vital in the improvement and development of advanced technologies. By tuning the width of the gap and p-/n-type character of conduction, we gain control over a material's capacity to play a certain role upon incorporation into a device setting. For example, moving beyond the current size limit of logic transistors, improving the function of optoelectronics devices, and even fine-tuning photovoltaic devices to increase efficiency or expand the energy range which a solar panel may harvest light. Given the importance of controlling the electronic properties of semiconductor materials, I present in the following sections, a brief summary of the work presented in this dissertation as well as potential future directions one can explore in the advancement of semiconducting materials.

Chapters 3-5 presented a body of work which highlights the bright possibilities of tuning phosphorene nanoribbons via width, and edge-passivation as well as two-dimensional semiconductors via charge transfer doping. These findings play a small role in the overall advancement of materials. However, it is the collective efforts of materials research which help to move the needle of progress. Influenced by the great need for solving technological problems like reliable energy storage and renewable energy

production, moving beyond Moore's law for logic transistors, etc. I propose several directions for future work.

As demonstrated in Chapter 4, it is possible to shift the electronic spectrum of phosphorene nanoribbons by varying the edge-passivating ligands. Combining these effects with the promising results given in Chapter 5 for charge transfer doping, it may be possible to tune the electronic spectrum of both components in order to induce p-/n-type doping more easily in a high valence band material such as phosphorene.

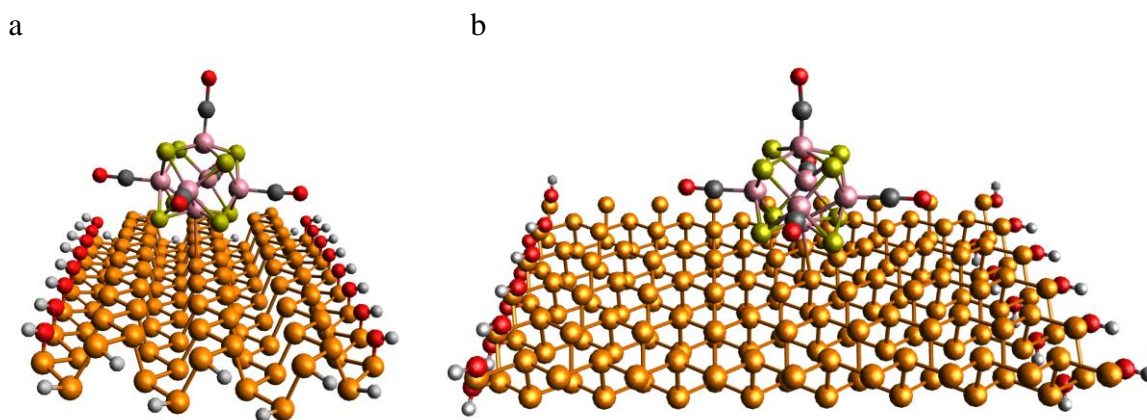


Figure 6.1. Example structures of phosphorene nanoribbons doped with $\text{Co}_6\text{S}_8(\text{CO})_5$ superatoms with zigzag (a) and armchair (b) geometries respectively.

Additionally, expanding these ideas to other nanoribbons like graphene, MoS_2 , WSe_2 , etc. may induce a variety of exciting properties. For example, it has been shown that edge-passivation of MoS_2 with oxygen induces “single edge ferromagnetism” in zigzag nanoribbons.[1] Investigating this effect in conjunction with the effects of ligated, magnetic metal chalcogenide superatoms could prove quite interesting and incites further inquisition. For example, does charge transfer doping two-dimensional nanoribbons, like edge-passivated MoS_2 , with magnetic metal chalcogenide superatoms increase the spin density of the material as a whole or are the initial effects of edge passivation negated?

By a similar line of questioning, I am interested in the effects of magnetic superatoms on periodic two-dimensional sheets like MoS₂ and WSe₂. Preliminary calculations for these structures have been performed and can be seen in Figure 2.

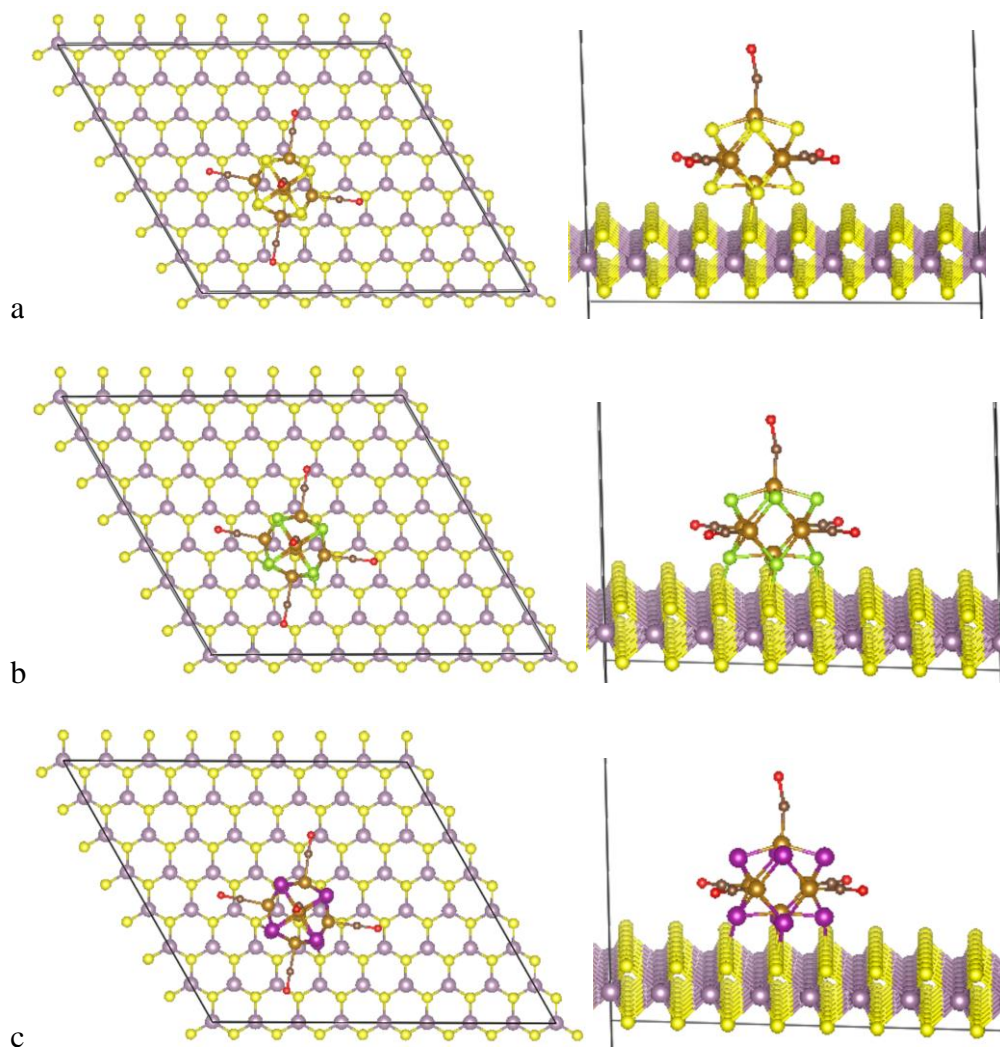


Figure 6.2. Visualization of various ligated magnetic metal chalcogenide clusters, Fe₆E₈CO₅, deposited on monolayer MoS₂, where E = S, Se, and Mn, from top to bottom.

With the promising results presented in previous chapters, comes a spark of intrigue. What possibilities exist in these new materials and can they be applied to new

technologies that ultimately make an impact and elevate quality of human life at scale? By continuing this work we hope to add knowledge and insight to the growing body of work in the field of two-dimensional materials and inspire, inform, or at least, add a valuable node to the web of science.

Appendix-A

Picture of Phosphorene Nanoribbon Optimized Geometry for All Ribbon Widths

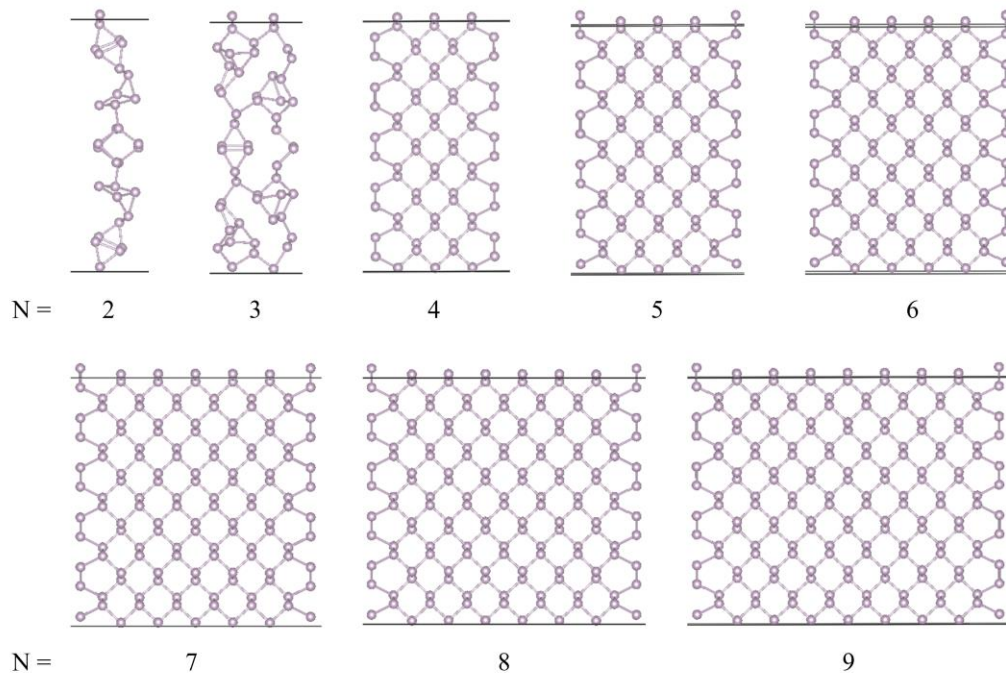


Figure A1 Complete picture of all CONTCAR geometry of non-edge-terminated armchair phosphorene nanoribbons, widths $N = 2, 9$. Note, again, the significant reconstruction for widths $N = 2$ and 3 which is not existent in ribbon widths past $N = 3$.

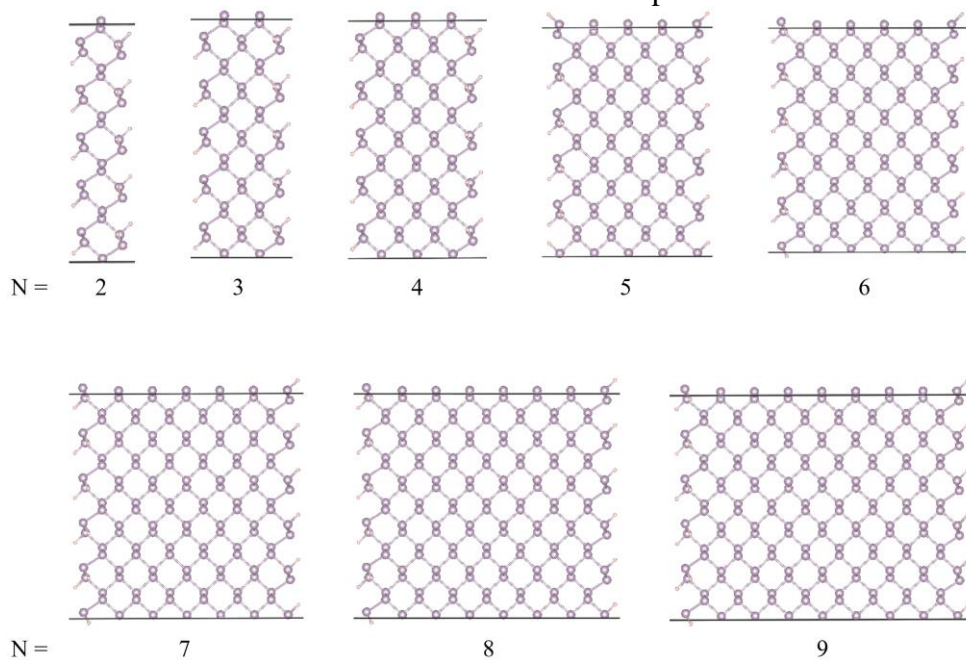


Figure A2 Complete picture of all CONTCAR geometry of terminated armchair phosphorene nanoribbons, widths $N = 2, 9$.

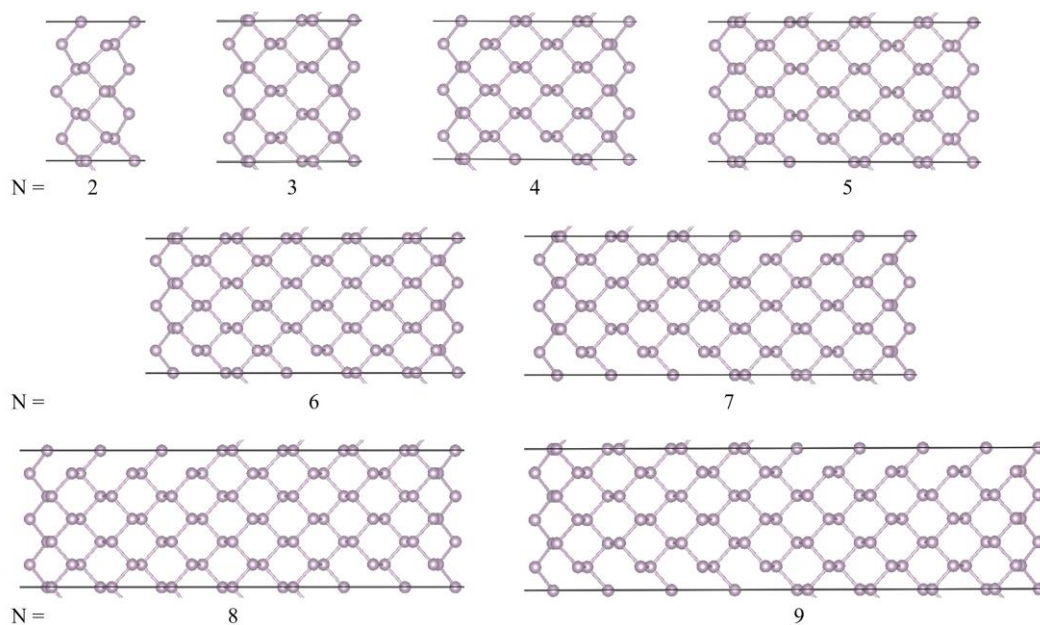


Figure A3 Complete picture of all CONTCAR geometry of non-edge-terminated zigzag phosphorene nanoribbons, widths $N = 2, 9$.

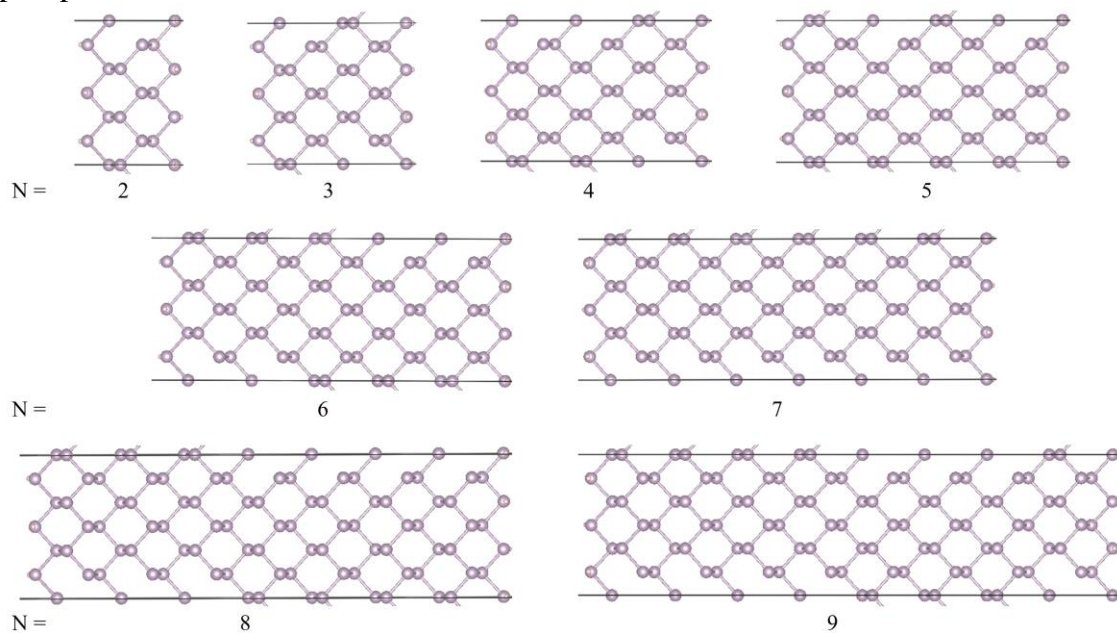


Figure A4 Complete picture of all CONTCAR geometry of terminated zigzag phosphorene nanoribbons, widths $N = 2, 9$.

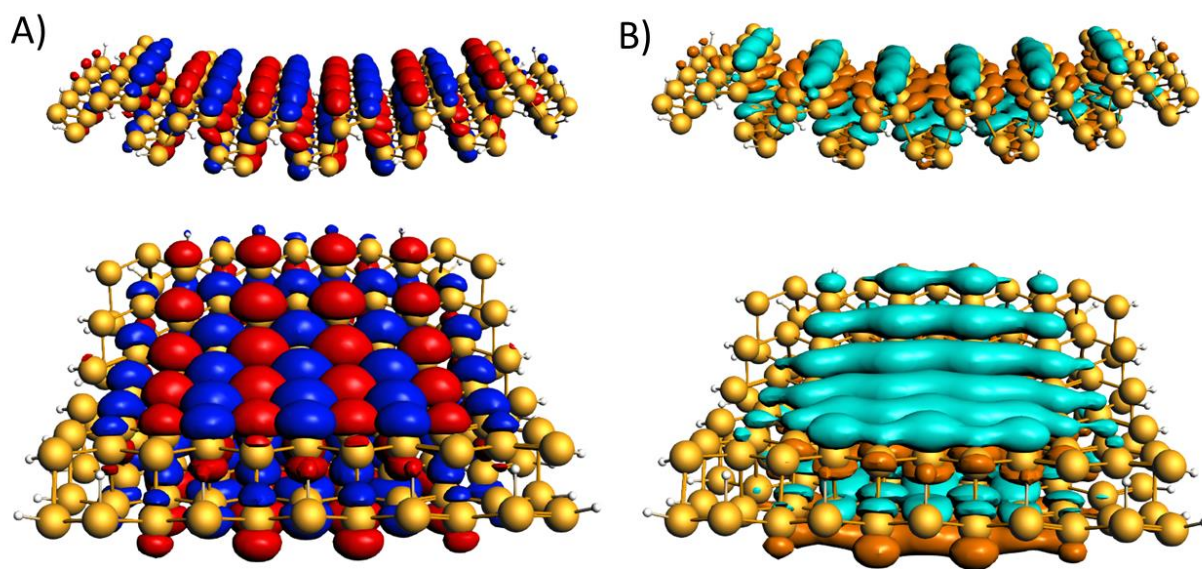


Figure A5 The A) the HOMO and B) the LUMO of the Phosphorene Cluster model $P_{141}H_{35}$.